Università degli Studi di Trieste

Dipartimento di Fisica

Corso di Studi in Fisica
Tesi di Laurea Magistrale

Studi di tracciamento per il rivelatore dell'esperimento Belle II

Laureando:
Filippo Dattola

Relatore:
Prof. Lorenzo Vitale
Correlatore:
Dott. Diego Tonelli

ANNO ACCADEMICO 2017/2018

Abstract

Questo lavoro di tesi magistrale è un'analisi di dati di fisica delle particelle. L'obbiettivo è il monitoraggio e l'ottimizzazione dell'allineamento del rivelatore di vertici di decadimento dell'esperimento Belle II, al fine di migliorare le prestazioni di ricostruzione di traiettorie di particelle cariche (tracce).
L'esperimento Belle II si propone di studiare miliardi di decadimenti di mesoni B e D e leptoni τ, prodotti in collisioni elettrone-positrone a 10.58 GeV di energia, per cercare segni indiretti di dinamica oltre il modello standard. L'accurato allineamento del rivelatore di vertice è un aspetto di primaria importanza per la corretta ricostruzione dei suddetti decadimenti, frequentemente caratterizzati dalla presenza di particelle cariche negli stati finali.
Ho simulato configurazioni di disallineamento attraverso un codice dedicato, e ne ho osservato gli effetti sulla procedura di ricostruzione, per mezzo di variabili di test appositamente sviluppate da me. Tali variabili utilizzano i parametri di traccia ricostruiti e sono pensate per essere specialmente sensibili a configurazioni di disallineamento scarsamente riconoscibili attraverso le procedure standard esistenti, che diventano, con il mio lavoro, identificabili in maniera rapida ed efficiente. Grazie a questi risultati, il mio lavoro sarà incluso nelle procedure standard per il monitoraggio dell'allineamento del rivelatore di vertice di Belle II.

Contents

1 Introduction **5**

2 Quark flavor physics at Belle II **6**
2.1 Introduction 6
2.2 Role of quark flavor in the development of the Standard Model 7
2.3 Flavor physics in the Standard Model 8
2.4 CP violation in the SM 11
2.5 Flavor changing neutral currents to probe non-SM dynamics 12
2.6 Current status of flavor physics 13

3 The Belle II detector at SuperKEKB **17**
3.1 The SuperKEKB e^+e^- collider 17
3.2 The Belle II detector 20
3.3 Vertex detector 22
3.3.1 Pixel vertex detector 22
3.3.2 Silicon vertex detector 23
3.4 Central drift chamber 24
3.5 Other detectors 25
3.5.1 Electromagnetic calorimeter 26
3.5.2 K_L^0 and muon detector 26
3.6 Trigger and data acquisition 27
3.7 Offline processing and simulation 29
3.8 Schedule 30

4 Charged particle tracking **32**
4.1 Track reconstruction 32
4.1.1 Including noise 36
4.1.2 Including multiple scattering 37
4.2 Tracks in Belle II 38
4.2.1 Transverse impact parameter 39
4.2.2 Azimuthal angle 39

4.2.3 Curvature . . . 40
4.2.4 Polar angle . . . 40
4.2.5 Longitudinal impact parameter . . . 41
4.3 Standard VXD alignment . . . 42
4.3.1 VXD geometry . . . 42
4.3.2 Alignment . . . 43

5 Baseline checks against macroscopic misalignments 46
5.1 Strategy . . . 46
5.2 Preliminary checks . . . 47
5.3 Event selection . . . 50
5.4 Differences in charge-specific distributions . . . 52
5.4.1 Transverse impact parameter . . . 52
5.4.2 Azimuthal angle . . . 54
5.4.3 Curvature . . . 56
5.4.4 $\tan\lambda$ . . . 57
5.4.5 Longitudinal impact parameter . . . 57
5.5 A novel variable: minimum track distance . . . 59

6 Weak misalignment configurations 63
6.1 Origin of weak modes . . . 63
6.2 Weak mode description and simulation . . . 65
6.3 Weak mode detection . . . 75
6.3.1 Signal-only data . . . 76
6.3.2 Including background . . . 84

7 Detecting misalignments through overlapping sensors 86
7.1 Coordinate-residual differences . . . 86
7.2 Results . . . 88

8 First look at data and summary 93

Chapter 1

Introduction

My thesis work is a data analysis project targeted at monitoring, calibrating and optimizing the Belle II performances in reconstructing charged particle trajectories (tracks).

Belle II [1] is a modern particle physics experiment designed to study billions of B, D and τ decays produced in energy-asymmetric electron-positron collisions at the SuperKEKB collider [2], starting in early 2019. The experiment offers the opportunity to perform low-background measurements of many processes sensitive to possible contributions from non-Standard-Model particles. The approach is based on comparing precise measurements of lower-energy processes and Standard-Model predictions, thus probing energies much higher than those directly attainable in hadron collisions.
The decays targeted at Belle II are dominated by the presence of final-state charged particles, and therefore precise tracking with accurate and precise momentum and impact parameter determination is essential for the success of the experiment. The more precisely the tracks are measured, the more accurately we can determine properties of their parents and their dynamics.

When I started my thesis work, collider data were not yet available, I therefore used simulated $e^+e^- \to \mu^+\mu^-$ data to develop novel, original procedures to identify misalignments of the vertex detector in a fast and efficient fashion. This thesis is organized as follows: Chapter 2 introduces the physics of Belle II; Chapter 3 describes the Belle II detector and the SuperKEKB collider; in Chapter 4 my work is introduced, with an overview of charged-particle tracking at Belle II; Chapter 5 introduces an original procedure developed to quickly detect macroscopic misalignments of the vertex detector; Chapter 6 describes the development of a procedure to identify specific misalignments of the vertex detector that are poorly detected by standard alignment algorithms; Chapter 7 explores novel approaches to identify misalignments based on measurement-hits from tracks traversing azimuthally-overlapping sensors at same radius; Chapter 8 gives a summary of the work, along with first plots on experimental data.

Chapter 2

Quark flavor physics at Belle II

This chapter offers a brief introduction to quark-flavor physics. The exploration of this sector at high precision is the primary motivation for the Belle II experiment, where I conducted my thesis work. Some details about the Belle II physics program are also discussed.

2.1 Introduction

The Standard Model (SM) [3], [4], [5] is, at the current level of experimental precision and at the energies reached so far, the theory that best describes fundamental particles interactions. Despite its success as an effective theory, the SM is still unable to answer many open questions. For instance, it does not include gravity and, therefore, cannot be valid at energy scales approaching $m_{Planck} \approx 10^{19}$ GeV; it does not allow for neutrino masses; it does not explain the apparently fine-tuned value of the Higgs boson mass; it does not describe dark matter and dark energy; nor it explains the matter/antimatter asymmetry of the universe which is directly linked to the phenomenon of charge-parity violation.

Flavor physics and the phenomenon of the violation of charge (C) and parity (P) symmetries (CP violation) have been giving essential contributions to the building and development of the Standard Model (SM) and still hold a prominent role in it, as most of the SM parameters relate to flavor and offer far-reaching windows into the search for non-SM physics.

The SM picture of CP violation has been conclusively established in 2001, with the observation of CP violation in B meson decays [6], [7]. In recent years, the mission of flavor physics has therefore moved toward the precise measurement of SM parameters as probes for deviations from predictions that could indicate contributions from non-SM dynamics.

This approach, in fact, allows for probing energy scales beyond the direct reach of high energy collisions such as those studied at the Large Hadron Collider (LHC). Even in the absence of such deviations, accurate measurements of flavor and CP-violating processes impose precise constraints on non-SM models that will guide and inform future searches.

2.2 Role of quark flavor in the development of the Standard Model

When only three quarks where known ($u,\ d,\ s$), the lifetime of the neutron and the lifetime of strange particles, predicted using the muon lifetime and universal weak couplings, were different and too short, indicating that the coupling of the weak interactions was systematically different when measured in different processes. This led Cabibbo [8] to introduce the parameter θ_C, which contributes as $\cos\theta_C$ in the $d \to u$ transition and as $\sin\theta_C$ in the case of a $s \to u$ transition.
This idea found further completion in the GIM (Glashow, Iliopoulos, Maiani) mechanism [9], which was introduced to describe suppression of processes like $K^0 \to \mu^+\mu^-$; which were predicted by the Cabibbo mechanism to occur at measurable rates, but remained unobserved. The GIM model predicted the existence of the fourth quark c [10] and finally led to the interpretation of θ_C as a rotation angle between the quark flavor eigenstates (d, s) and the weak eigenstates of the Hamiltonian (d', s'),

$$\begin{pmatrix} d' \\ s' \end{pmatrix} = \begin{pmatrix} \cos\theta_{\mathrm{C}} & \sin\theta_{\mathrm{C}} \\ -\sin\theta_{\mathrm{C}} & \cos\theta_{\mathrm{C}} \end{pmatrix} \begin{pmatrix} d \\ s \end{pmatrix}. \tag{2.1}$$

Thus, only using the weak eigenstates, the coupling is $u \leftrightarrow d'$, $c \leftrightarrow s'$. The discovery of the charm quark through the J/ψ resonance [11], [12] supported the GIM mechanism's prediction.
However, this model was still lacking a consistent explanation for the violation of CP symmetry observed in 1964 in kaon oscillations by Cronin, Fitch and collaborators [13]. A suitable explanation was proposed by Kobayashi and Maskawa [14] in 1973 by postulating a third generation of quarks (t, b) and extending the Cabibbo matrix to a 3×3 matrix, which allowed for the presence of an irreducible complex phase δ that could be responsible for CP violation.
Since the 80ies, many experiments studied CP violation in bottom-meson dynamics. CLEO [15], at Cornell (USA), ARGUS [16] at DESY (Germany), and Mark II [17] at SLAC (USA) made important advances on the pysics of B mesons, but none could observe CP violation in B decays.
A major boost to the study of CP violation came with the introduction of the "B-Factory" concept [18], which led to the BaBar experiment (1999-2008) at the PEP II accelerator (SLAC, USA) and the Belle experiment (1999-2010) at the KEKB collider (KEK, Japan).

In 2001, these experiments performed the first measurements of decay-time-dependent CP violation in B decays, showing that CP violation was genuinely a feature of weak interactions and not a peculiarity of kaon-mixing. These experiments, in addition, performed many other measurements of observables related to B meson dynamics, which helped constraining the Kobayashi-Maskawa description [14] as the leading source of CP violation.
In 2010, the Belle collaboration moved towards an improvement of the detector and of KEKB, which led to the development of the Belle II detector at SuperKEKB.
Since early 2001, flavor physics has also been studied successfully in hadron collisions by experiments like D0 and CDF [19] at the Tevatron (Fermilab, USA) and, later, CMS [20], ATLAS [21] and mostly LHCb [22] at LHC (CERN, Switzerland).

2.3 Flavor physics in the Standard Model

Flavor physics aims at describing the interactions between the various types (*flavors*) of particles that are subject to the same set of interactions, in order to explore the underlying dynamics of flavor symmetry breaking in the SM.
The SM is a gauge theory with gauge group $SU(3) \times SU(2) \times U(1)$. The $SU(3)$ symmetry describes the strong interactions of quarks and gluons and $SU(2) \times U(1)$ is the gauge symmetry of electroweak interactions. Within the unbroken $SU(3) \times U(1)$ gauge group, there are four different types of particles, each coming in three flavors:

- Up-type quarks in the $(3)_{+2/3}$ representation: $u,\ c,\ t$;
- Down-type quarks in the $(3)_{-1/3}$ representation: $d,\ s,\ b$;
- Charged leptons in the $(1)_{-1}$ representation: $e,\ \mu,\ \tau$;
- Neutrinos in the $(1)_0$ representation: $\nu_1,\ \nu_2,\ \nu_3$;

In the notation $(n)_j$, n represents the dimension of the group representation and j the conserved e.m. charge. In the SM, the left-handed quarks are arranged in doublets of the $SU(2)$ weak interactions,

$$q_L^i = \begin{pmatrix} u_L \\ d_L \end{pmatrix}, \begin{pmatrix} c_L \\ s_L \end{pmatrix}, \begin{pmatrix} t_L \\ b_L \end{pmatrix}, \tag{2.2}$$

while the right-handed quarks are introduced as $SU(2)$ singlets,

$$u_R^i = (u_R, c_R, t_R), \qquad d_R^i = (d_R, s_R, b_R). \tag{2.3}$$

Similarly, for leptons we have

$$l_L^i = \begin{pmatrix} \nu_{eL} \\ e_L \end{pmatrix}, \begin{pmatrix} \nu_{\mu L} \\ \mu_L \end{pmatrix}, \begin{pmatrix} \nu_{\tau L} \\ \tau_L \end{pmatrix}, \qquad e_R^i = (e_R, \mu_R, \tau_R). \tag{2.4}$$

A fundamental ingredient of the Standard Model is the Higgs field H [23], [24] which has a vacuum expectation value (VEV) assumed to be

$$\langle H \rangle = \frac{1}{\sqrt{2}} \begin{pmatrix} 0 \\ v \end{pmatrix}. \tag{2.5}$$

The quark couplings to the gluons, the weak gauge bosons $W^{\pm}$ and Z, and the photon, are described by the kinetic term in the following Lagrangian:

$$\mathcal{L}_{\text{ferm.}} = \sum_{i=1}^{3} \bar{q}_L^i i \not{D}_q q_L^i + \bar{u}_R^i i \not{D}_u u_R^i + \bar{d}_R^i i \not{D}_d d_R^i, \tag{2.6}$$

with covariant derivatives

$$D_{q,\mu} = \partial_\mu + i g_s T^a G_\mu^a + i g \tau^a W_\mu^a + i g' Q_q^Y B_\mu, \tag{2.7}$$

$$D_{u,\mu} = \partial_\mu + i g_s T^a G_\mu^a + i g' Q_u^Y B_\mu, \tag{2.8}$$

$$D_{d,\mu} = \partial_\mu + i g_s T^a G_\mu^a + i g' Q_d^Y B_\mu, \tag{2.9}$$

and hyper-charges $Q_q^Y = 1/6,\ Q_u^Y = 2/3,\ Q_d^Y = -1/3$. The symbols $T^a (a = 1, ..., 8)$ and $\tau^a (a = 1, 2, 3)$ indicate the generators of the $SU(3)$ and $SU(2)$ groups, respectively. Flavor non-universality is induced by the Yukawa couplings between the quarks and the Higgs field, which is responsible for the generation of quark masses,

$$\mathcal{L}_{\text{Yuk.}} = \sum_{i,j} \left(\lambda_{Uj}^i \tilde{H} \bar{q}_{Li} u_R^j + \lambda_{Dj}^i H \bar{q}_{Li} d_R^j + \lambda_{Ej}^i H \bar{l}_{Li} e_R^j + h.c. \right), \tag{2.10}$$

where the hermitian conjugate of the Higgs field $\tilde{H} = i\tau^2 H^*$appears. In compact form, the equation reads as

$$\mathcal{L}_{\text{Yuk.}} = -\tilde{H} \bar{q}_L \lambda_U u_R - H \bar{q}_L \lambda_D d_R - H \bar{l}_L \lambda_E e_R + h.c. \tag{2.11}$$

Without Yukawa interactions ($\lambda_U = \lambda_D = \lambda_E = 0$), the SM Lagrangian has a global symmetry because only the covariant kinetic energy terms $\sum_n \bar{\psi}_n i \not{D} \psi_n$ are left. Unitary transformations on the fields leave this Lagrangian unaffected.

However, in nature, we have the Yukawa couplings to the Higgs field. If we replace the Higgs field with its VEV in Eq. (2.11) we obtain the mass terms for quarks and leptons,

$$\mathcal{L}_m = -\frac{v}{\sqrt{2}}\bar{u}_L\lambda_U u_R - \frac{v}{\sqrt{2}}\bar{d}_L\lambda_D d_R - \frac{v}{\sqrt{2}}\bar{e}_L\lambda_E e_R + h.c. \tag{2.12}$$

A field redefinition diagonalizes the mass matrices and keeps unchanged the kinetic terms. The redefinition can only be linear (to keep the model renormalizable) and it must commute with the gauge symmetry $U(1) \times SU(3)$ (electromagnetism and color), which is preserved in the spontaneous symmetry breaking that follows the introduction of the VEV. Then, this linear transformation can only mix quarks (and leptons) with same charge and helicity,

$$u_R \to V_{u_R} u_R,\ u_L \to V_{u_L} u_L,\ d_R \to V_{d_R} d_R,\ d_L \to V_{d_L} d_L. \tag{2.13}$$

By requiring that the transformations diagonalize the mass terms, we have

$$V_{u_L}^\dagger \lambda_U V_{u_R} = \lambda'_U, \quad V_{d_L}^\dagger \lambda_D V_{d_R} = \lambda'_D, \tag{2.14}$$

where the matrices λ'_U and λ'_D are diagonal, real and positive. Then, the Lagrangian containing the mass terms becomes

$$\mathcal{L}_m = -\frac{v}{\sqrt{2}}(\bar{u}\lambda'_U u + \bar{d}\lambda'_D d + \bar{e}\lambda_E e), \tag{2.15}$$

where we identify the diagonal mass matrices $m_U = v\lambda'_U/\sqrt{2}$, $m_D = v\lambda'_D/\sqrt{2}$ and $m_E = v\lambda_E/\sqrt{2}$. The field redefinitions of Eq. (2.13) yield an additional term in the gauge interactions part

$$\frac{g}{\sqrt{2}}\bar{u}_L(V_{u_L}^\dagger V_{d_L})\not{W}^+ d_L + \frac{g'}{\sqrt{2}}\bar{d}_L(V_{d_L}^\dagger V_{u_L})\not{W}^- u_L. \tag{2.16}$$

The redefinition relic that appears in the form of a unitary matrix,

$$V_{\text{CKM}} = V_{u_L}^\dagger V_{d_L} = \begin{pmatrix} V_{ud} & V_{us} & V_{ub} \\ V_{cd} & V_{cs} & V_{cb} \\ V_{td} & V_{ts} & V_{tb} \end{pmatrix}, \tag{2.17}$$

is called Cabibbo-Kobayashi-Maskawa (CKM) matrix. The standard parametrization of the CKM matrix involves three mixing angles θ_{12}, θ_{23}, θ_{13} and an irreducible complex phase δ, allowed by the angles θ_{ij}, as flavor parameters:

$$V_{\text{CKM}} = \begin{pmatrix} c_{12}c_{13} & s_{12}c_{13} & s_{13}e^{-i\delta} \\ -s_{12}c_{23} - c_{12}s_{23}s_{13}e^{i\delta} & c_{12}c_{23} - s_{12}s_{23}s_{13}e^{i\delta} & s_{23}c_{13} \\ s_{12}s_{23} - c_{12}c_{23}s_{13}e^{i\delta} & -c_{12}s_{23} - s_{12}c_{23}s_{13}e^{i\delta} & c_{23}c_{13} \end{pmatrix}. \tag{2.18}$$

Experiments found that the CKM matrix shows a distinctive hierarchy, where

$$s_{12} \sim 0.2, \quad s_{23} \sim 0.04, \quad s_{13} \sim 4 \cdot 10^{-3}. \tag{2.19}$$

Hence the CKM matrix approximates the identity matrix, resulting in strongly suppressed flavor changing processes. The lack of a more fundamental theory that might explain this hierarchy is one of the open questions of the SM ("flavor hierarchy problem").

2.4 CP violation in the SM

The CKM angles θ_{ij} of the CKM matrix parametrize the amount of flavor mixing between quarks of different generations. Weak interactions violate both charge and parity because these transformations affect differently left and right-handed quarks. A CP transformation (namely a combination of C and P) connects left-handed quarks to right-handed anti-quarks.
The Lagrangian describing the charged-current interactions via the $W^{\pm}$ bosons transforms as follows under a CP-transformation,

$$\mathcal{L}_{c.c} = \frac{g}{\sqrt{2}} V_{ik} \bar{u}_{Li} \gamma_\mu W^{\mu+} d_{Lk} + \frac{g}{\sqrt{2}} V_{ik}^* \bar{d}_{Lk} \gamma_\mu W^{\mu-} u_{Li}; \tag{2.20}$$

$$\mathcal{L}_{c.c} \xrightarrow{\text{CP}} \frac{g}{\sqrt{2}} V_{ik}^* \bar{d}_{Lk} \gamma_\mu W^{\mu-} u_{Li} + \frac{g}{\sqrt{2}} V_{ik}^* \bar{u}_{Li} \gamma_\mu W^{\mu+} d_{Lk}. \tag{2.21}$$

Then CP-conjugation transforms the CKM element V_{ik} into its complex conjugate. Hence, any non-vanishing complex phase in the quark-mixing couplings results in CP-violating interactions.

Flavor hierarchy is more transparently visualized by turning to the Wolfenstein parametrization [25] of the CKM matrix, which consists in expanding flavor violations in powers of λ

$$V_{\text{CKM}} = \begin{pmatrix} 1 - \frac{\lambda^2}{2} & \lambda & A\lambda^3(\rho - i\eta) \\ -\lambda & 1 - \frac{\lambda^2}{2} & A\lambda^2 \\ A\lambda^3(1 - \rho - i\eta) & -A\lambda^2 & 1 \end{pmatrix} + O(\lambda^4), \tag{2.22}$$

where $\lambda = |V_{us}| \approx 0.2$, while $A, \rho, \eta \approx O(1)$.

The CKM matrix is unitary, with 18 parameters of which only 4 are independent. They are linked by relations that are tested in experiments, like

$$V_{ud}V_{ub}^* + V_{cd}V_{cb}^* + V_{td}V_{tb}^* = 0, \tag{2.23}$$

which is represented on the complex plane by the so-called "Unitarity Triangle".

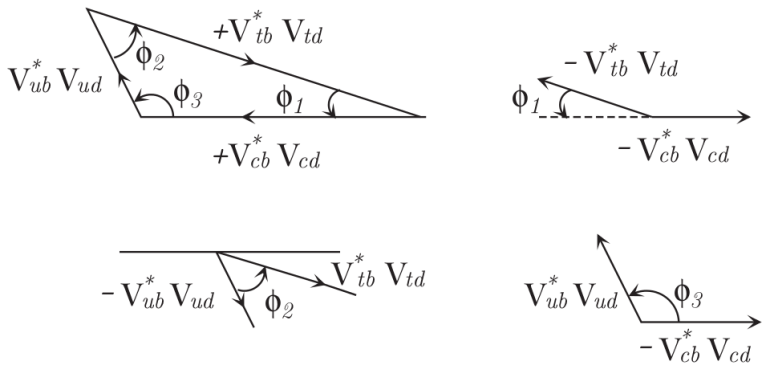

Figure 2.1: Unitarity triangle: the angles of the Unitarity Triangle are related to the Kobayashi-Maskawa phases of the CKM matrix.

If the base of the triangle is normalized to unity, then the remaining sides will be

$$R_b = \frac{|V_{ud}V_{ub}^*|}{|V_{cd}V^*cb|} = \left(1 - \frac{\lambda^2}{2}\right)\frac{1}{\lambda}\frac{|V_{ub}|}{|V_{cb}|}, \tag{2.24}$$

$$R_t = \frac{|V_{td}V_{tb}^*|}{|V_{cd}V_{cb}^*|} = \frac{1}{\lambda}\frac{|V_{td}|}{|V_{cb}|}. \tag{2.25}$$

The Unitarity Triangle sides and angles are measured in flavor-changing processes involving K and B mesons. The side R_b and the angle ϕ_3 are measured in B decays dominated by charged-current interactions. R_t and ϕ_1 depend on CKM elements involving the top quark. They can only be measured in processes governed by a flavor-changing-neutral current loop.

2.5 Flavor changing neutral currents to probe non-SM dynamics

Flavor-changing processes are interactions where the initial and final flavor-numbers (the number of particles of a certain flavor minus the number of antiparticles of the same flavor) differ. In flavor-changing-charged-current processes, up-type and down-type flavors,

and/or both charged lepton and neutrino flavors are involved. Flavor changing charged currents occur at the leading perturbation order in the SM. The size of the interactions is related to the off-diagonal elements of the CKM matrix.
In flavor changing neutral current (FCNC) processes, either up-type or down-type flavors (but not both) and/or either charged lepton or neutrino flavors but not both, are involved. These processes are allowed at the tree level (the leading perturbation order) in the SM but are rather generated by loop diagrams with internal $W^{\pm}$ bosons, as illustrated in Figure 2.2.

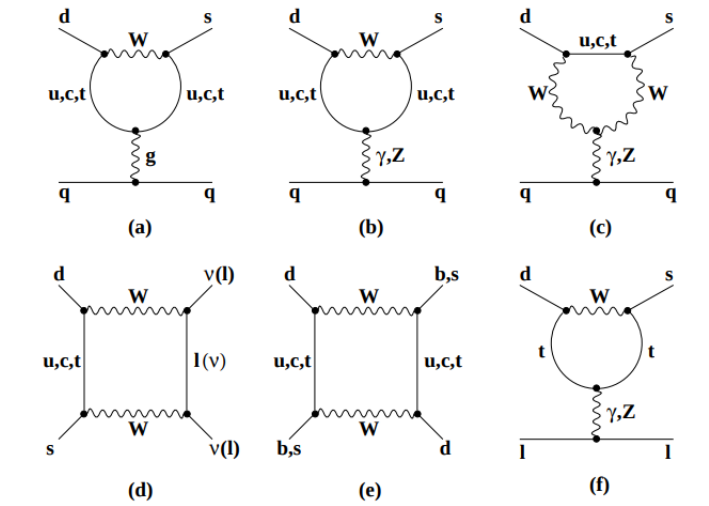

Figure 2.2: Typical penguin and box diagrams.

This makes FCNCs very sensitive to possible contributions from non-SM physics because any internal quark-line could be replaced by virtual non-SM particles with appropriate quantum numbers but arbitrarily high mass, which could sensibly alter the amplitudes. FCNCs therefore offer a powerful tool for identifying indirectly the contribution of non-SM particles by measuring departures from SM predictions in quantities associated with loops.
The high sensitivity of flavor physics to high energy scales motivates the current experimental effort to measure flavor parameters with unprecedented precision, in which the Belle II experiment is an important player.

2.6 Current status of flavor physics

In the past two decades, measurements from CLEO [15], NA48 [26], KTeV [27], BaBar [7], Belle [6], CDF [19] and LHCb [22] led to a detailed and precise determination of the Unitarity-Triangle sides and angles. These measurements have been combined in the

CKM-fit [28], which is a global fit of the CKM elements using all available theoretical and experimental constraints, thus allowing to compare the consistency of measurements with the theoretical model. This fit classifies the constraints in CP-conserving variables $(\Delta m_{B_d}, \Delta m_{B_s}, |V_{ub}|)$ and CP-violating variables $(\epsilon_K, \alpha, \beta, \gamma)$. An example of this fit is shown in Figure 2.3.
The overall picture is of striking consistency: the Cabibbo-Kobayashi-Maskawa interpretation of quark interactions is the leading explanation for all quark-flavor measurements performed so far.

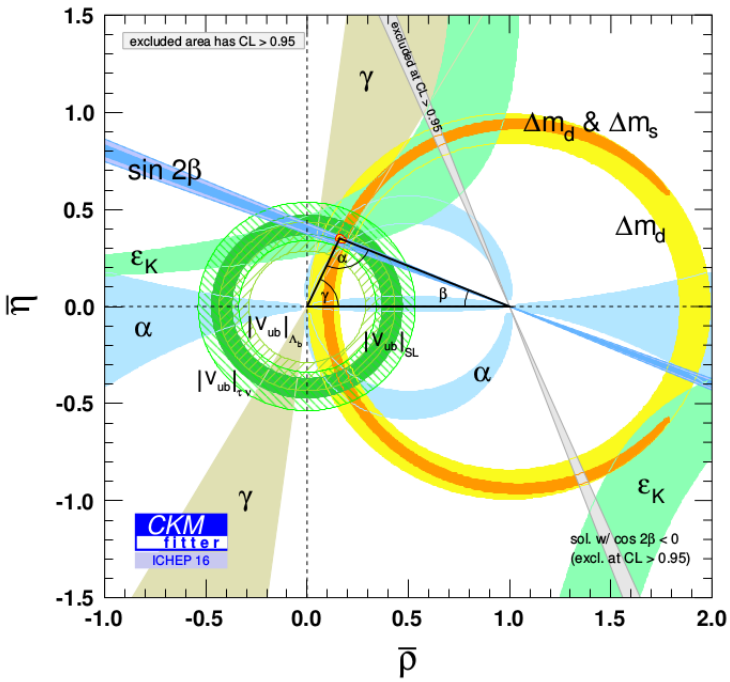

Figure 2.3: CKM fit on the $\bar{\rho} \times \bar{\eta}$ plane. Current constraints arising from CP-conserving $(\Delta m_{B_d}, \Delta m_{B_s}, |V_{ub}|)$ and CP-violating $(\epsilon_K, \alpha, \beta, \gamma)$ are shown.

However, a number of open fundamental questions associated to flavor remain, including the following [29]:

- *Are there additional CP violating phases indicating non-SM particles or interactions?* Insight on this question implies precise measurements of time dependent CP-violation in $b \to sss$ penguin decays (one-loop processes where a quark temporarily changes flavor, via a W or Z loop, and the flavor-changed quark is involved in some tree interaction). The comparison of time-dependent CP-violation parameters of penguin dominated $b \to sss$ decays (e.g., $B^0 \to \phi K_S^0$, $B^0 \to \eta' K_S^0$) with tree dominated $b \to c\bar{c}s$ decays ($B^0 \to J/\psi K_S^0$) is a powerful observable: in the SM, the

difference between these parameters is expected to vanish, but non-SM dynamics may contribute in the loops of $b \to sss$ decays and induce deviations.

- *Are there quark flavor-changing neutral currents beyond the SM?* FCNCs for $b \to s(d)$ decays are forbidden at the tree level and can only occur in loops. It is of great interest to measure $b \to s\nu\bar{\nu}$ transitions such as $B \to K^*\nu\bar{\nu}$, which are part of a class of decays with large unreconstructed final-state energies, because of the presence of neutrinos in final states. Moreover, it is of primary importance to improve FCNCs measurements of $b \to d$, $b \to s$ and $c \to u$ transitions. These kind of precise measurements of rare FCNC decays provide precision tests of the SM.

- *Are there sources of lepton-flavor violation (LFV) beyond the SM?* Large mixing between ν_μ and ν_τ, which has been observed in neutrino experiments, are leading to precise measurements to search for flavor changing processes like $\tau \to \mu\gamma$. LFV in charged lepton decays is also a key prediction in many neutrino mass generation mechanisms.

- *Does nature support multiple Higgs bosons?* Charged Higgs bosons, in addition to the neutral SM-like Higgs, have been predicted by many extensions of the SM. Charged Higgs are searched in flavor transitions to τ leptons, including $B \to \tau\nu$ and $B \to D^{(*)}\tau\nu$. The large mass of the τ lepton makes the $B \to D^{(*)}\tau\nu$ decay kinematics highly suppressed compared to the ordinary semi-leptonic B decays (with e or μ in the final state), but at the same time also sensitive to the possible charged Higgs contributions. These processes are expected to be more sensitive to the charged Higgs sector than the semi-leptonic K decay processes, because the Higgs couplings to fermions are proportional to the fermion mass.

- *Does non-SM physics enhance CP violation via $D^0 - \bar{D}^0$ mixing to an observable level?* The first evidence for $D^0 - \bar{D}^0$ mixing was obtained in 2007. CP-violation in the system has not been observed yet. The predicted rate within the SM is very small and an observation of CP-violation could indicate the contribution of non-SM physics.

A dedicated experimental effort is devoted to gain insight on these questions, led by Belle II at SuperKEKB and LHCb at LHC. At LHCb large samples of B mesons are produced via incoherent QCD production of $b\bar{b}$ pairs from high-energy pp collisions. At Belle II, e^+e^- collisions produce $B\bar{B}$ pairs from the decay of $\Upsilon(4S)$ mesons at threshold. High-energy pp collisions produce bottom and charm hadrons with cross sections of approximately 1-100 μb, hence at rates 1000 to 100000 times higher than in B-factories. However, events at Belle II are less degraded by backgrounds with respect to LHCb events, because no additional particles are produced in $B\bar{B}$ events, while at LHCb the composite nature of the colliding hadrons and the large extra energy available after the

collision yields all kind of hadrons (Figure 2.4).
These two experiments are complementary. LHCb can produce all types of b-hadrons at higher rates and explore mainly final states using only tracks. Belle II has better sensitivity to B and D decays into final states with neutral particles because it relies on beam-energy constraints and has low-background events.

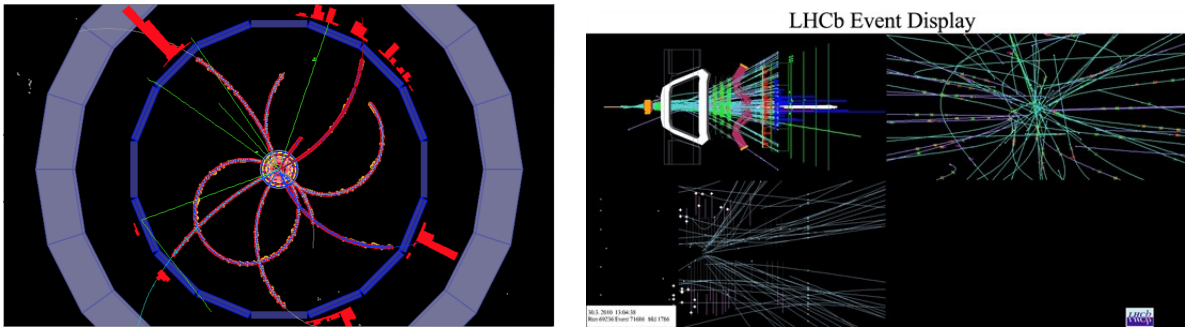

(a) Belle II (b) LHCb

Figure 2.4: Event display for Belle II (a) and LHCb (b).

The main goals of Belle II are to look for non-Standard Model physics in the flavor sector at the intensity frontier in sinergy and competition with LHCb for the next decade.

Chapter 3

The Belle II detector at SuperKEKB

The Belle II experiment is the upgraded successor of the Belle experiment. It consists of upgraded systems together with newly developed detectors. High SuperKEKB luminosity and advanced detection technologies will allow for unique sensitivity to a broad class of quantities that are sensitive to non-SM physics and not accessible competitively by hadron-collider experiments. This chapter discusses the SuperKEKB collider and Belle II sub-detectors, with particular attention to the tracking system, which is more closely connected to my thesis work.

3.1 The SuperKEKB e^+e^- collider

SuperKEKB is a state-of-the-art high-luminosity electron-positron collider with asymmetric energies [2], designed to produce collisions corresponding to an integrated luminosity of 80 ab^{-1} in five years. The collider provides a low-background environment for production of $B\bar{B}$ pairs ($B^0\bar{B}^0$ or B^+B^-) via decays of $\Upsilon(4S)$ mesons produced at threshold. The expected integrated luminosity will correspond to samples of approximately 55 billion $B\bar{B}$ pairs, 47 billion $\tau^+\tau^-$ pairs and 65 billion $c\bar{c}$ pairs.

SuperKEKB is a B-factory. This kind of particle collider was targeted at CP-violation measurements in the B^0 system, in particular, to CP asymmetry in the "golden mode" decay $B^0 \to J/\psi K^0_S$. At the B-factories, B mesons are created in pairs at the center-of-mass energy corresponding to the $\Upsilon(4S)$ mass. The $B\bar{B}$ pair is in a p-wave entangled state, until one of the two mesons decays. When neutral mesons are produced, the decay may occur into a final state that distinguishes between B^0 and $\bar{B}^0$, thus projecting the accompanying B meson onto the opposite b-flavor at that time; afterwards the accompanying meson evolves independently.
The baseline requirements for a second-generation B-factory experiment are

- High luminosity: the FCNC processes are suppressed in the SM and therefore rare. Thus, large samples of $B\bar{B}$ pairs are needed.

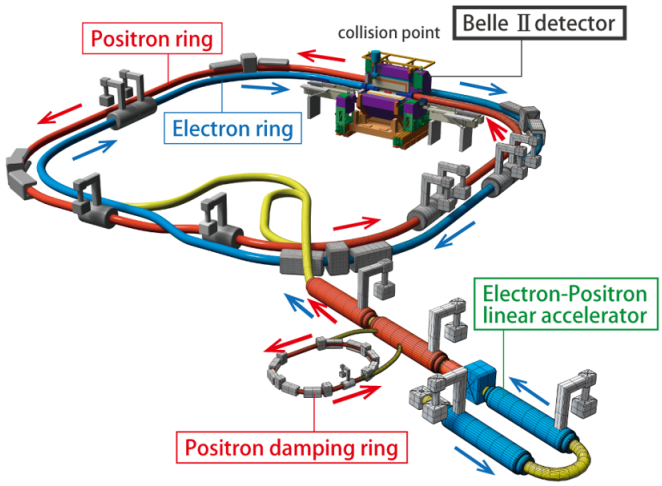

Figure 3.1: Schematic view of SuperKEKB: relevant accelerator components that produce and deliver electrons and positrons to the interaction point are shown.

- Boosted $B\bar{B}$ pairs: The B and $\bar{B}$ mesons must have decay lengths in the laboratory that are sufficiently long to infer the time of their decays. The $\Upsilon(4S)$ mesons produced at threshold in energy-symmetric colliders are at rest in the laboratory frame and the resulting $B\bar{B}$ pair is, in turn, nearly at rest in the $\Upsilon(4S)$ frame because $m_{\Upsilon(4s)} - 2mB^0 \simeq 19$ MeV. If the $B\bar{B}$ pair is at rest, then decay time cannot be measured and therefore decay-time dependent asymmetries remain unaccessible. This suggested the proposal for asymmetric beam energies, resulting in a boost for the $\Upsilon(4S)$ and, consequently, in $B\bar{B}$ pairs boosted along the z-direction in the laboratory frame. This allows for indirect measurement of the decay times difference Δt using the displacement in z between the decay vertices of the two B mesons.

SuperKEKB meets these requirements by means of a double-ring energy-asymmetric collider. The positron energy is 4 GeV (LER, for low energy ring) and that of the electrons is 7 GeV (HER, for high energy ring).

Simultaneous and continuous injection is necessary to provide SuperKEKB with a constant luminosity, given the short beam lifetime due to degradation of the beam quality caused by interactions within and between the beams, and between beams and residues of gas in the beam pipe. Further requirements are a shorter beam intensity per pulse and low emittance (a measure of the average spread of particle coordinates in position and momentum phase space) for both electrons and positrons because the beam-lifetime will be very short and the injection aperture will be small. A photo-cathode radio-frequency gun is used to produce electrons and a flux concentrator (a device providing an external

magnetic field after the target to increase the positron yield) is used to produce positron beams. Since the positrons from the flux concentrator have a large emittance, a damping ring (a collector ring that accepts the beam with a large energy spread and a large transverse emittance) applies an appropriate combination of synchrotron radiation in bending fields with energy gain in radio-frequency cavities, to reduce the positron emittance.
The positron beam is accelerated up to 1.1 GeV by a linear accelerator and extracted to be injected into the damping ring. The positron beam is injected again into the linear accelerator, then accelerated up to 4 GeV and injected to the LER. After production, electrons are accelerated to 7 GeV by the linear accelerator and injected to HER.

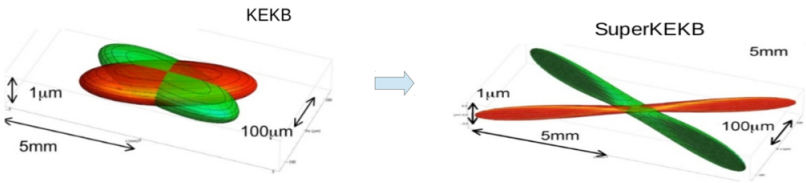

Figure 3.2: Sketch of the luminous region in KEKB (left) and SuperKEKB (right) at the interaction point.

A nano-beam large-angle crossing angle collision scheme is used [30]. This is an innovative scheme based on a large crossing angle and small horizontal and vertical emittance. The configuration of the nano-beam crossing mirrors a collision with many short micro bunches allowing a significant advantage in luminosity compared to standard schemes. The luminous region is reduced to a twentieth with respect to the previous accelerator KEKB, which, combined with doubled beam currents, result in a factor of 40 gain in intensity.

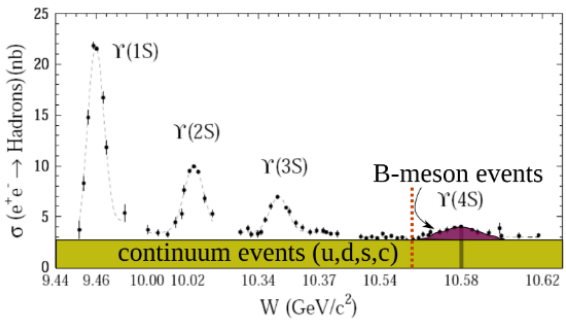

Figure 3.3: e^+e^- cross section in the $\Upsilon(1S) - \Upsilon(4S)$ region as a function of the center-of-mass energy. The red dashed line marks the kinematic threshold for the production of $B\bar{B}$ pairs.

Particles produced in a collision fly from the interaction point (IP) into the volume of

Process	**Cross Section [nb]**
$e^+e^- \to \mu^+\mu^-$	1.148 ± 0.005 (full angle)
$e^+e^- \to \tau^+\tau^-$	0.919 ± 0.003 (full angle)
$e^+e^- \to e^+e^-(\gamma)$	294 ± 2 (10-170 deg)
$e^+e^- \to \gamma\gamma(\gamma)$	4.96 ± 0.02 (10-170 deg)
$e^+e^- \to e^+e^-e^+e^-$	39.74 ± 0.03 (full angle)
$e^+e^- \to e^+e^-\mu^+\mu^-$	18.87 ± 0.02 (full angle)
$e^+e^- \to u\bar{u}(\gamma)$	1.605 (full angle)
$e^+e^- \to d\bar{d}(\gamma)$	0.401 (full angle)
$e^+e^- \to s\bar{s}(\gamma)$	0.383 (full angle)
$e^+e^- \to c\bar{c}(\gamma)$	1.329 (full angle)
$e^+e^- \to \Upsilon(4S) \to B^+B^-$	0.5346 (full angle)
$e^+e^- \to \Upsilon(4S) \to B\bar{B}^0$	0.5654 (full angle)

Table 3.1: Total cross sections from various physics processes from collisions at $\sqrt{s} =$ 10.573 GeV.

the Belle II detector. In the collision, many fundamental processes can happen, depending on the corresponding cross sections, listed in Table 3.1. The $e^+e^- \to$ hadrons cross section, which is most relevant for the physics of Belle II, is shown in Figure 3.3 as a function of the center-of-mass energy.

3.2 The Belle II detector

The Belle II detector consists of a set of sub-detectors, each designed for a specific purpose. Three tracking sub-detectors are located in the center of the detector, and immersed in a 1.5 T axial magnetic field generated by a solenoid, to reconstruct the trajectories of charged particles (tracks). The pixel and silicon vertex detector (PXD, SVD) are used to measure charged particle momenta and to reconstruct decay vertices and low-momentum tracks that do not reach the central drift chamber (CDC). The PXD is a new detector, not previously present in Belle, while the SVD has been upgraded.

The CDC samples charged-particles trajectories, from which charge, momentum and energy loss by ionization are determined. It was present in the Belle detector and has been upgraded. The three tracking sub-detectors are surrounded by a time-of-propagation (TOP) detector, which is a new version of an existing detector. This measures the flight-time of charged particles, which, combined with momentum information, allows to infer their mass and identifies charged particles. An electromagnetic calorimeter (ECL), already present in Belle, follows, that measures the energy of electromagnetically interacting particles, photons and electrons in particular. The purpose of the K_L^0 and muon detector (KLM), the outermost detector layer, which has been upgraded with respect to Belle, is

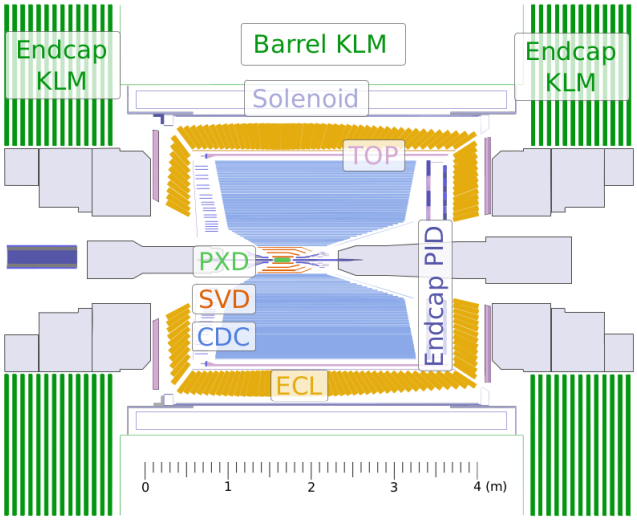

Figure 3.4: Longitudinal cross section of the Belle II detector. The polar asymmetry of the apparatus mirrors the asymmetric acceptance due to energy-asymmetric collisions.

to identify K_L^0 mesons and muons.

Belle II adopts a Cartesian, right-handed coordinate system (Figure 3.5), with origin at the nominal interaction point and axes as follows: the z-axis points along the direction of the magnetic field, which is also the direction of the HER (forward); the y-axis points upwards, in the direction of the detector hall roof; and the x-axis points along the radial direction outwards of the accelerator ring.

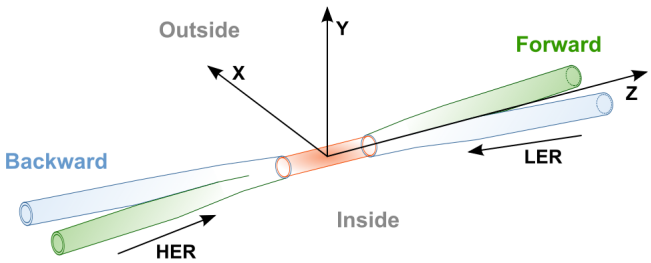

Figure 3.5: The Belle II coordinate system.

If not otherwise specified, all xy projections of the Belle II detector are drawn such that the detector is seen from the forward to the backward direction, with z-axis pointing out of the page, x-axis to the right, and y-axis upwards.

3.3 Vertex detector

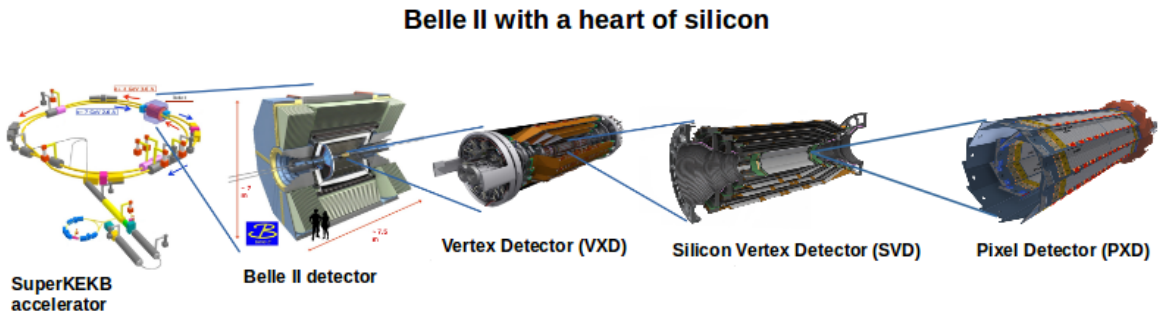

Figure 3.6: Sketch of the VXD and of its sub-detectors in Belle II.

The VXD provides precise measurements of tracks in the vicinity of the interaction point, thus allowing to reconstruct decay vertices of long-lived particles. The most important factors affecting the precision of the vertex-position determination are the distance of the first measured hit from the vertex, the spatial resolution of that hit, and the effect of multiple scattering. The VXD is composed of two complementary systems, the pixel vertex detector and the silicon vertex detector, for a total of 6 layers, 65 ladders and 212 sensors. An illustration of the VXD and of its components is shown in Figure 3.6.

3.3.1 Pixel vertex detector

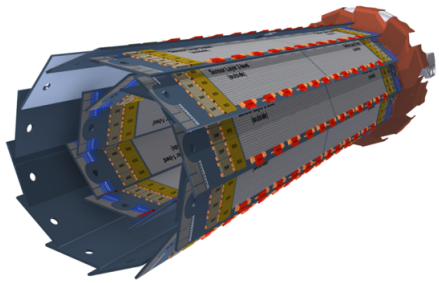

(a) Schematic view of the geometrical arrangement of the sensors for the PXD.

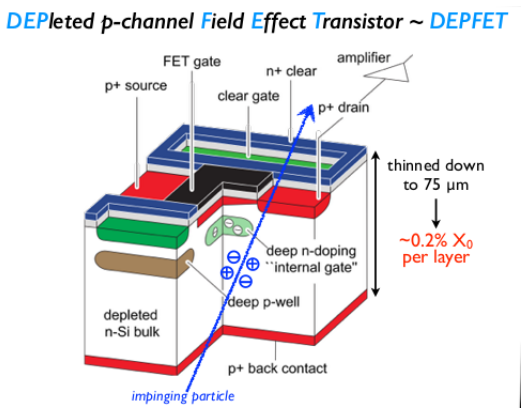

(b) Operating principle of a DEPFET.

Figure 3.7: Schematic description of the PXD detector.

The PXD [31] is used to reconstruct the spatial positions of B, D and τ decay vertices. It is made of pixel sensors that use the DEPFET (depleted field effect transistor) technology, a semiconductor detector concept combining detection and in-pixel amplification. It consists of two layers of sensors, at radii of 14 mm and 22 mm. The inner layer consists of 8 planar sensors (ladder), each 15 mm in width and with a sensitive length of 90 mm. The outer layer consists of 12 planar sensors with a width of 15 mm and a sensitive length of 123 mm.
The PXD position allows for vertex reconstruction with spatial resolution of $\sigma \approx 210$ μm, but the large quantum-electrodynamics background expected near the interaction point requires sensors to be radiation-hard. These requirements are met by the DEPFET technology.
DEPFET were invented in 1987 by Josef Kemmer and Gerhard Lutz [32]. A p-channel MOSFET (metal oxide semiconductor field effect transistor) or JFET (junction field effect transistor) is integrated on a silicon detector substrate, which is entirely depleted by a sufficiently high negative voltage. A potential minimum is formed by sideward depletion, which is shifted directly underneath the the transistor channel at a depth of about 1 μ by an additional phosphorus implantation under the external gate. Incident particles generate electron-hole pairs inside the fully depleted region. While the holes drift to the back contact, electrons are accumulated in the potential minimum, called internal gate. When the transistor is switched on, the electrons modulate the channel current.
Amplification of the signal charge occurring just above the position of its generation, avoids leakage due to lateral charge transfer. The most important feature of the DEPFET is the very small capacitance of the internal gate, which allows for measurements affected by low noise even at room temperature.

3.3.2 Silicon vertex detector

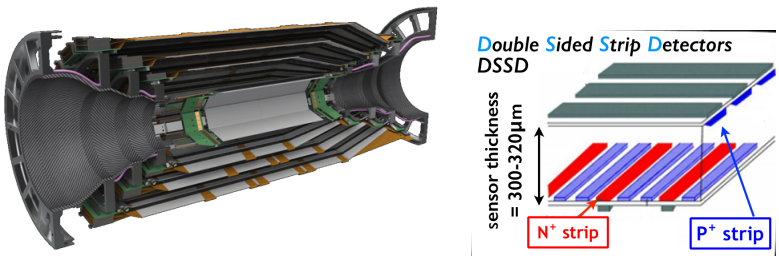

(a) Schematic view of the geometrical arrangement of the sensors for the SVD.

(b) Operating principle of a DSSD.

Figure 3.8: Schematic description of the SVD detector.

The SVD [33] provides two position measurements for traversing charged particles,

with expected spatial resolution of $\sigma \approx 20$ μm each. The SVD is placed between the pixel detector and the drift chamber, at 38 mm to 140 mm radii.
SVD is composed of four layers. The thickness of SVD sensors is 320 μm. Rectangular sensors are used in the barrel part and trapezoidal sensors in the forward region. All rectangular silicon sensors are double-sided with long strips on the $p-$side parallel to the beam axis (z direction). The $n-$side strips along $r-\theta$ are short and located on the sensor side facing outside of the detector.
The size of rectangular sensors in the third layer is 38.4×122.8 mm^2 and 57.6×122.8 mm^2 in layer 4, 5, and 6. The size of trapezoidal sensors is $38.4 - 57.6 \times 122.8$ mm^2.
When a charged particle passes through the sensor, electron-hole pairs are created along its path by ionization. Electrons are collected by n^- strips while holes by the p^+ strips. The sensor produces an electric signal and two coordinates of the particle position are read, the z direction by the $p-$side and $r-\theta$ direction by the $n-$side.

3.4 Central drift chamber

Surrounding the SVD is the CDC [34]. It has an inner radius of 16 cm and an outer radius of 113 cm and contains 14336 sense wires immersed in a 50% helium, 50% ethane gas volume. The CDC is used to reconstruct charged particles, to measure their momenta and to identify them using their specific ionization-energy deposits in the gas volume.
Charged particles passing through the gas lose part of their energy by ionization, producing electron-ion pairs that are separated by an electrical field applied by 42240 aluminum field wires, 126 μm in diameter, arranged in 56 layers. The sense wires are made of gold-plated tungsten and have 30 μm diameter.

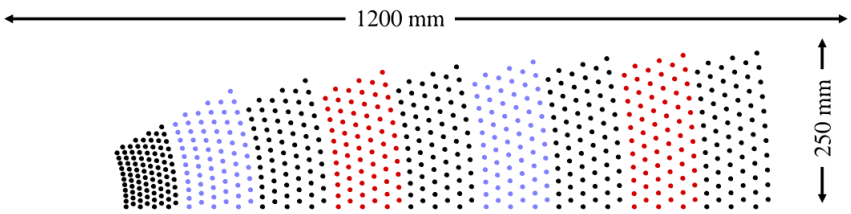

Figure 3.9: Cross-section of the CDC, with axial superlayers in black, stereo superlayers in magenta and red for positive and negative stereo angles, respectively.

Axial wires enable to reconstruct the track only in the $r-\phi$ plane. Information on the z direction comes from layers with sense wires tilted with respect to the z (from -74.0 mrad to 70.0 mrad) called *stereo layers*. The chamber has alternating superlayers, each made of six layers with the same orientation.
Axial superlayers (A) are followed by stereo superlayers (U) in turn followed by axial

superlayers. Stereo super layers (V) with a negative stereo angle follow in turn, to optimize the z resolution. The arrangement of the total 9 superlayers is AUAVAAUAVA. To reduce the impact of background, which is higher in the inner parts of the detector, the innermost superlayer is realized with a denser packing of wires. This so-called *small-cell chamber* consists of 8 layers instead of the usual 6, and has a lower per-cell occupancy than a superlayer with normal cell configuration.
The CDC provides hits with good spatial resolution ($\sigma_{r\phi} \approx 100$ μm and $\sigma_z \approx 2$ mm), it has a fairly low dead time and is also used for charged-hadron identification by specific energy loss (about 3σ separation between charged kaons and pions).

3.5 Other detectors

In addition, Belle II uses two technologies for particle identification.

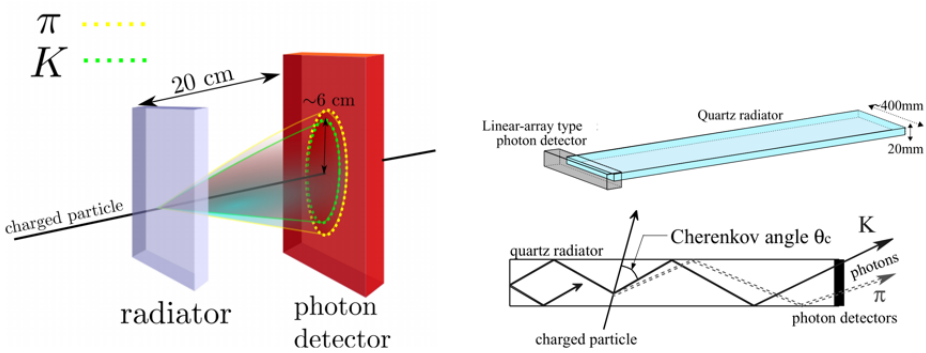

Figure 3.10: Principles of Belle II particle identification detectors: in the ARICH (left), the yellow Cherenkov ring on the photon detector is generated by pions and the green ring is produced by kaons. Design for a TOP bar (top-right) and a sketch showing the functionality of the TOP detector (bottom-right).

In the barrel region, the detection is based on the combination of time-of-flight and Cherenkov angle measurements. Incoming charged particles produce Cherenkov radiation in a quartz radiator and the generated photons are reconstructed using an array of photo-multipliers. The Cherenkov image is reconstructed from information provided by two coordinates (x, y) and precise timing, determined by micro-channel detectors at the surfaces of quartz bars. The time of propagation (TOP) counter [35] is made up of 32 quartz bars, each 20 mm $\times$ 450 mm $\times$ 1250 mm with two bars per module that measure the time of propagation of the Cherenkov photons, internally reflected inside a quartz

radiator. The expected charged kaon identification efficiency is greater than 90%, with charged pion misidentification probability smaller than 10%.
In the forward endcap, an aerogel ring-imaging Cherenkov detector (ARICH) ARICH [35] is installed to separate kaons from pions over most of their momentum spectrum and to identify charged particles with momentum smaller than 1 GeV/c. The is composed of an aerogel radiator for production of Cherenkov photons, an expansion volume for formation of Cherenkov rings and a photon detector. The ARICH consists of 420 modules for photon detection in seven layers and 248 aerogel tiles of wedge shape in four layers. The inner radius is 56 cm and outer radius is 114 cm. The ARICH K/π separation efficiency at 4 GeV/c is $\approx$ 96%.

3.5.1 Electromagnetic calorimeter

The ECL [36] allows for measurements of the energy of electromagnetic particles, the detection of neutral particles and luminosity measurements. The requirements are an high efficiency for photon detection and precise determination of particle energy. The ECL consists of a 3m-long barrel section with inner radius of 1.25 m and annular endcaps at z = 1.96 m (forward) and z = -1.02 m (backward) from the interaction point. The barrel compartment has a tower structure that geometrically projects to the interaction point. It consists of 6624 CsI(Tl) crystals in 29 distinct shapes. Each crystal is a truncated pyramid of about 6×6 cm^2 in cross sections and 30 cm in length. The endcaps consist of 2112 CsI crystals of 69 shapes. Photons and electromagnetic particles are detected using electromagnetic cascades. The cascades produce excitation of scintillator material, which is amplified and detected by photo-multipliers mounted at the end of each crystal. The number of photons is directly dependent on the energy released by an absorbed particle. The expected energy resolution is $\sigma(E)/E = 0.2\%/E \oplus 1.6\%/\sqrt[4]{E} \oplus 1.2\%$.

3.5.2 K_L^0 and muon detector

The KLM [37] is a sandwich structure of 4.7 cm thick iron plates with resistive plate chambers (RPC) in between.
RPCs consist of two planar glass sheets that act as high voltage electrodes, separated by a thin gas volume. Particles traversing this volume create ion-electron pairs that are accelerated by the electric field, producing a streamer between the two electrodes, which causes a voltage drop in the nearby electrodes. This voltage drop is detected by pick-up strips placed on either side of the chamber. The pick-up strips are a few centimeters wide and are arranged orthogonally on both sides, so that the particle track can be localized in z/ϕ for the barrel and ϕ/θ for the endcap.
The KLM exploits the high penetration power of muons to distinguish them from hadrons. For hadrons, the KLM and ECL combined provide 4.7 interaction lengths of material, which efficiently dissipates their energy through hadronic showers. Electrons have short

radiation length in iron (1.7 cm) and are usually absorbed by the electromagnetic calorimeter. K_L^0 mesons produce clusters in both ECL and KLM. These clusters are grouped and geometrically matched with charged tracks found in the inner tracking detectors. Clusters without an accompanying charged track are then taken as K_L^0 candidates.
The KLM expected relative momentum resolution is $\sigma_p/p = 18\%$ for 1 GeV/c K_L with angular resolution of $\Delta\phi = \Delta\theta = 10$ mrad.

3.6 Trigger and data acquisition

The Belle II online event selection system (trigger) enables data acquisition from the whole detector for interesting events, based on partial information it receives from an appropriate set of sub-detectors. The trigger is organized hierarchically. Each sub-trigger system sends the trigger information associated with the corresponding sub-detector to a central trigger logic, the global decision logic (GDL) [1], which decides whether the event should be recorded or not.

The SuperKEKB bunch crossings occur almost continuously, every second or third period of the machine radio-frequency at about 408 MHz. The total cross sections and trigger rates at the goal luminosity of 8×10^{35} cm^{-2}s^{-1} for several processes of interest are listed in Figure 3.11. Bhabha and $\gamma\gamma$ events are used to measure the luminosity and to calibrate the detector responses. Since their cross sections are dominant, the corresponding triggers are prescaled by a factor of 100 or more. Prescaling means accepting only a predetermined fraction of events that meet the trigger requirements. After a beam collision, the GDL

Physics process	Cross section (nb)	Rate (Hz)
$\Upsilon(4S) \to B\bar{B}$	1.2	960
Hadron production from continuum	2.8	2200
$\mu^+\mu^-$	0.8	640
$\tau^+\tau^-$	0.8	640
Bhabha ($\theta_{\rm lab} \geq 17°$)	44	350 [a]
$\gamma\gamma$ ($\theta_{\rm lab} \geq 17°$)	2.4	19 [a]
2γ processes ($\theta_{\rm lab} \geq 17°$, $p_t \geq 0.1$ GeV/c)	~ 80	~ 15000
Total	~ 130	~ 20000

[a] rate is pre-scaled by a factor of 1/100

Figure 3.11: Total cross section and trigger rates with $L = 8 \times 10^{35}$ cm^{-2}s^{-1} from various physics processes at the $\Upsilon(4S)$.

-

makes a decision in 4.5 μs and, if the decision is to accept, then the readout starts. Since the GDL is the first system to make the decision and is dead time free, it is also called

Level 1 trigger. It receives all sub-trigger information, makes logical calculations and then issues the Level 1 trigger on appropriate timing.

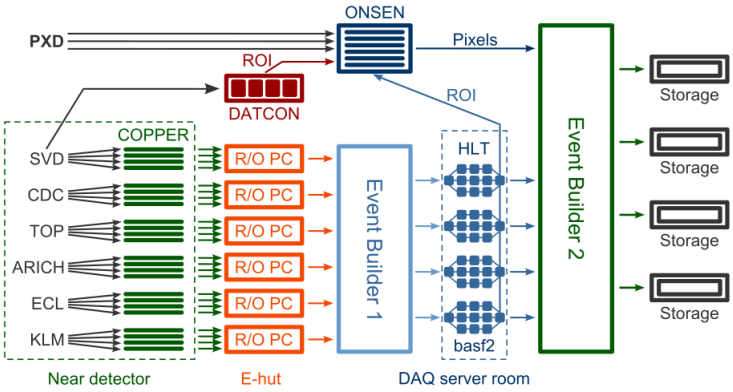

Figure 3.12: Schematic overview of the Belle II DAQ. About 300 COPPER boards take the data and transfer it to about 30 R/O PCs. The data are then merged in the event builder and the events are reconstructed by the HLT, which consists of $O(10)$ units with about 400 cores per unit. The reconstructed data are merged with the PXD data and stored in about 10 storage units.

As soon as the Level 1 trigger sends the signal for reading out the Belle II detector, the data acquisition system (DAQ) [1] takes over. It reads the data from the various sub-detectors, and processes and writes them to the storage system. Exception for the PXD, all sub-detectors are read out through a unified data link system, the Belle2Link. An important part of the Belle2Link is the COPPER board, an electronic board inherited from Belle, which converts the data format of each individual sub-detector into a common data format. The output of each COPPER board is sent to the event builder, which merges the data that belong to the same collision into an event. Then the full event reconstruction follows. This is accomplished with the help of the high level trigger (HLT) [1], a computing farm running the Belle II analysis software framework (BASF2), the same used for physics analyses. Information coming from fully reconstructed events allows the HLT to make the final decision and choose whether an event has to be recorded or discarded. If it is recorded, the associated PXD data are merged with existing data in a second event builder.
As soon as the PXD receives a trigger signal, readout starts. The data are read into the online selector nodes that store the PXD data for up to 5 s, which is the maximum latency of the HLT. The HLT, in the meantime, performs event reconstruction. The charged tracks reconstructed in the HLT, based on the information from the SVD and CDC, are then propagated back to the PXD sensors to define regions of interest (ROI). Only the PXD pixels contained within a ROI are kept and sent to the second event builder. In addition

to the HLT, another system, the data concentrator, searches for ROIs. Those systems work complementarily. The concentrator is optimized for low momentum particles, while the HLT targets high-momentum particles. In order for both systems to work, a charged particle has to produce hits in all SVD layers.
Various trigger selections are possible. Trigger for physics are typically based on the presence of 2-3 tracks in the event, or a large energy deposition in the calorimeter, or a high multiplicity of isolated electromagnetic clusters, or a combination of these. Bhabha events are vetoed.

3.7 Offline processing and simulation

The Belle II data processing software BASF2 [38] is a consistent software framework designed to handle off-line processing and analysis tasks. Most of the code is written in C++ and Python scripts are used for framework execution. Events are processed by a sequence of modules specified in the Python steering file written by the user. BASF2 is linked to external libraries like ROOT [39] which enables storing of common data for events processing, Geant4 [40] for full detector simulation and alignment libraries like Millepede II [41].

Off-line reconstruction takes into account that the detector is composed by a set of subdetectors of various geometries, dimensions and materials immersed in a magnetic field, and exploits information on the interactions of particles with matter to reconstruct the particles trajectories and the signals they induce in the detectors, using algorithms that model particle propagation.
A detailed overview of the off-line track reconstruction algorithms, which are specifically pertinent to this thesis work, is given in the next chapter.

EvtGen [42] is the main Belle II Monte Carlo generator for B and D physics events. Belle II has developed its own version of EvtGen, where source code is written in C++ and the latest C++ version of Pythia [43] is used.
EvtGen implements many detailed dynamical models that are relevant for the physics of B mesons. One of the central ideas subtending EvtGen is that decay amplitudes, instead of probabilities, are used. New decays can be added as modules. The amplitude for each node in the decay tree is used, thus including all angular correlations. In total, there are approximately 70 models implemented to simulate a large variety of physics processes.

In this work I also used KKMC [44]. This event generator was designed for precision SM predictions of the processes $e^+e^- \to f\bar{f},\ f = \mu, \tau, d, u, s, c, b$ at the center of mass energies from τ-lepton threshold up to 1 TeV. Photon emission from initial beams and outgoing fermions are included up to the second QED order, including all interference ef-

fects. Electroweak corrections are included at first order and final-state quarks hadronize according to the parton shower model, which describes cascades of radiation produced from QCD processes and interactions. The main improvements with respect to previous generators for fermion final states are the inclusion of the initial-final state QED interference and the inclusion of the exact matrix element for two photons.

Eventually, I also used BabaYagaNLO [45] [46], which is targeted at QED processes at flavor factories for center-of-mass energies of 1-10 GeV. The goal was to reach an accurate prediction of the cross section of QED processes, in particular for Bhabha scattering, by inclusion of radiative corrections (by means of the parton shower model) and of photon radiation effects. BabaYagaNLO is able to generate $e^+e^- \to e^+e^-(n\gamma)$, $e^+e^- \to \mu^+\mu^-(n\gamma)$, $e^+e^- \to \gamma\gamma(n\gamma)$ and $e^+e^- \to \pi^+\pi^-(n\gamma)$ events, using the following cross section:

$$\sigma(s) = \int dx_1 dx_2 dy_1 dy_2 \int d\Omega D(x_1, Q^2) D(x_2, Q^2) \times$$
$$\times D(y_1, Q^2) D(y_2, Q^2) \frac{d\sigma_0(x_1, x_2, s)}{d\Omega}, \tag{3.1}$$

where the Born-like cross section for the process $d\sigma_0/d\Omega$ is convoluted with the QED non-singlet structure functions $D(x, Q^2)$, which are the solutions of the Altarelli-Parisi equation [47] in QED that account for photon radiation emitted by both initial-state and final-state fermions.
Once particles of each event are generated, their interactions with the detector are simulated, taking into account the various materials and geometries, and energy losses in the sensitive volumes are stored. This is realized using Geant4, which simulates the passage of particles through matter using Monte Carlo methods. After this procedure, hits associated to the event are created, together with trajectories and secondary particles. The hits are are saved in hits collections. Simulated data are then analyzed using the reconstruction modules of each detector component. This simulated information will be used as truth information in the analysis.

3.8 Schedule

SuperKEKB/BelleII is a major improvement of the old KEKB/Belle experiment which operated from 1999 to 2010. On June 30 2010 KEKB was shut down, in order to be updated toward SuperKEKB. The commissioning of SuperKEKB and Belle II consists of three phases:

- *Phase 1 (October 2015 to December 2016).* The beam pipe was cleaned without the detector, by circulating a beam current of 0.5-1 A.

- *Phase 2 (March 2018 - July 2018).* Belle II was installed, but with just a small azimuthal portion of the vertex detector. This phase is currently ongoing and is focused essentially on background studies for the detector, in order to ensure that background levels associated with the much higher machine luminosity expected for physics data taking are compatible with the operation of the vertex detector. In addition, hardware controls are tested. The target is to reach the design luminosity of KEKB (10^{34} cm^{-2} s^{-1}) with stored beams of 1000/800 mA.

- *Phase 3 (since February 2019).* This is the phase when the physics data taking will start for the detector complete with its VXD and the luminosity will be ramped up gradually to the design value of 8×10^{35} cm^{-2} s^{-1}.

Chapter 4

Charged particle tracking

In this chapter my original work is introduced. The chapter deals with the reconstruction of charged particles trajectories (tracks), and includes a description of the algorithm for off-line event reconstruction, an introduction to track parametrization in Belle II and details on the treatment of Coulomb multiple scattering using the general-broken-lines algorithm and examples from simulated events. We end the chapter with the description of the default track based alignment procedure.

4.1 Track reconstruction

In general, track reconstruction proceeds through three steps:

1. **Hit clustering:** in which hits in tracking detectors are selected and merged to remove noise hits and obtain a more precise estimate of the space-point where the particle traversed the detector.

2. **Pattern recognition:** in which dedicated algorithms identify the radial sequences of hit-clusters more likely to correspond to real trajectories, taking into account the constraints due to the production topology (e.g., trajectories originating in the collision point) and the detector geometry.

3. **Track fitting:** in which the final, precise estimation of track parameters is achieved with a fit of the hit-cluster positions after pruning clusters not belonging to identified patterns.

Belle II adopts GENFIT2 [48], illustrated in Figure 4.1, to perform track reconstruction. GENFIT2 consists of three main tools. Clustering is performed by *Hit reconstruction*, which deals with different dimensionalities of measurements (e.g., 1 for silicon strips, 2 for pixels) and for CDC hits constructs virtual planes where the measurement is expressed, as shown in Figure 4.2.

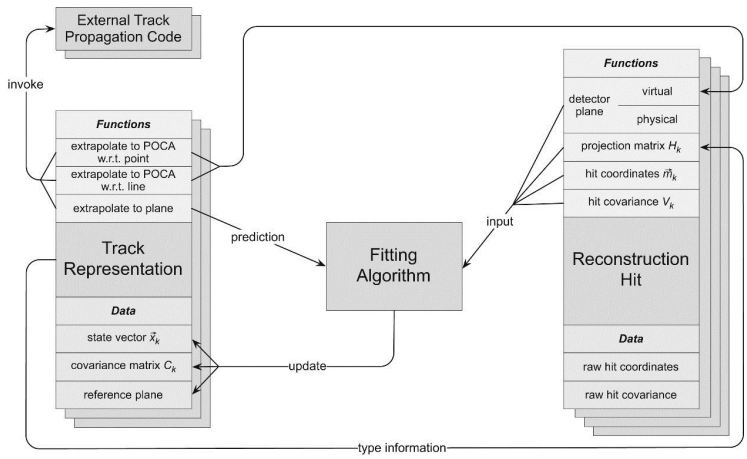

Figure 4.1: Procedure of hit reconstruction and track fitting.

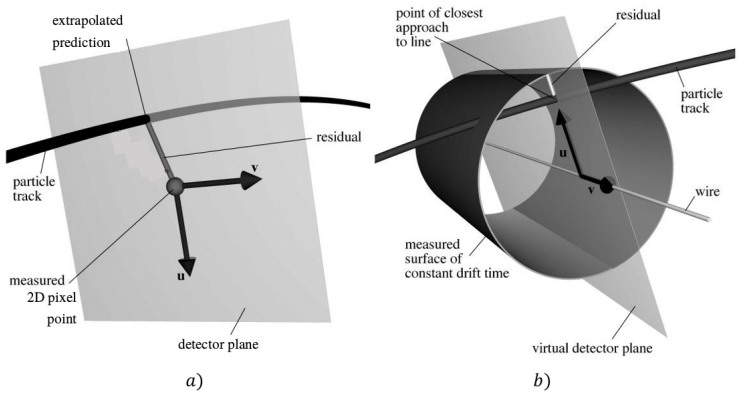

Figure 4.2: a) Track passing through a pixel sensor. b) Construction of virtual plane for wire hit.

Usually for a charged particle traversing a sensor, multiple pixels/strips record a signal and the single pixel or strip outputs are combined into clusters that are then identified as hits. The *Hit reconstruction* tool provides a single hit position estimation and an uncertainty that accounts for the shape and charge distribution in the cluster.
Pattern recognition is performed by *Track representation*, which performs particle propagation and extrapolation taking into account the detector geometry and the magnetic field. It combines the track parametrization and extrapolation functionalities. This tool holds the information about the state vector, representing the trajectory at a given plane, and the covariance matrix corresponding to a hit measurement. It also provides functions to extrapolate the track parameters to different positions in the detector volume along with the estimated trajectory.

The third tool is *Track fitting* which, given the reconstructed hits and a track representation (a set of parameters describing the track), fits the track using either the Kalman filter or the deterministic annealing filter and updates the state vector and covariance of track parameters.
Given the relevance that track-fitting has for my work, I discuss track-fitting in greater detail. It is useful to introduce the coordinate system relevant for the reconstruction algorithms.

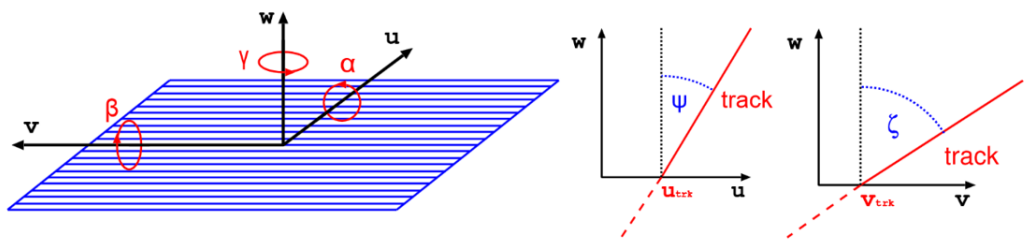

Figure 4.3: Local coordinate system (u, v, w) and Euler rotation angles (α, β, γ) on the left. Definition of the track slopes $u' = tan\psi$ and $v' = tan\xi$ in the local system, on the right

The VXD sensors are treated as planar rigid bodies and a local coordinate system (u, v, w) is defined for each, as shown in Figure 4.3. The origin of the system is set at the center of the sensor, w is the local coordinate orthogonal to its surface, and u and v are parallel to the short and the long side of the sensor, respectively. A track can be expressed locally by means of the following state vector $(q/p, u, v, du/dw, dv/dw)$ where q is the charge of the particle and p its momentum.

The Kalman filter [49] is the basic algorithm for most track fitting used in high energy physics. It is a least-squares stepwise parameter-estimation technique originaly proposed by R.E. Kalman to provide signal filtering in electrical engineering. A schematic description of the algorithm is in Figure 4.4.

Let us consider a track model $\vec{f}$ and the state vector of the particle trajectory at a given point in space $\vec{x} = (x, y, dx/dz, dy/dz, q/p)$, expressed in laboratory's global coordinates, where q/p is the charge-momentum ratio. The aim of the Kalman filter is to infer the state vector at location k based on its value at the previous location $k-1$,

$$\vec{x}_k = \vec{f}_k(\vec{x}_{k-1}) + \vec{w}_k, \tag{4.1}$$

where $\vec{w}_k$ is a noise vector with zero mean. The Kalman filter implies a linearization of the system in the vicinity of $\vec{x}_{k-1}$ to obtain

$$\vec{f}_k(\vec{x}_{k-1}) = F_k \cdot \vec{x}_{k-1}, \tag{4.2}$$

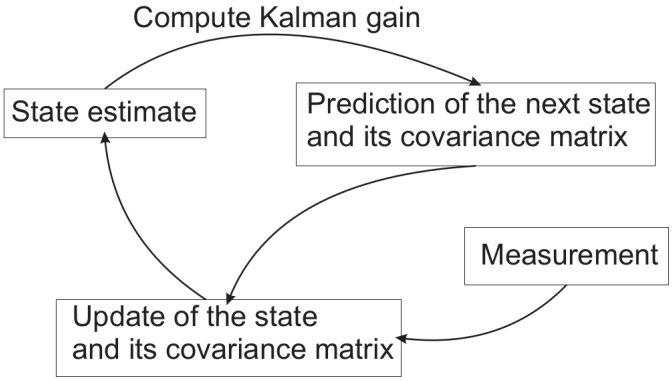

Figure 4.4: Workflow of the Kalman filter.

$$h_k(\vec{x}_k) = H_k \cdot \vec{x}_k, \tag{4.3}$$

for the track model and the measurement equation, respectively. Kalman filter estimation therefore involves three essential functionalities:

- **Prediction**, which is the estimation of the state vector at a *future* step $k+1$ using all the measurements up to and including the previous measurement m_k.
- **Filtering**, which is the estimation of the *present* state vector based on all *present* and *past* measurements. For forward-filtering, this means estimating track parameters at iteration k using measurements up to and including m_k. For backward-filtering, this means estimating track parameters at k using the measurements from the last m_N down to m_k. **Filter** stands for the algorithm that performs filtering and is built incrementally. This means that filtering from m_1 to m_k consists in filtering m_1 to m_{k-1}, propagating the track from m_{k-1} to m_k and including m_k. A filter can proceed forward (when k increase) or backward (when k decreases).
- **Smoothing**, which means interpolating through all measurements to provide a track parameter estimate at any position. The smoothed estimate is a weighted mean of two filtered estimates: the first one using m_1 to m_k (forward) and the other using m_N to m_{k+1} (backward).

The basic idea is understood as follows: if an estimate of the state vector at the $k-1$ step is available, this is extrapolated to the k step by means of Eq. (4.4). The estimate at step k is then computed as a weighted mean of the predicted state vector and of the actual measurement at the step k, according to the measurement Eq. (4.6). The information contained in this estimate can be passed back to all previous estimates by means of a second filter running backwards or by the smoother.

The main relations for the resulting linear dynamic system are the following:

- **System equation:**

$$\vec{x}_k = F_k \cdot \vec{x}_{k-1} + \vec{w}_k; \tag{4.4}$$

$$E[\vec{w}_k] = 0, \quad cov[\vec{w}_k] = Q_k \quad (1 \leq k \leq N). \tag{4.5}$$

- **Measurement equation:**

$$m_k = H_k \cdot \vec{x}_k + \epsilon_k; \tag{4.6}$$

$$E[\epsilon_k] = 0, \quad cov[\epsilon_k] = V_k = G_k^{-1} \quad (1 \leq k \leq N). \tag{4.7}$$

where ϵ_k is the measurement error, and the matrices Q_k and V_k represent the process noise (multiple scattering, bremsstrahlung, etc.) and measurement noise (detector resolution) respectively.
In the special case of a charged particle traveling in a solenoidal magnetic field, the trajectory is described by five parameters. The information on the measurement errors is stored in a five dimensional covariance matrix V. The information available after the Kalman fitting are

- $\vec{x}_k^F$ and $\vec{x}_K^B$: the forward and backward estimates of the state vector at k. The estimate of the track parameters are therefore available at the k-th step using measurements 1 up to k (forward) and N down to k (backward).
- $\chi_k^{2(F)}$ and $\chi_k^{2(B)}$: the minimum χ^2 value of the forward and backward fit up to measurement k.
- $V_F^{(\vec{x}_k)}$ and $V_B^{(\vec{x}_k)}$: the covariance matrices of $\vec{x}_k^F$ and $\vec{x}_k^B$ respectively.
- $\vec{x}_k$, χ_{trk}^2 and $V^{(\vec{x}_k)}$: the same quantities, determined from the smoothed estimates, the equivalent of a full fit at k.

As shown in Figure 4.5, the procedure yields, at every hit, the results of three fits for the track parameters at that hit: a fit to the upstream track segment, a fit to the downstream track segment and a fit of the whole track.

4.1.1 Including noise

The deterministic annealing filter (DAF) [50] is mainly used when ambiguous measurements, heavily affected by noise, are present. In such cases the Kalman filter is suboptimal because it requires the hit-assignment problem to be solved by previously performed track finding and wrongly assigned noise hits would lead to biased fit results. The DAF is based on a Kalman filter with an additional re-weighting of the observed measurements. The

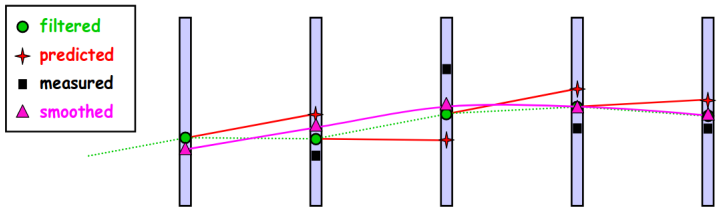

Figure 4.5: Schematic representation of a track fit performed by means of the Kalman filter. At every measurement plane, information on the measured hit (black), the predicted hit (red), the filtered hit (green) and the smoothed hit (magenta) are available.

DAF determines assignment probabilities for all competing hits. This way, outlier hits that are marginally compatible with the track parameters are down-weighted. The filter is applied by performing several iterations. If a hit probability falls below a certain threshold, that hit is not used in the next iteration. The threshold is decreased progressively and the total number of iterations is optimized depending on the noise and the quality of the starting values.

4.1.2 Including multiple scattering

Charged particles interact with the detector material losing energy by ionization or radiation, which reduces their momentum. In addition, tracks are affected by multiple Coulomb scattering, which produces changes in direction.
Multiple scattering effects are treated by the general broken lines (GBL) algorithm [51], which is integrated in GENFIT2. It performs the propagation from a measurement plane or scatterer to the previous and next scatterer using a locally linearized track model. For the Belle II vertex detector, only scattering from the detector planes is considered.

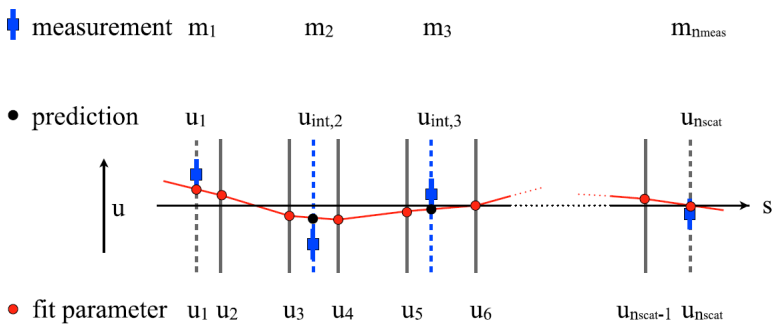

Figure 4.6: Schematic description of the GBL method. The material between measurement i and $i+1$ is described by means of two thin scatterers. The fit prediction $u_{int.,i}$ for the measurement m_i is obtained by interpolation between the enclosing scatterers.

At each thin scatterer, a two-dimensional offset $\vec{u} = (u, v)$ in the local frame is defined as a fit parameter. In case of small corrections to the track parameters $(\Delta q/p, \Delta\vec{u}', \delta\vec{u})$, they propagate as

$$\Delta\vec{u}_{i+1} = \frac{\partial\vec{u}_{i+1}}{\partial\vec{u}_i}\Delta\vec{u}_i + \frac{\partial\vec{u}_{i+1}}{\partial\vec{u}'_i}\Delta\vec{u}'_i + \frac{\partial\vec{u}_{i+1}}{\partial q/p}\Delta q/p. \tag{4.8}$$

In addition, in the case of three scattering planes, kinks (large slope differences between the linearized track before and after a scattering plane), resulting mainly from multiple Coulomb scattering between the charged particle and the atomic electrons, are taken into account.
The GBL algorithm fits the set of local parameters $\vec{x} = (\Delta q/p, \vec{u}_1, ..., \vec{u}_{Nscatt})$ and obtains the kinks and their uncertainties at scattering planes, by minimizing

$$\chi^2(\vec{x}) = \sum_{i=1}^{n_{meas.}} (H_{m,i}\vec{x} - \vec{m}_i)^T V_{m,i}^{-1} (H_{m,i}\vec{x} - \vec{m}_i) + \sum_{i=2}^{n_{scatt.}} (H_{k,i}\vec{x})^T V_{k,i}^{-1} (H_{k,i}\vec{x}), \tag{4.9}$$

where $V_{m,i}, V_{k,i}$ are respectively the variances of the measurements and kinks and $H_{m,i}, H_{k,i}$ are the matrices of the derivatives $\partial\vec{m}/\partial\vec{x}, \vec{k}/\partial\vec{x}$ of the measurements and related kinks, with respect to the fit parameters.

4.2 Tracks in Belle II

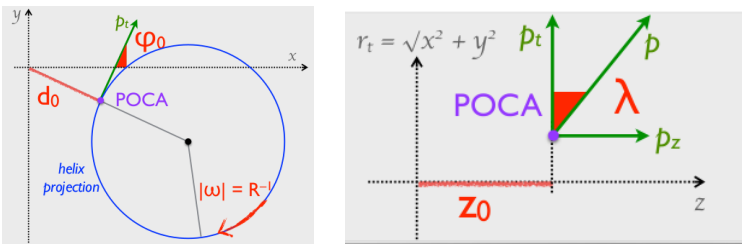

(a) Transverse parameters. (b) Longitudinal parameters.

Figure 4.7: Track parametrization at POCA.

A SuperKEKB collision is expected to generate eleven tracks, on average, in the Belle II detector. The trajectory of a charged particle moving into a magnetic field collinear with the beam axis is approximated by a helical shape. A convenient parametrization for physics analysis is to use the parameters referred to the perigee, or point of closest approach (POCA) to the z-axis, as shown in Figure 4.7. The advantage of this parametrization is that it uses five independent parameters, directly connected with the

physics quantities relevant for data analysis.

In what follows, I show the typical distributions for the global track parameters for a sample of simulated 5000 signal-only $e^+e^- \to \mu^+\mu^-$ events, reconstructed using GENFIT2, to provide a first qualitative feeling of the typical properties of the Belle II tracks.

4.2.1 Transverse impact parameter

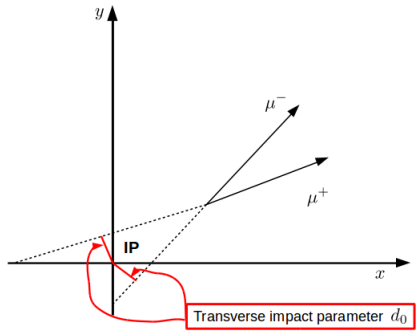

Figure 4.8: Illustrative sketch of impact parameter in a dimuon event.

The transverse impact parameter d_0 is the signed distance from the origin to the POCA, in the transverse plane (x, y). The sign of d_0 is such that $\vec{p}_T$, $\vec{d}_0$ and $\hat{z}$ form a right-handed system. The distribution of the reconstructed d_0 values, shown in Figure 4.9, is Gaussian as expected. The d_0 value depends on the spatial positions of track hits on the inner sensors of the VXD (Figure 4.8), which are mainly affected by multiple Coulomb scattering. Multiple scattering effects explain also the long tails of the distribution, produced by low-momentum muons suffering major scattering. The mean of the distribution is consistent with a production vertex in the e^+e^- interaction point, in the origin of the reference system, in contrast to the decays of long-lived particles, like B and D mesons, where higher mean-valued d_0 distributions are expected.
The standard deviation offers an estimate of the d_0 resolution and its value of $O(10)$ μm is consistent with the expected performance of the VXD.

4.2.2 Azimuthal angle

The azimuthal angle ϕ_0 is the angle between $\vec{p}_T$ and the x-axis at POCA.
Figure 4.10 shows the distribution of reconstructed ϕ_0 from the $e^+e^- \to \mu^+\mu^-$ sample. The distribution is uniform as expected.

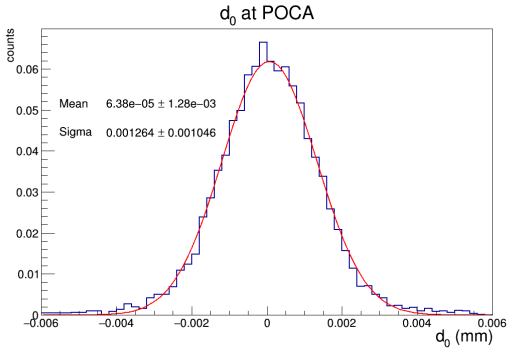

Figure 4.9: Distribution of reconstructed $d0$s at POCA. The solid red line correspond to a Gaussian fit and the estimated parameters are shown in the legend.

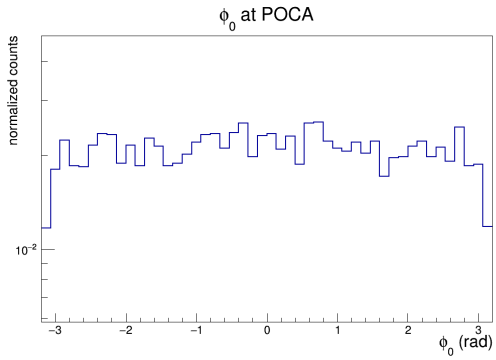

Figure 4.10: Normalized distribution of reconstructed ϕ_0 at POCA.

4.2.3 Curvature

The track's curvature at POCA is defined as $\omega = 1/2R$, where R is the radius of the circle corresponding to the projection of the helix on the (x, y) plane.
The distribution of reconstructed ω for μ^+ and μ^- is shown in Figure 4.11(a). This distribution is bimodal because the curvature is signed.

The distribution of p_T, which is closely related to the curvature, is shown in Figure 4.11(b). It peaks at approximately 5 GeV/c which, for a muon pair produced directly in the e^+e^- interaction, is linked to the collision energy of $\sqrt{s} = 10.58$ GeV. Muons with $p_T < 5$ GeV/c are those that decay in a plane different than the transverse plane.

4.2.4 Polar angle

The parameter $\tan\lambda$ is the ratio between the longitudinal momentum p_z and the transverse momentum p_T, at POCA, and carries information on the polar motion of the particle.
Figure 4.12(a) shows the distribution of reconstructed $\tan\lambda$ for our simulated muons. The

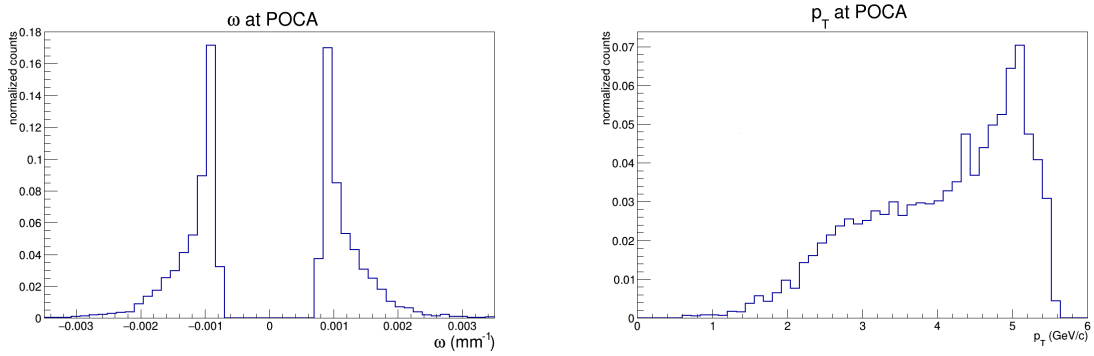

(a) Reconstructed ω (b) Reconstructed p_T

Figure 4.11: Normalized distributions of reconstructed ω (a) and p_T (b) at POCA.

distribution is asymmetric and has positive mean.
The distribution of reconstructed p_z in Figure 4.12(b) is asymmetric. The positive mean is expected from the SuperKEKB boost in the positive direction of the z-axis.

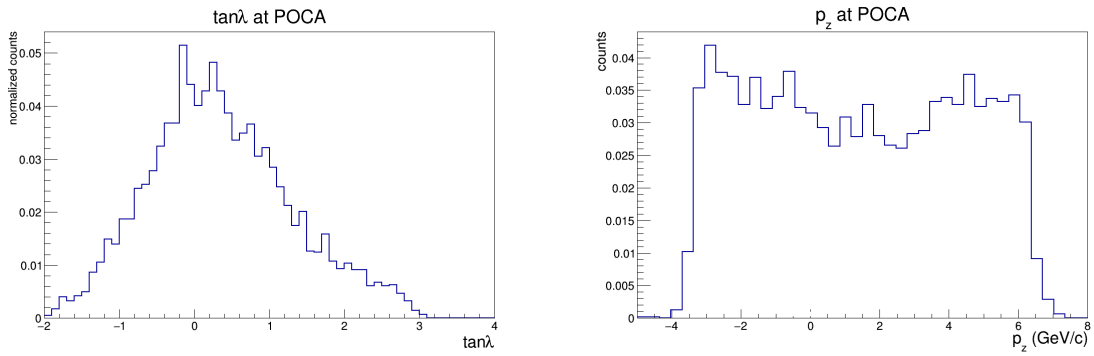

(a) Reconstructed ω (b) Reconstructed p_z

Figure 4.12: Normalized distributions of reconstructed tanλ (a) and p_z (b) at POCA.

4.2.5 Longitudinal impact parameter

The longitudinal impact parameter z_0 corresponds to the signed distance of the POCA from the transverse plane.
Figure 4.13 shows the distribution of reconstructed z_0 for our $e^+e^- \to \mu^+\mu^-$ sample. Its shape is Gaussian, with deviations from the mean value mainly caused by multiple scattering. No relevant contributions appear in the tails from low-momentum muons.
The value estimated by the fit for the standard deviation is a measure of the parameter resolution, which is approximately 16 μm, consistent with the expected $\sigma_{z_0} \approx 20$ μm.

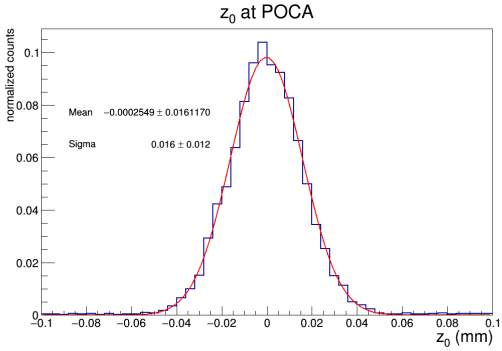

Figure 4.13: Distribution of reconstructed z_0 at POCA.

4.3 Standard VXD alignment

Silicon detectors are placed very close to the interaction point to reconstruct accurately decay vertices, by extrapolating inward tracks reconstructed using their hits. In order to correctly reconstruct tracks and vertices in space, it is necessary to know the actual positions of the vertex detector sensors. Silicon sensors are assembled and installed with tight tolerances around nominal positions, but small misalignments occur because of temperature variations, vibrations and other mechanical degrees of freedom. In addition, off-line alignment procedures are typically capable of achieving alignment precisions way superior of the mechanical tolerances respected during construction.
For small misalignments, as those expected in our case, an accurate way to estimate the real positions of VXD sensors is to use tracks reconstructed themselves by the VXD. The concept is that the known geometric and kinematic constraints associated with tracks of known origin (cosmic rays or collision products) are sufficient to infer statistically the misalignments of sensors and determine corrections for them.

4.3.1 VXD geometry

Because my work is related to the alignment of the vertex detectors, is convenient to introduce a parametrization of tracking detectors geometry.

A measurement in the local (i.e., referred to the specific position of the active detector layer in the tracking volume) reference system $\vec{u}_l$ can be expressed by using global coordinates, which are those defining the global Belle II reference system, by means of the following transformation

$$\bar{u}_g = R^T \vec{u}_l + \vec{r}_0, \tag{4.10}$$

where R is a rotation matrix and $\vec{r}_0$ is the position of the center of the measuring

sensor in the global reference system.
A correction to the rotation matrix ΔR and one corresponding to a local shift $\Delta\vec{q} = (\Delta u, \Delta v, \Delta w)$ result in a new global measurement

$$\vec{u}'_g = R^T \delta R(\vec{u}_l + \Delta\vec{q}) + \vec{r}_0. \tag{4.11}$$

The rotation is parametrized by Euler angles and is performed around the sensor's center so that no shift of the origin is induced by the rotation.
The alignment of each sensor is parametrized using six alignment parameters, three rotations and three translations, which allow to define the following alignment vector:

$$\vec{a} = (\Delta u, \Delta v, \Delta w, \Delta\alpha, \Delta\beta, \Delta\gamma)^T. \tag{4.12}$$

Then, for small corrections and neglecting higher-order contributions, the local measurement is expressed in terms of the alignment parameters as

$$\vec{u}'_l = \begin{pmatrix} 1 & \Delta\gamma & \Delta\beta \\ -\Delta\gamma & 1 & \Delta\alpha \\ -\Delta\beta & -\Delta\alpha & 1 \end{pmatrix} \begin{pmatrix} u \\ v \\ w \end{pmatrix} + \begin{pmatrix} \Delta u \\ \Delta v \\ \Delta w \end{pmatrix}. \tag{4.13}$$

4.3.2 Alignment

The alignment task is to find corrections that map the actual positions and orientations of sensors back to the nominal ones, so that the tracking reconstruction code offers optimal performance.
The track-based procedure to estimate these parameters consists in taking a large set of tracks of different types (curved tracks from collisions measured in presence of the magnetic field, straight tracks from collisions recorded when the magnetic field is off, cosmic-ray tracks not originated in the interaction point) and to constrain them to certain linear combinations of parameters, in order to use the degrees of freedom that remain after track fits to estimate alignment parameters.
Using measured hits and measurement uncertainties, the normalized tracking residuals are

$$z_{ij} = \frac{u^m_{ij} - u^p_{ij}(\vec{\tau}_j, \vec{a})}{\sigma_{ij}} = \frac{r_{ij}(\vec{\tau}_j, \vec{a})}{\sigma_{ij}}, \tag{4.14}$$

where u^m_{ij} is the measured u position of hit i on track j, u^p_{ij} is the predicted u position based on the track parameters $\vec{\tau}_j$ and the alignment parameters $\vec{a}$, and σ_{ij} is the uncertainty of the measurement.
The optimal track and alignment parameters are found by minimizing the following χ^2:

$$\chi^2(\vec{\tau},\vec{a}) = \sum_j^{tracks}\sum_i^{hits} z_{ij}^2(\vec{\tau}_j,\vec{a}). \tag{4.15}$$

Because of the large number of parameters, the minimization is a high dimensional problem. A special algorithm, Millepede II [41], has therefore been developed to deal with these χ^2 minimizations with constraints, Millepede II.

The first step in Millepede II consists in the linearization of the normalized residuals z_{ij}, so that the χ^2 can be written as

$$\chi^2(\vec{\tau},\vec{a}) = \sum_j^{tracks}\sum_i^{hits} z_{ij}^2(\vec{\tau}_j,\vec{a}) \simeq \sum_j^{tracks}\sum_i^{hits} \frac{1}{\sigma_{ij}^2}\left(r_{ij}(\vec{\tau}_j^0,\vec{a}^0) + \frac{\partial r_{ij}}{\partial \vec{a}}\delta\vec{a} + \frac{\partial r_{ij}}{\partial \vec{\tau}_j}\delta\vec{\tau}_j\right)^2, \tag{4.16}$$

where $\vec{\tau}_j^0$, $\vec{a}^0$ are the initial values of the track and alignment parameters, while $\delta\vec{\tau}_j$ and $\delta\vec{a}$ are small corrections. Track parameters are specific for each track and are called local parameters. Alignment parameters are common to the whole set of tracks and are therefore called global parameters.

The Millepede II minimization of $\chi^2(\vec{\tau},\vec{a})$ becomes equivalent to solving a system of linear equations:

$$\begin{pmatrix} \sum C_j & \cdots & G_j & \cdots \\ \vdots & \ddots & 0 & 0 \\ G_j^T & 0 & \Gamma_j & 0 \\ \vdots & 0 & 0 & \ddots \end{pmatrix} \begin{pmatrix} \vec{a} \\ \vdots \\ \delta\vec{\tau}_j \\ \vdots \end{pmatrix} = \begin{pmatrix} \sum \vec{b}_j \\ \vdots \\ \vec{\beta}_j \\ \vdots \end{pmatrix}. \tag{4.17}$$

The sum runs over all fitted tracks. Three kinds of sub-matrices arise. The first kind of matrix depends only on derivatives with respect to global parameters

$$(C_j)_{kl} = \sum_i^{meas} \frac{1}{\sigma_{ij}^2}\left(\frac{\partial r_{ij}}{\partial \vec{a}_k}\right)\left(\frac{\partial r_{ij}}{\partial \vec{a}_l}\right); \tag{4.18}$$

the second combines local and global parameters

$$(G_j)_{kl} = \sum_i^{meas} \frac{1}{\sigma_{ij}^2}\left(\frac{\partial r_{ij}}{\partial \vec{a}_k}\right)\left(\frac{\partial r_{ij}}{\partial \vec{\tau}_{j,l}}\right); \tag{4.19}$$

and the third contains only derivatives with respect to the track parameters

$$(\Gamma_j)_{kl} = \sum_i^{meas} \frac{1}{\sigma_{ij}^2}\left(\frac{\partial r_{ij}}{\partial \vec{\tau}_{j,k}}\right)\left(\frac{\partial r_{ij}}{\partial \vec{\tau}_{j,l}}\right). \tag{4.20}$$

The vector on the right-hand-side of Eq.(4.17) contains a sum of residuals related to the global or local parameters multiplied by the corresponding global or local derivatives,

$$(\vec{b}_j)_k = \sum_i^{meas} \left(\frac{\partial r_{ij}}{\partial \vec{a}_k} \right) \frac{r_{ij}}{\sigma_{ij}^2}, \qquad (\vec{\beta}_j)_k = \sum_i^{meas} \left(\frac{\partial r_{ij}}{\partial \vec{\tau}_{j,k}} \right) \frac{r_{ij}}{\sigma_{ij}^2}. \tag{4.21}$$

We reduce the size of the matrix in Eq.(4.17) to that of matrix (4.18), which is proportional to the number of alignment parameters, using Schur decomposition for a system of equations, which leads to the following smaller system:

$$C'\vec{a} = \vec{b}', \tag{4.22}$$

where

$$C' = \sum_i C_i - \sum_i G_i \Gamma_i^{-1} G_i^T, \qquad \vec{b}' = \sum_i \vec{b}_i - \sum_i G_i (\Gamma_i^{-1} \beta_i). \tag{4.23}$$

The main aim of Millepede II is to reduce the system of equations in order to deal with Eq.(4.22). This way, the correction to track and alignment parameters are respectively

$$\delta\vec{\tau}_j = \Gamma_j^{-1} \vec{\beta}_j \qquad \delta\vec{a} = (C')^{-1} \vec{b}'. \tag{4.24}$$

In Millepede II, solutions can be subjected to linear constraints. These constraints can be used to remove global undefined degrees of freedom, which are represented by three rotations and three translations, and, in addition, to implement structural constraints, which correlate alignment parameters of structures and their sub-components. The algorithm takes into account these constraints by adding Lagrange multipliers.

The first goal of my thesis is to develop a procedure to identify misalignments that is complementary to Millepede II. A first objective is to define a quick and efficient procedure, that may be approximated if compared to the accuracy of Millepede II, but that can allow for a direct identification of macroscopic misalignments of the detector, without having to wait for Millepede II to converge.
A second important objective is to define an algorithm capable of identifying specific misalignment configuration to which Millepede II is not sensitive, in order to supplement its performance.

Chapter 5

Baseline checks against macroscopic misalignments

This chapter discusses my work based on comparing distributions of reconstructed parameters for μ^+ and μ^- to develop a fast and efficient procedure for early identification of major misalignments of the vertex detector.

5.1 Strategy

The default track-based alignment procedure based on Millepede II needs a large number of tracks to solve a high-dimensional problem. Hence, the successful alignment with Millepede II requires time to collect sufficient data and computation time to converge. However, it is often useful to have preliminary information on alignment available in a short time-scale after collecting the data, or even on-line.
The basic idea of this initial alignment study is to develop an approximated but efficient procedure to quickly detect possible misalignments of the vertex detector. We aim at identifying a set of fast checks, using reconstructed information, to be used both during an on-line data acquisition and in preliminary reconstruction.

I choose to use muon tracks from the $e^+e^- \to \mu^+\mu^-$ process. Muon pairs allow for relying on sufficiently large and easily reconstructed samples for tracking studies, even after relatively short time periods of data taking. Although less abundantly produced, muon pairs are chosen over e^+e^- pairs, because of their reduced radiation.
Since experimental Belle II collision data were not yet available when I started my thesis work, I produced a sample of 2×10^4 $e^+e^- \to \mu^+\mu^-(\gamma)$ signal-only events generated using KKMC. The $e^+e^- \to \mu^+\mu^-$ cross section, at the $\Upsilon(4S)$ center-of-mass energy, is $\sigma = 1.148$ nb, as shown in Figure 5.1. Assuming that the collider is working at the nominal instantaneous luminosity of 8×10^{35} cm^{-2} s^{-1}, we should collect such a sample in approximately

22 sec of data taking.
I simulated the interaction of the generated muons with all the Belle II sub-detectors in the Phase 3 geometry (spring 2019 onwards), in which the full VXD is installed. This process generates trajectories and simulated hits that are used as truth information. After simulation, I performed full reconstruction of the signal events, from which I obtain the reconstructed track parameters.

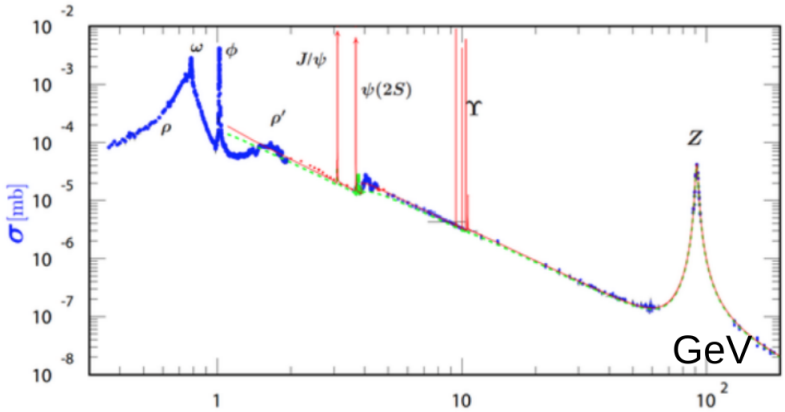

Figure 5.1: Cross section in [mb] for the process $e^+e^- \to \mu^+\mu^-$, as a function of the center of mass energy in GeV.

5.2 Preliminary checks

Prior to studying the details of reconstructed track parameters, I inspected a few distributions relevant for tracking, to ensure that the quality and understanding of my simulated sample is adequate. For these checks and in the following section 5.3, I used a smaller sample of 5000 $e^+e^- \to \mu^+\mu^-$ events.

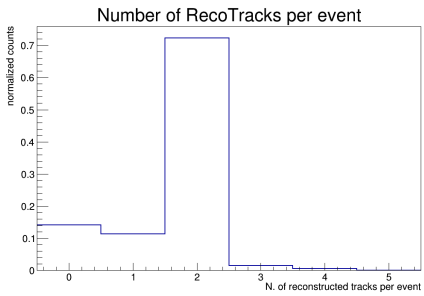

Figure 5.2: Distribution of the number of reconstructed tracks per event.

I studied the distribution of the number of reconstructed tracks for each $e^+e^- \to \mu^+\mu^-$

event, which is displayed in Figure 5.2. Approximately 72 % of the events are associated to two reconstructed tracks, which is consistent with a signal event. Events with less than two reconstructed tracks are explained by inefficiency of the reconstruction procedure, while those with more than two reconstructed tracks can be linked to a possible photon, produced together with the μ pair, that converts into electron-positron pairs in the detector.

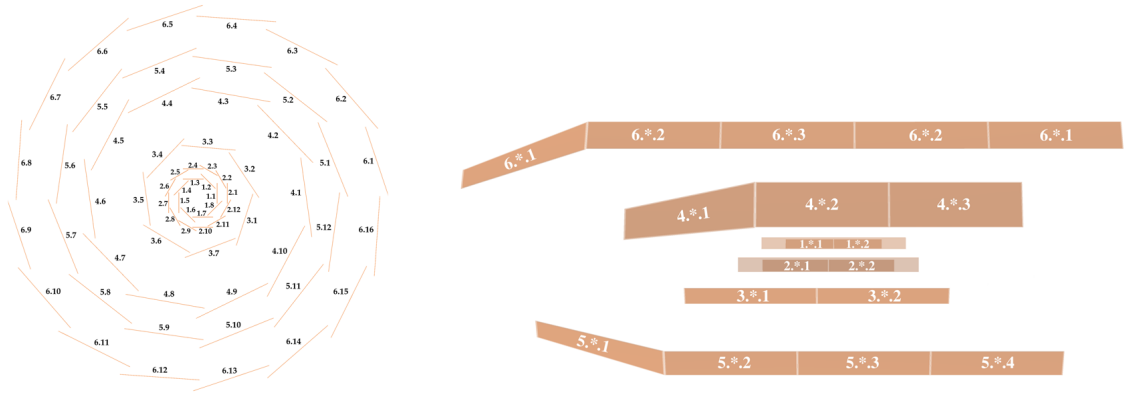

(a) Front view of the VXD: numbers of sensors are in the format Layer.Ladder. Layers 1, 2 belong to the PXD; layers 3, 4, 5, 6 to the SVD.

(b) Side view of the VXD: numbers of the sensors are in the format Layer.Ladder.Sensor (1.*.* and 2.*.* corresponding to PXD sensors, 3.*.*, 4.*.*, 5.*.*, 6.*.* to SVD sensors.)

Figure 5.3: Front (a) and side (b) views of the Belle II vertex detector.

Then I studied the distributions of the reconstructed PXD and SVD hits, after restricting to events where only two tracks are reconstructed. Figure 5.4 shows the number of PXD and SVD hits associated to a track. About 80 % of tracks excites two PXD hits, which is consistent with a muon traversing the two layers of the PXD.

Tracks with three PXD hits are linked to a muon passing through a sensor of the first layer and then through two overlapping sensors of the second layer or in the boundary of two pixels, which results in a (smaller) signal in both. The case of zero or only one hit correspond to tracks associated to e^+e^- pairs produced by a radiated photon outside of the PXD or between its two layers respectively, but can also be linked to detector and tracking algorithm inefficiencies.
The SVD is made of four layers of partially overlapping sensors, as shown in Figure 5.3(a), each capable of reading two position coordinates simultaneously. Approximately 75% of tracks have eight SVD hits, corresponding to a muon traversing a sensor per layer. Higher number of hits arise because of the narrow azimuthal regions hosting overlapping sensors, while the peak at six can be linked to a pair production after the first SVD layer and the peak at zero hits can be explained with a pair production outside the SVD. Pair-produced

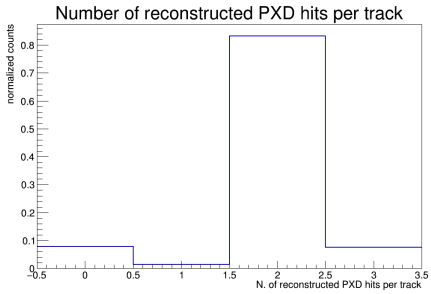

(a) Reconstructed PXD hits per track.

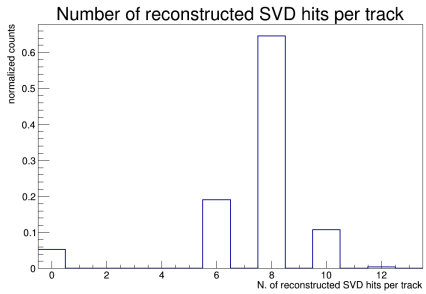

(b) Reconstructed SVD hits per track.

Figure 5.4: Distributions of the number of hits per track reconstructed in the PXD (a) and the SVD (b).

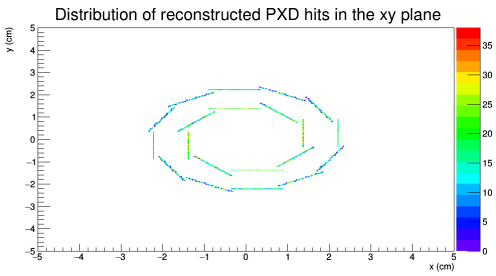

(a) Distribution of reconstructed PXD hits positions on the xy plane

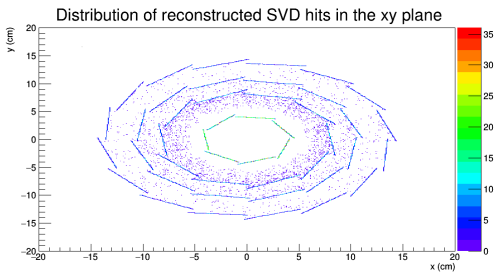

(b) Distribution of reconstructed SVD hits positions on the xy plane

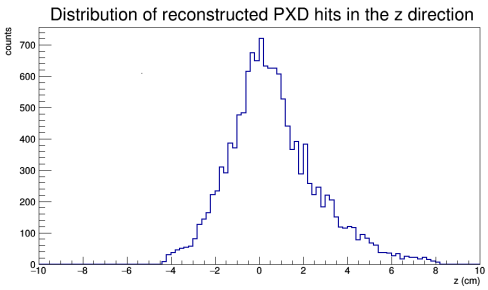

(c) Distribution of the z-coordinate for reconstructed PXD hits

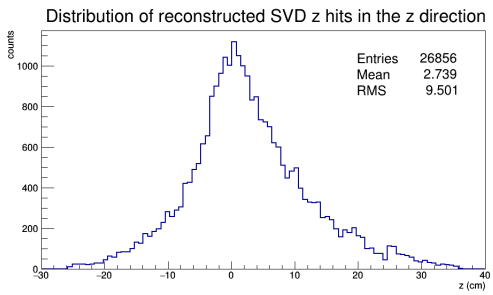

(d) Distribution of the z-coordinate for reconstructed SVD hits

Figure 5.5: Distributions of reconstructed PXD (a) and SVD (b) hits positions on the xy plane and of the z-coordinate for reconstructed PXD (c) and SVD (d) hits.

electron or positron tracks at these radii may come from rare cases of a photon radiated by a muon. Figure 5.5 shows the two-dimensional distributions of reconstructed hits on the xy plane and along the z direction. Comparison of these distributions with Figures 5.3 show that hits positions on the xy plane reproduce the two layers of the PXD and the four SVD layers, and hits detected by sensors in the forward end-cap of the SVD (layers 4, 5, 6) which are not orthogonal to the xy plane.
Plots (c) and (d) in Figure 5.5, show two asymmetric distributions with respect to zero, and with positive means, which are consistent with a boost in the positive z direction.

I also checked the alignment of the beam by looking at the two-dimensional distribution of d_0 versus ϕ_0, shown in Figure 5.6. In case of beams not coincident with the z axis this distribution would exhibit a sinusoidal shape, while a symmetric distribution is observed, showing no major signs of beam displacement.

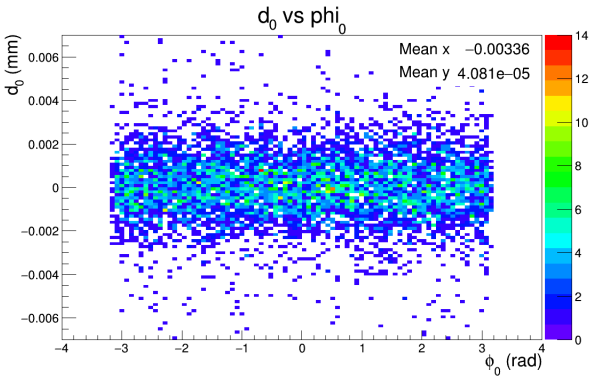

Figure 5.6: Two-dimensional distributions d_0 vs ϕ_0.

Once I ascertained that I understand adequately the properties of my sample I proceed to the misalignment study.

5.3 Event selection

Even if I generate signal-only events, the reconstructed information is affected by background that consists of possible electron pairs produced by the possible photon in the $e^+e^- \to \mu^+\mu^-(\gamma)$ process or radiated in the interaction of one of the muons with the detector. In order to suppress this background, I restrict only to those events where e^+e^- collisions produce two tracks reconstructed with opposite charge. In addition, I require that both tracks are geometrically extrapolated to sequences of hits in the KLM detector (Figure 5.7(a)) to further enrich my sample in pure muons. Figure 5.7(b), which is a two dimensional distribution of $\phi_0(\mu^+)$ (vertical axis) as a function of $\phi_0(\mu^-)$ (horizontal axis) for tracks subjected to the KLM selection, shows that most of the events lie along

two straight lines where $\Delta\phi_0 = \phi_0(\mu^+) - \phi_0(\mu^-)$ is approximately $+\pi$, when $\phi_0(\mu^-) \leq 0$ and $-\pi$ when $\phi_0(\mu^-) \geq 0$. However, there are still events scattered in the secant region corresponding to the peak around zero in Figure 5.7(a). Hence, I further require that the angle between muon momenta approaches π (back-to-back particles).

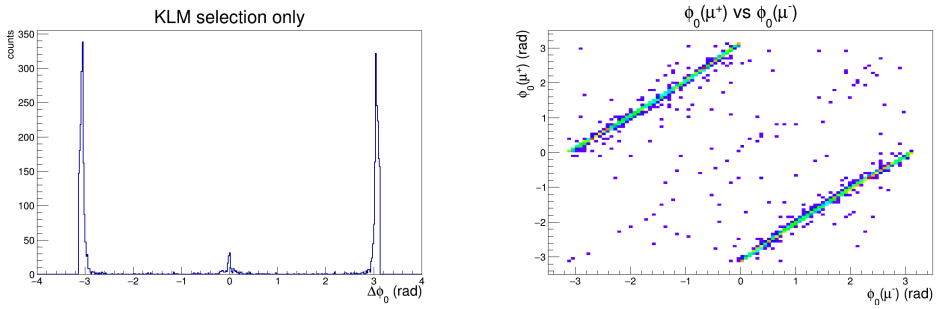

(a) $\Delta\phi_0$ distribution

(b) $\phi_0(\mu^+)$ vs $\phi_0(\mu^-)$ scatter plot.

Figure 5.7: $\Delta\phi_0$ distribution (a) and scatter plot of the azimuthal angles at POCA (b) for two reconstructed tracks having opposite charge and hits in the KLM.

These criteria slightly reduce the number of events in our data sample. We lose only 324 reconstructed tracks over 6580 with respect to the simpler selection of tracks with KLM hits, which itself reduced the original sample of 804 tracks out of 7384.
The combination of the KLM-hits condition and the back-to-back muons condition reduces the original track sample of about 15%. Inspection of relevant impact parameter distributions (Figure 5.8) shows that our simple selection criteria do not bias appreciably the features of the tracks.

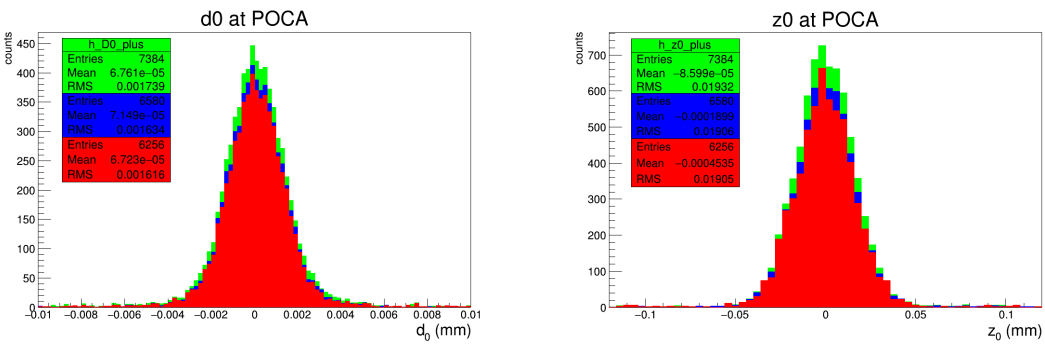

(a) d_0 distribution.

(b) z_0 distributions.

Figure 5.8: Distributions of reconstructed d_0 (a) and z_0 (b). Original sample (green), KLM-hits selection (blue) and KLM-hits + $|\Delta\phi| \simeq \pi$ selection (red).

5.4 Differences in charge-specific distributions

I now proceed to test the possibility of introducing a fast tool for early identification of VXD misalignments. For this study, I use a sample of 2×10^4 $e^+e^- \to \mu^+\mu^-$ events, subject to the selection previously illustrated.

In order to spot macroscopic misalignments, I exploit that charge-specific distributions of track parameters might be sensitive to particular misaligned configurations of the vertex detector, since track with opposite charge curve in opposite directions in the magnetic field. For each inspected variable, I study the difference between μ^- and μ^+ counts for each bin, by defining an asymmetry variable

$$A = \frac{n_i^{(-)} - n_i^{(+)}}{n_i^{(-)} + n_i^{(+)}}, \tag{5.1}$$

where $n_i^{(\pm)}$ is the number of $\mu^\pm$ counts in bin i of the relevant distribution. Figures 5.10 to 5.19 show the resulting asymmetries, with Poissonian errors on counts, fitted either by a constant model $y = p_0$ (left panel) or by a linear model $y = p_1 \cdot x + p_0$ (right panel).

5.4.1 Transverse impact parameter

Figure 5.10 shows shift between the two distributions. This suggests that there are more negative values for reconstructed d_0 in the case of μ^- and more positive values of the reconstructed d_0 if the track belongs to a positive muon. The sign of the parameter d_0 depends on the charge of the particle. Since for each $\mu^+\mu^-$ production vertex the reconstructed transverse impact parameters should have the same magnitude, but opposite signs, one would expect the two reconstructed distributions to be equivalent.
This shift towards the positive values for the d_0 distribution of the μ^+ may reflect a possible slope between the barrel part of the VXD and the beam axis.
I tested whether the count asymmetries for the reconstructed d_0 distributions of μ^- and μ^+ can be used as a fast-check to identify possible misalignments of the vertex detector. To do this I superpose asymmetries for the aligned configuration to those obtained for the three random VXD misalignments shown in Figure 5.9. These misalignments are obtained by displacing each sensor along the vector (du, dv, dw) with local displacements generated according to a normal distribution on a specific range and rotated of α, β and γ around the local axes, with angles of rotation uniformly generated on a selected range. The effects of these random misalignments on d_0 are shown in Figure 5.11, where I fitted data using a linear model. Figure 5.11 shows that d_0 count asymmetries are very sensitive to even moderate random misalignments, thus providing fast and efficient information to spot a misalignment of the VXD.

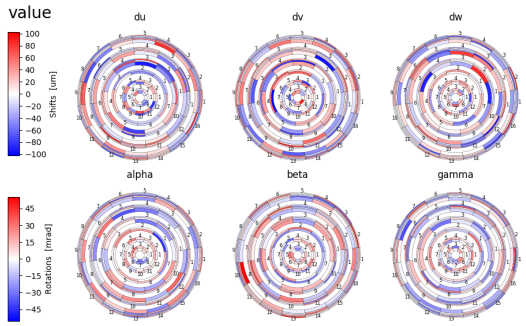

(a) Random VXD misalignment with local shifts in the range (-100,100) μm and local rotations in the range (-50,50) mrad.

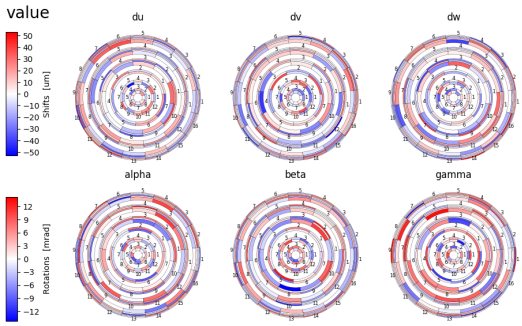

(b) Random VXD misalignment with local shifts in the range (-50,50) μm and local rotations in the range (-15,15) mrad.

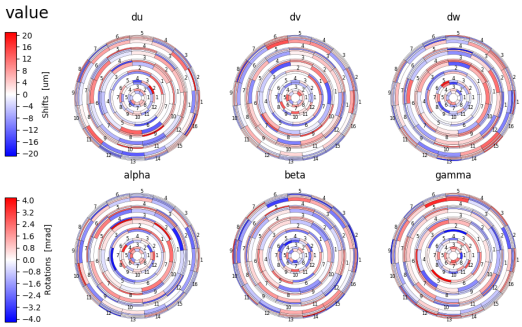

(c) Random VXD misalignment with local shifts in the range (-20,20) μm and local rotations in the range (-4,4) mrad.

Figure 5.9: Pictorial illustrations of random misalignments of the vertex detector. The color code on the left refers to the size of the sensor displacement. In the upper panels of (a), (b) and (c) du, dv, dw correspond to shifts for every sensor and in the lower panels alpha, beta and gamma refer to angles of rotation around the local axes.

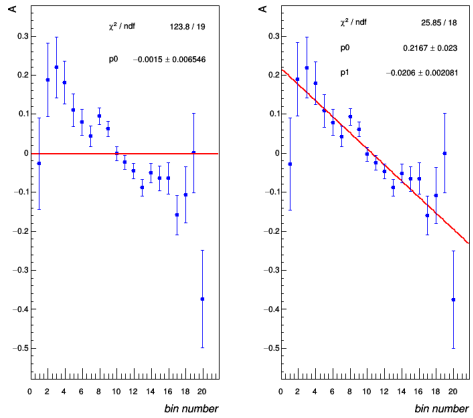

Figure 5.10: Track count asymmetries as functions of d_0, for aligned VXD. The data are fitted either by a constant model (left panel) or by a linear model (right panel).

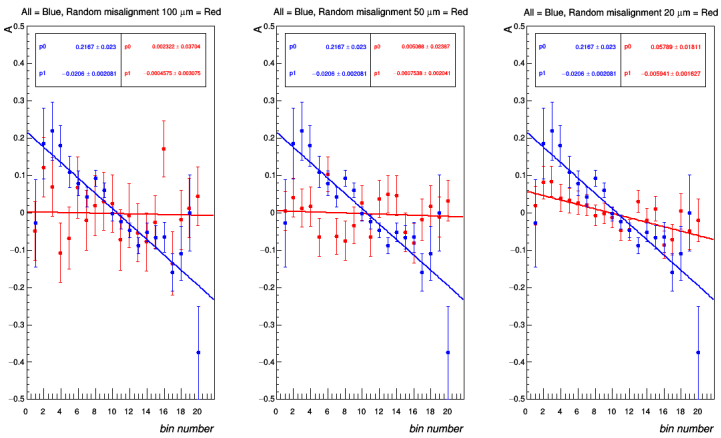

Figure 5.11: Track count asymmetries as functions of d_0 distributions, for aligned VXD (blue points) and for a random VXD misalignment (red points) of maximum 100 μm (left panel), 50 μm (central panel) and 20 μm (right panel).

5.4.2 Azimuthal angle

Figure 5.12 shows the track count asymmetries between charge-specific ϕ_0 distributions in an aligned VXD configuration. The points are fitted either by a constant model (left panel) or by a linear model (right panel), that show compatible results, which do not capture the pattern observed in data.

I tested the sensitivity of ϕ_0 count asymmetries to the random misalignments of Fig-

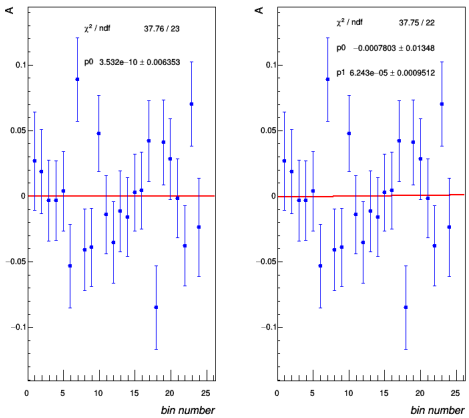

Figure 5.12: Track count asymmetries as functions of ϕ_0 distributions, for aligned VXD. The points are fitted either by a constant model (left panel) or by a linear model (right panel).

ure 5.9, by comparing points obtained in the aligned configuration to those resulting from a misalignment. Comparisons are shown in Figure 5.13 where blue points are related to the aligned VXD and red points to a random misalignment. Figure 5.13 shows that ϕ_0 asymmetries are not very informative, as expected, given the azimuthal isotropy of positive and negative tracks, even in the case of a relevant VXD random misalignment.

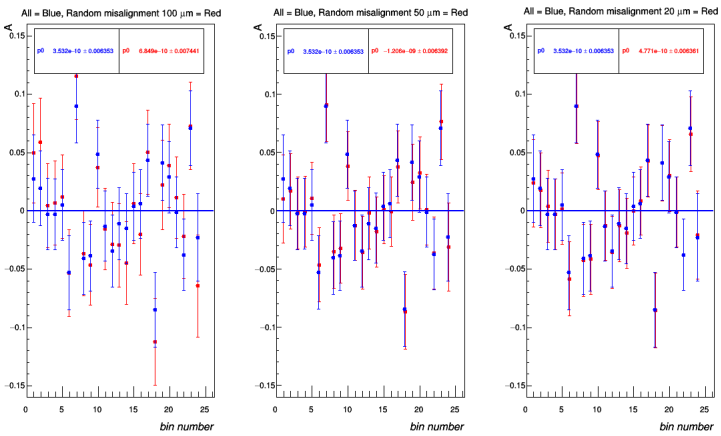

Figure 5.13: Track count asymmetries as functions of ϕ_0 distributions, for aligned VXD (blue points) and for a random VXD misalignment (red points) of maximum 100 μm (left panel), 50 μm (central panel) and 20 μm (right panel).

5.4.3 Curvature

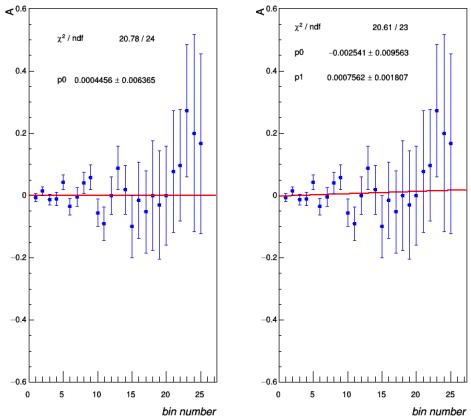

Figure 5.14: Track count asymmetries as functions of curvature magnitudes, in an aligned configuration. The data are fitted either by a constant model (left panel) or by a linear model (right panel).

Curvature has the same sign of the particle's charge, hence asymmetries in counts of Figure 5.14 are calculated using curvature magnitudes. The points are fitted either by a constant model (left panel) or by a linear model (right panel). Both the fits shown in Figure 5.14 describe adequately the data.

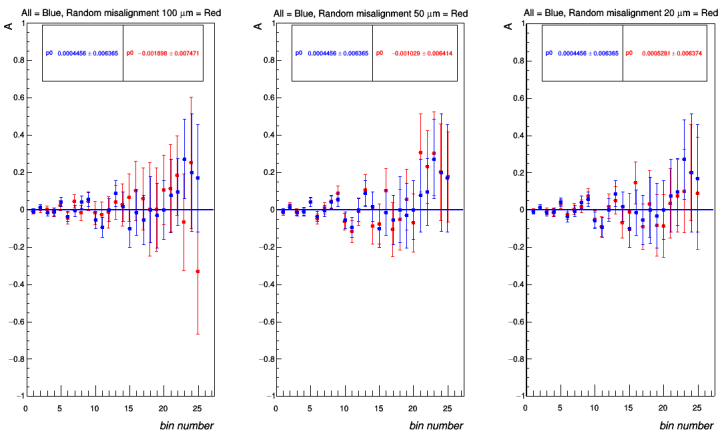

Figure 5.15: Track count asymmetries between μ^- and μ^+ as functions of $|\omega|$, for aligned VXD (blue points) and for a random VXD misalignment (red points) of maximum 100 μm (left panel), 50 μm (central panel) and 20 μm (right panel).

I tested the sensitivity of curvature asymmetries to the random VXD misalignments of Figure 5.9 by superimposing differences calculated for an aligned configuration to those resulting from a misalignment. In Figure 5.15, blue points are referred to the aligned configuration while red points to a VXD misalignment and they are both fitted using a constant model. The estimates of the parameter suggest that $|\omega|$ count asymmetries are poorly sensitive to random misalignments of the VXD.

5.4.4 tanλ

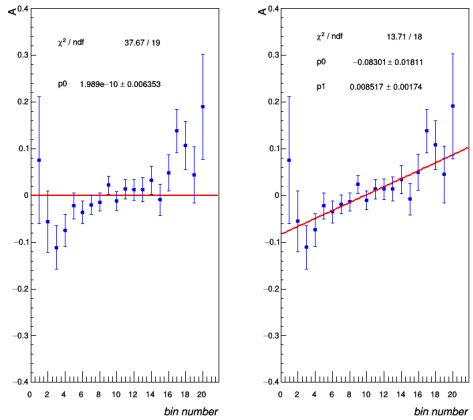

Figure 5.16: Track count asymmetries as functions of tanλ distributions. The data are fitted either by a constant model (left panel) or by a linear model (right panel).

Count asymmetries between μ^- and the μ^+ as functions of tanλ, obtained for the aligned VXD, are shown in Figure 5.16, where points have also been fitted using a constant and a linear model, which describes data better.
I tested whether the asymmetries between the reconstructed tanλ distributions of μ^- and μ^+ can be used as a fast check to identify possible misalignments of the vertex detector. I superpose count asymmetries for the aligned configuration to those obtained for the three VXD misalignments of Figure 5.9, as shown in Figure 5.17. Looking at the estimates of the linear model, I conclude that tanλ asymmetries are sensitive only to the largest misalignment, corresponding to displacements of sensors of 100 μm.

5.4.5 Longitudinal impact parameter

Data points in Figure 5.18 are the count asymmetries as functions of z_0, fitted either by a constant model (left panel) or by a linear model (right panel). The distributions are consistent, indicating a correct alignment for the sensors.

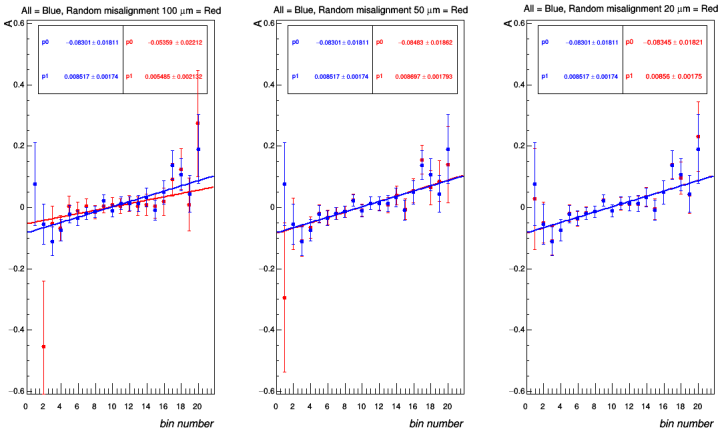

Figure 5.17: Track count asymmetries between μ^- and μ^+ as functions of tanλ, for aligned VXD (blue points) and for a random VXD misalignment (red points) of maximum 100 μm (left panel), 50 μm (central panel) and 20 μm (right panel).

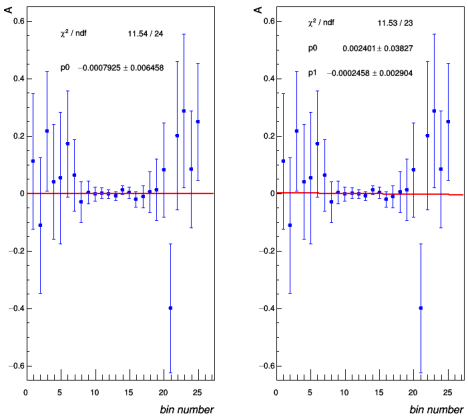

Figure 5.18: Count asymmetries as functions of z_0, obtained when the VXD is aligned. The points are fitted either by a constant model (left panel) or by a linear model (right panel).

I compare count asymmetries calculated for the distributions obtained in the aligned configuration to those resulting from the random VXD misalignments of Figure 5.9. Results are shown in Figure 5.19, where blue points refer to the aligned configuration and red points to one of the misalignments: z_0 asymmetries are only marginally sensitive to random VXD misalignments.

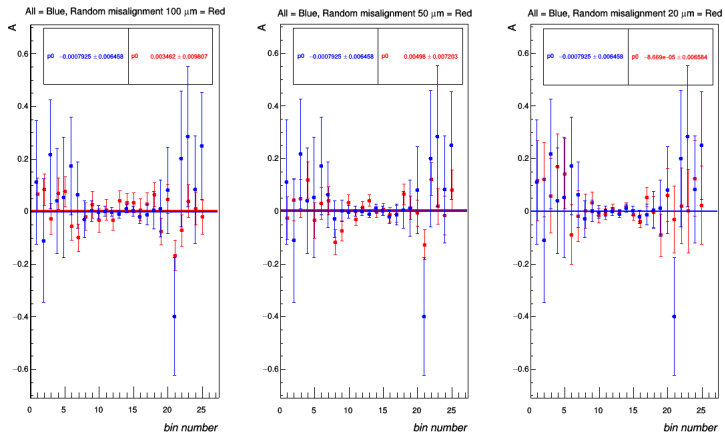

Figure 5.19: Track count asymmetries between μ^- and μ^+ as functions of z_0, for aligned VXD (blue points) and for a random VXD misalignment (red points) of maximum 100 μm (left panel), 50 μm (central panel) and 20 μm (right panel).

5.5 A novel variable: minimum track distance

Previous sections show that track count asymmetries as functions of track parameters might be sensitive to VXD misalignments, although it is not always straightforward to determine the nature and severity of the effect at play. In addition, it may be impractical to examine several different distributions while trying to detect quickly and efficiently VXD misalignments on-line. Therefore, in order to have a fast and reliable variable that summarizes most of the reconstructed track information, possibly amplifying the small effects observed, I construct a compact, higher-level variable consisting in the distance between the μ^- and μ^+ tracks. This variable is the shortest signed distance between the two straight lines, which approximate a pair of reconstructed tracks near the origin of the reference frame. In this approach, we neglect the curvature, which is justified for O(1) GeV/c muons travelling in the 1.5 T field over relevant radial distances of few centimeters.

In particular, if we consider the point of closest approach POCA of both tracks, we parametrize them as

$$\mu^+ : d_0^{(+)}\hat{t}^{(+)} + z_0^{(+)}\hat{z}_0 + \lambda^{(+)}\vec{p}_0^{(+)} \tag{5.2}$$

$$\mu^- : d_0^{(-)}\hat{t}^{(-)} + z_0^{(-)}\hat{z}_0 + \lambda^{(-)}\vec{p}_0^{(+)}. \tag{5.3}$$

As shown in Figure 5.20, d_0 and z_0 are the usual transverse and longitudinal impact parameters; $\hat{t}$ is the direction of d_0 and $\hat{z}$ that of z_0; λ is the angle formed by the particle's momentum at POCA with respect to the transverse plane (x, y); and $\vec{p}_0$ is the particle's

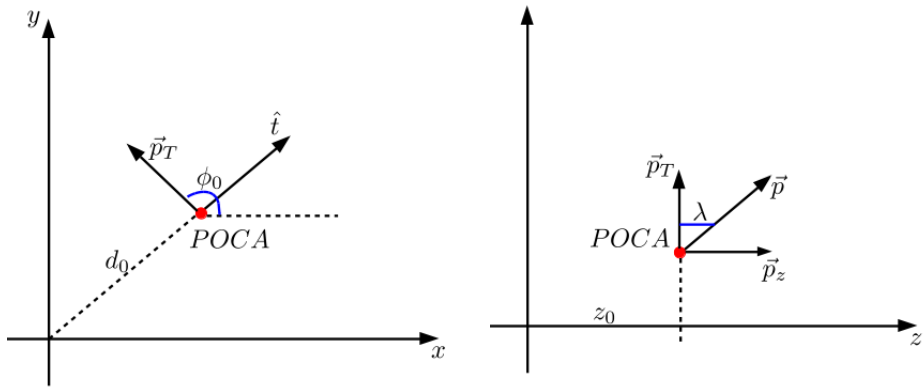

(a) Transverse view. (b) Longitudinal view.

Figure 5.20: Schematic description of a linearized track.

momentum at POCA, that can be written in terms of the transverse momentum p_T and of the azimuthal and polar angles, ϕ_0 and λ, as $\vec{p}_0 = (p_T \cos\phi_0,\ p_T \sin\phi_0,\ p_T \tan\lambda)$.

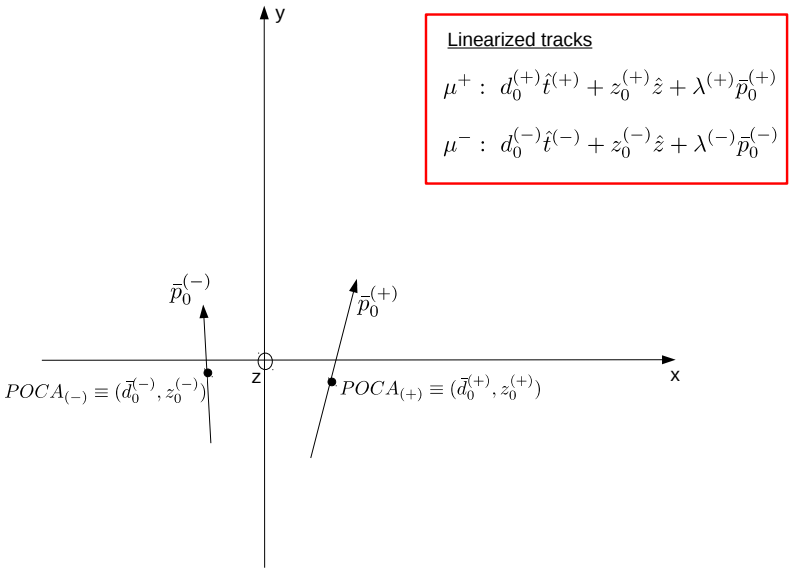

Figure 5.21: Linear approximation near the origin for two reconstructed charged tracks. The upper red box shows parameterizations for the two linearized tracks.

Figure 5.21 shows that one of the two lines passes through the point $\vec{P}_{(+)} \equiv POCA_{(+)}$ and is parallel to vector $\vec{p}_0^{(+)}$, which is the μ^+ momentum at POCA. The other through $\vec{P}_{(-)} \equiv POCA_{(-)}$ and is parallel to $\vec{p}_0^{(-)}$.

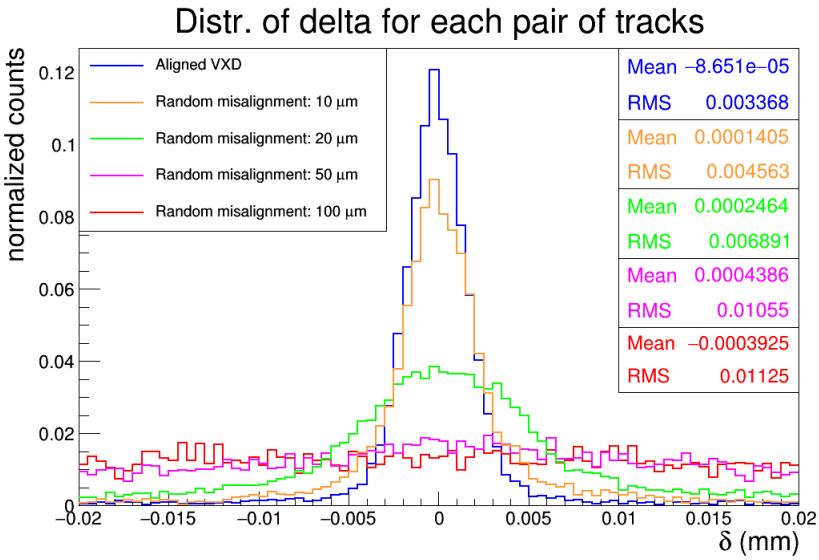

Figure 5.22: Distributions of δ distances for aligned VXD (blue), a random misalignment of the order of 10 μm (orange), 20 μm (green), 50 μm (magenta) and 100 μm (red). δ distances are calculated using Eq. (5.4), restricting to $e^+e^- \to \mu^+\mu^-$ events where only two tracks are reconstructed.

If these two lines intersect, then the minimum distance is trivially zero. In general, the two lines are not parallel and do not intersect. We build a vector $\vec{p}_0^{(+)} \times \vec{p}_0^{(-)}$ orthogonal to both lines. Then the projection of vector $\vec{P}_{(+)} - \vec{P}_{(-)}$ over $\vec{p}_0^{(+)} \times \vec{p}_0^{(-)}$ gives the minimum signed distance δ between the lines, defined by the following relation:

$$\delta = \frac{\vec{p}_0^{(+)} \times \vec{p}_0^{(-)}}{|\vec{p}_0^{(+)} \times \vec{p}_0^{(-)}|} \cdot \left(d_0^{(+)} \hat{t}^{(+)} - d_0^{(-)} \hat{t}^{(-)} + \left(z_0^{(+)} - z_0^{(-)} \right) \hat{z} \right) . \tag{5.4}$$

This distance was calculated for each of the simulated $e^+e^- \to \mu^+\mu^-$ events that meet the selection requirements, for an aligned VXD and in the case of three random misalignments of order 100 μm, 50 μm and 20 μm. The resulting distributions are shown in Figure 5.22. As expected, the blue distribution in Figure 5.22, corresponding to an aligned VXD configuration, is centered around zero, is symmetric and unimodal. On the other hand, Figure 5.22 shows that the δ distance is extremely sensitive to the random misalignments. When sensors are randomly displaced even of a small amount of 20 μm, which represents a realistic magnitude for shifts, the δ distribution keeps its symmetry but doubles its RMS. This widening is even larger for misalignments of 50 μm and 100 μm and it proves the δ distribution offers a useful, fast and efficient indicator to identify non-ideal alignments of the VXD in the reconstruction procedure.

The identification of such an easy to access variable that is supremely sensitive to tracker misalignments of even modest entity is a first important result of my thesis work.
The sensitivity of δ is used in Chapter 6 to spot specific misalignments of the vertex detector, that cannot be conclusively identified using χ^2 minimization procedures on measured tracks.

Chapter 6

Weak misalignment configurations

This chapter deals with the identification of those peculiar misalignments configurations that are poorly detected by the standard procedures. Such "weak modes" are residual misalignments arising from global, coherent displacements of sets of sensors that are marginally influent on the χ^2 minimization procedures.

6.1 Origin of weak modes

The best estimate of alignment parameters is found by solving the system of Eq. (4.22). This is only possible if the C' matrix can be inverted.
It may occur that the matrix is singular or nearly singular. This cases correspond to weakly defined degrees of freedom which poorly affect the χ^2. Weak modes are then related to eigenvectors of the C' matrix that have vanishing eigenvalues. These eigenvectors are linear combinations of alignment corrections, which result in coherent movements of individual VXD sensors that cannot be detected using the default alignment procedure.
This results in a significant contribution of weak modes to the systematic uncertainty of kinematic properties determined by the track fit and therefore on the quality of the physics.
The range of possible weak modes depends largely on the geometry and segmentation of the detector, on the topology and abundance of the tracks used for alignment, and on the alignment and track parameters. For a cylindrical detector in a solenoidal magnetic field like the Belle II VXD, and if the detector is aligned using tracks constrained to pass through the beam line, then the dominant weak modes are conveniently classified using cylindrical coordinates, i.e., by module displacements $\Delta r, \Delta z$ and $\Delta\phi$ as functions of r, z and ϕ.

An illustrative example of misreconstruction due to a weak mode is shown in Figure 6.2.

The described misalignment is a curl, which consists of an azimuthal rotation of sen-

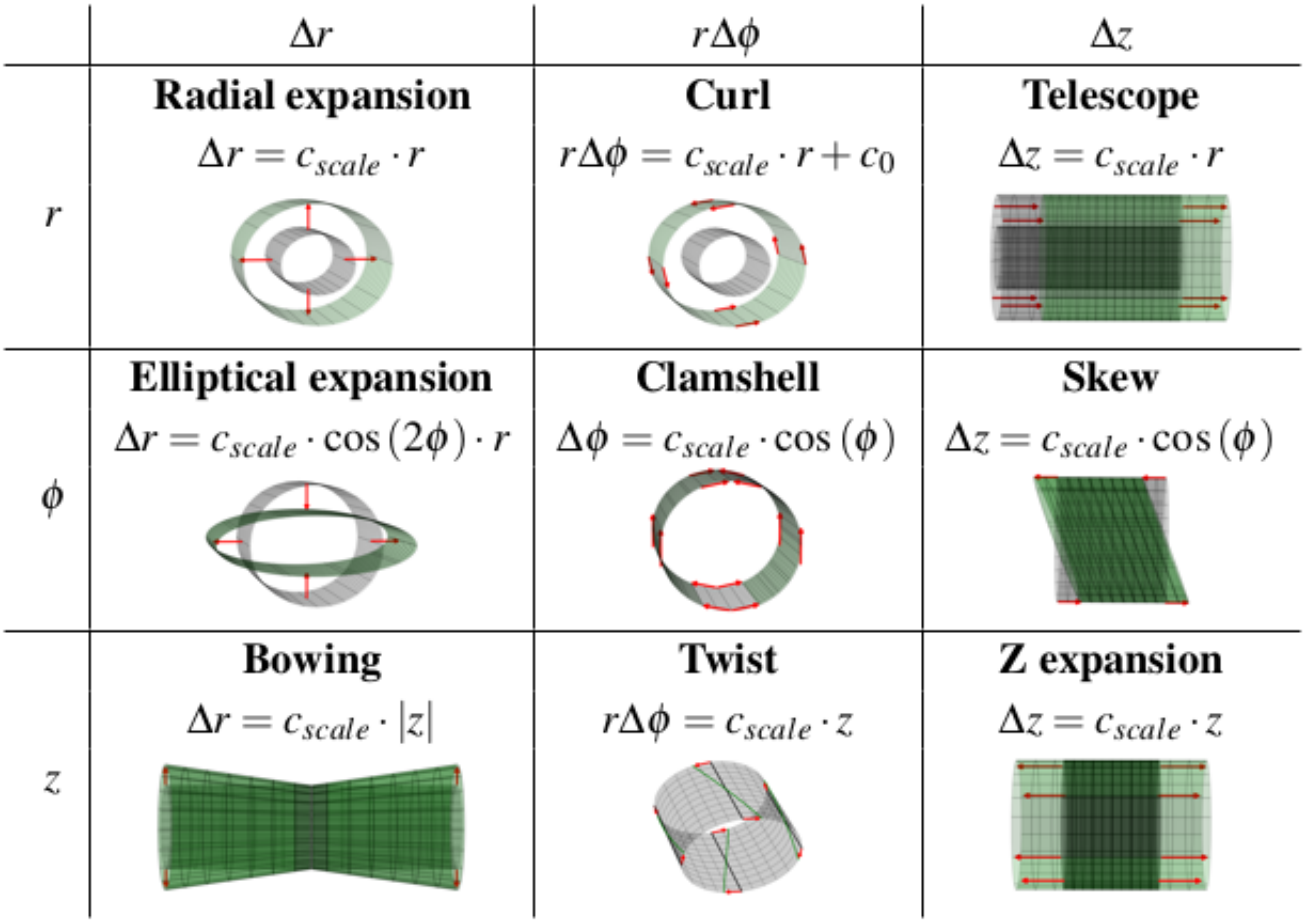

Figure 6.1: Sketch of the main weak modes of the Belle II vertex detector: coherent movements of individual sensors parametrized as displacements in global coordinates (columns) whose amplitudes depend on one of the global coordinates r, ϕ, z (rows).

sors. This results in reconstructing tracks using hits that are misplaced in the transverse plane for each z and obtaining wrong estimates for the track parameters defined on the transverse plane like d_0, ϕ_0 and ω.

In order to detect the presence of weak-mode misalignments using χ^2 minimization, it is necessary to include additional information in Eq. (4.15). In particular, combining track sets from various topological varieties and physics constraints, by means of cosmic ray tracks that break cylindrical symmetry; straight tracks without curvature, recorded when the magnetic field is off; information about the production vertices; or knowledge about the invariant mass of resonances whose decay products are observed as tracks.

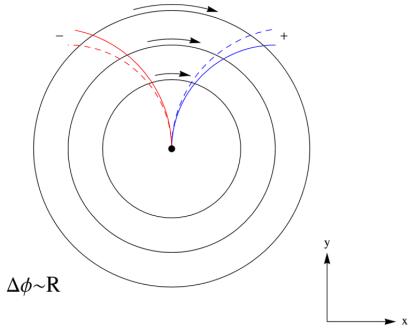

Figure 6.2: Curl deformation for a detector with cylindrical symmetry. Dashed lines correspond to the true trajectories of charged particles and solid lines show how they are reconstructed when the deformation occurs. The blue track correspond to the positively charged particle and the red to the negative particle.

This approach leads to a larger problem to be solved, because it adds complexity to the system of linear equations with extra rows and columns to the matrix that must be inverted.

The task is, then, to devise simpler dedicated and more effective procedures to detect weak modes. We aim at looking for distinctive patterns of reconstructed track parameters from easily available samples that can be linked to a specific weak mode, in order to enable a quick on-line identification.

6.2 Weak mode description and simulation

I started by simulating individually each of the misalignments of the vertex detector illustrated in Figure (6.1) using a dedicated python code. A three-dimensional deformation is defined as a class having an input parameter, which corresponds to a scale factor, and returning a spatial vector whose coordinates are the differences between the global coordinates of the new position of the sensor, induced by the deformation, and the original position. Every weak mode is implemented as another class where the characteristic relation between new and original coordinates is defined and calculated using the deformation class and the scale factor as input parameters.

An overview of the main weak-mode configurations follows:

- **Radial-expansion:** $\Delta r = c_{scale} \cdot r$.

  Every silicon sensor is shifted radially of a displacement Δr proportional to its

radius (Figure 6.3). This mode mostly affects the w local-coordinate which is orthogonal to the sensors surface.

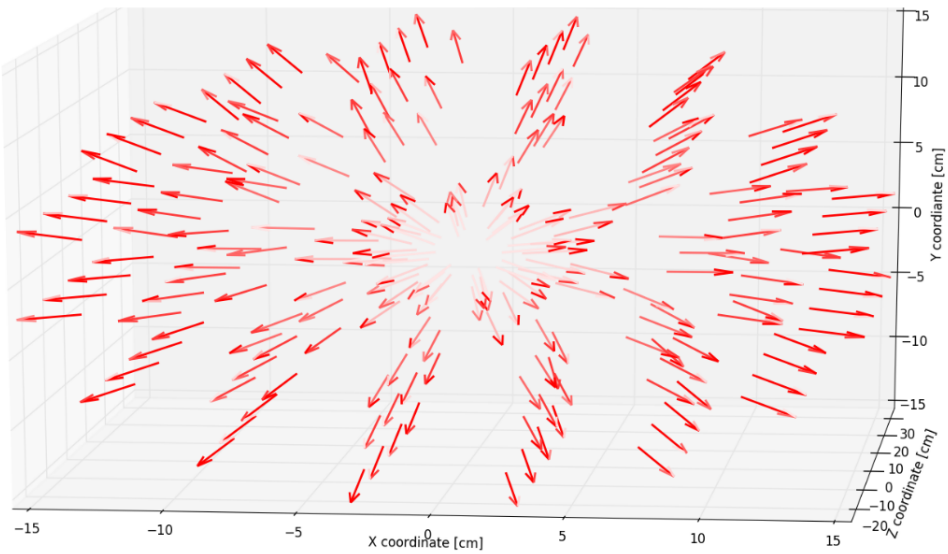

(a) Global coordinates.

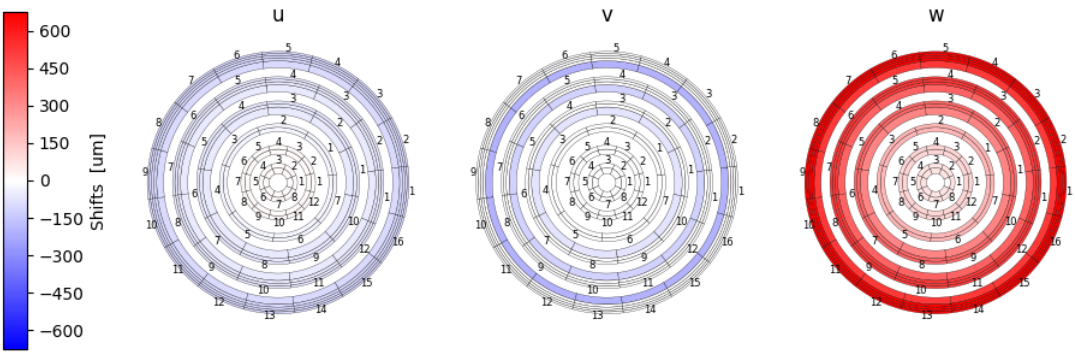

(b) Local coordinates.

Figure 6.3: Schematic description of VXD radial-expansion misalignment in the global coordinates system (a) and in the local coordinates system (b). The magnitude of the misalignment in the color bar is used for the analysis.

- **Curl:** $r\Delta\phi = c_{scale} \cdot r + c_0$.

  These are rotations of VXD sensors, where the magnitude of the shift on the transverse xy plane is proportional to the position r of the sensor (Figure 6.4). The local coordinate affected the most is u, which corresponds to the azimuthal direction.

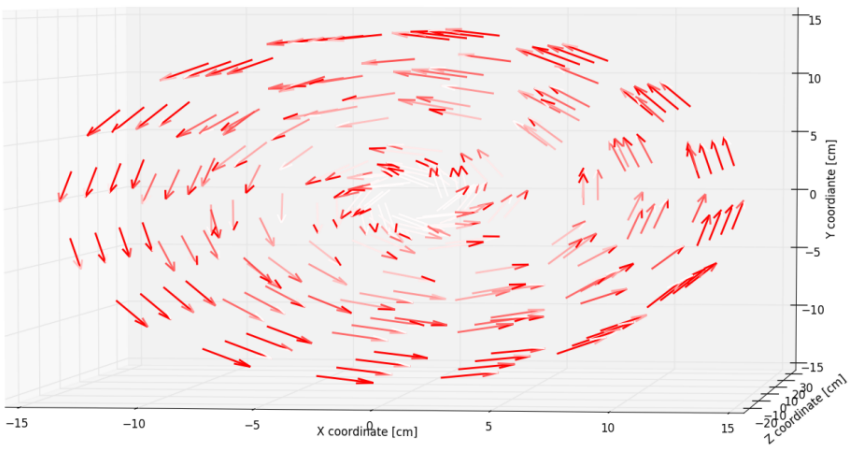

(a) Global coordinates.

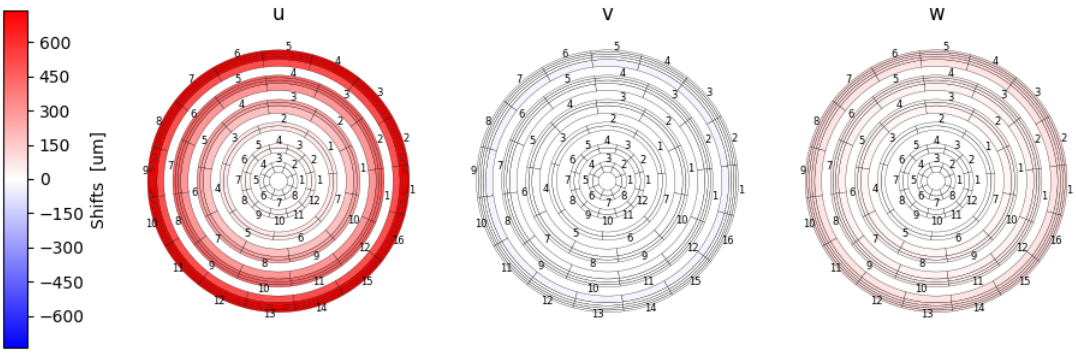

(b) Local coordinates.

Figure 6.4: Schematic description of the VXD curl misalignment in the global coordinates system (a) and in the local coordinates system (b). The magnitude of the misalignment in the color bar is used for the analysis.

- **Telescope:** $r\Delta z = c_{scale} \cdot r$.

  These are translations of sensors in the z-direction, where the magnitude of the shifts depends on the sensor's position r (Figure 6.5). This mode affects the v local-coordinate, which runs in the longitudinal direction.

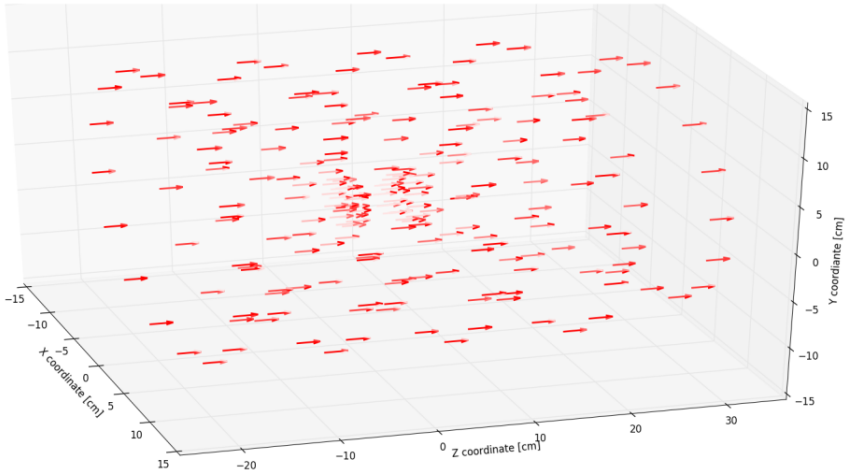

(a) Global coordinates.

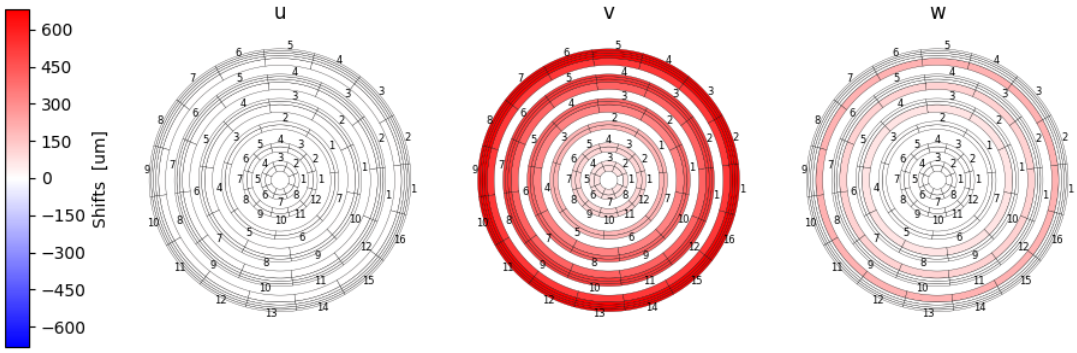

(b) Local coordinates.

Figure 6.5: Schematic description of the VXD telescope misalignment in the global coordinates system (a) and in the local coordinates system (b). The magnitude of the misalignment in the color bar is used for the analysis.

- **Elliptical-expansion:** $\Delta r = c_{scale} \cdot cos2\phi \cdot r$.

  Sensors of the VXD move tangentially to an ellipse on the transverse xy plane (Figure 6.6). Locally this mode affects mostly the w coordinate.

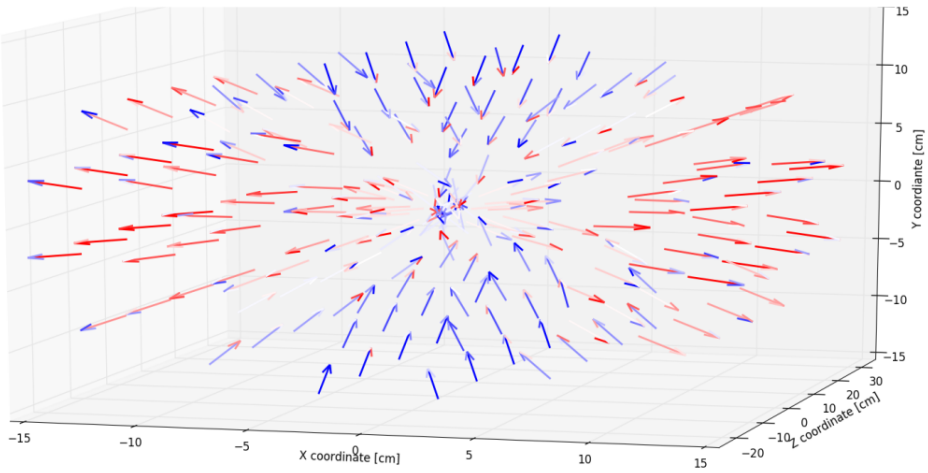

(a) Global coordinates.

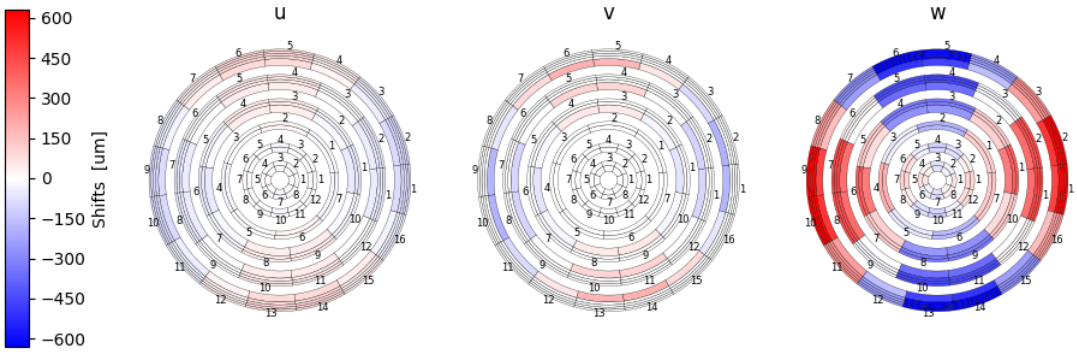

(b) Local coordinates.

Figure 6.6: Schematic description of the VXD elliptical-expansion misalignment in the global coordinates system (a) and in the local coordinates system (b). The magnitude of the misalignment in the color bar is used for the analysis.

- **Clamshell:** $\Delta\phi = c_{scale} \cdot cos\phi$.

  Sensors on one azimuthal half of the cylinder rotate in one direction while those on the other half rotate in the other (Figure 6.7). This misalignment produces a superposition of sensors in the junction interface between the halves and a depleted region on the complementary interface. It affects mostly the local u coordinate.

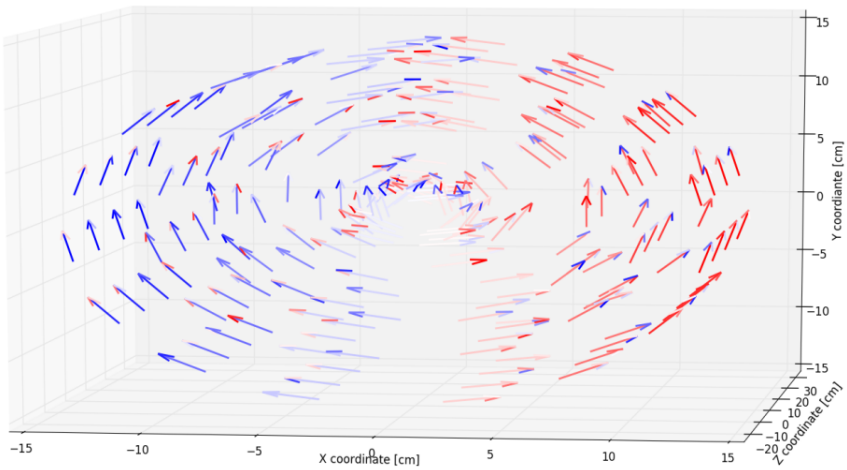

(a) Global coordinates.

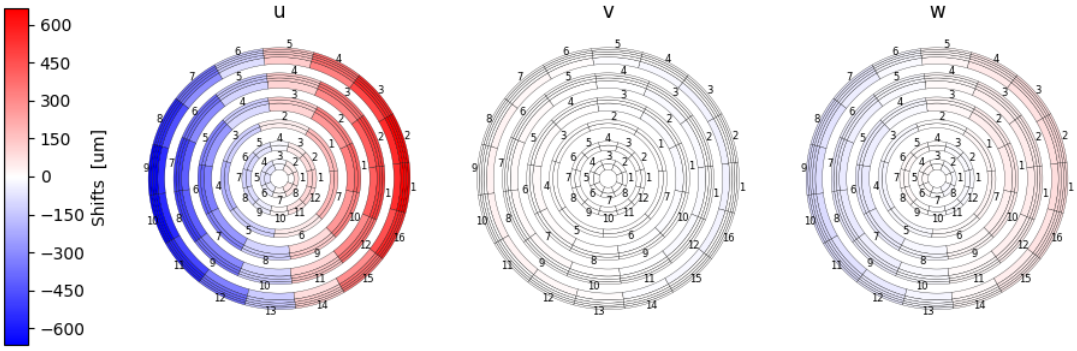

(b) Local coordinates.

Figure 6.7: Schematic description of the VXD clamshell misalignment in the global coordinates system (a) and in the local coordinates system (b). The magnitude of the misalignment in the color bar is used for the analysis.

- **Skew:** $\Delta z = c_{scale} \cdot cos\phi$.

  Sensors on one azimuthal half of the cylinder shift along a z-direction while those on the other half along the opposite z-direction (Figure 6.8). It affects mostly the local v coordinate.

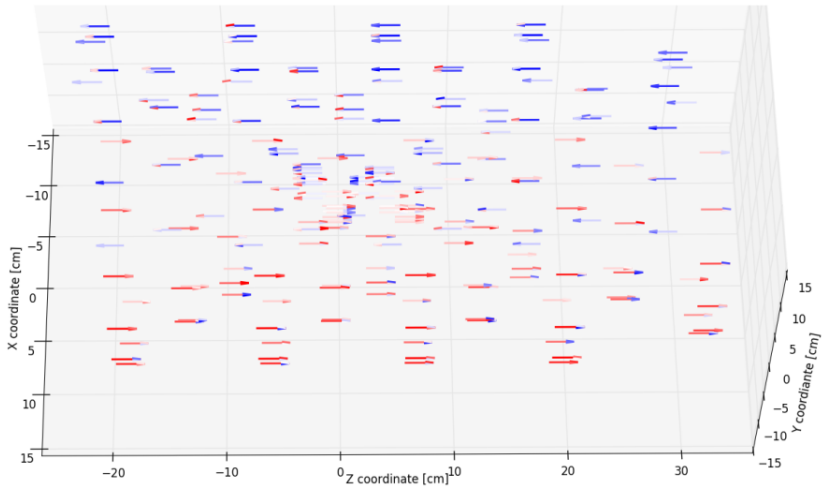

(a) Global coordinates.

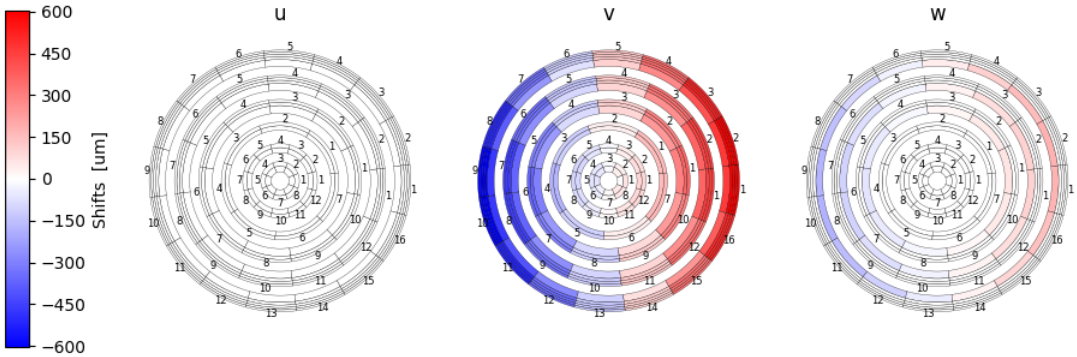

(b) Local coordinates.

Figure 6.8: Schematic description of the VXD skew misalignment in the global coordinates system (a) and in the local coordinates system (b). The magnitude of the misalignment in the color bar is used for the analysis.

- **Bowing:** $\Delta z = c_{scale} \cdot |z|$.

  Sensors on a $|z|$ = const. transverse plane shift radially with the magnitude directly proportional to $|z|$ (Figure 6.9). It affects mostly the local w coordinate.

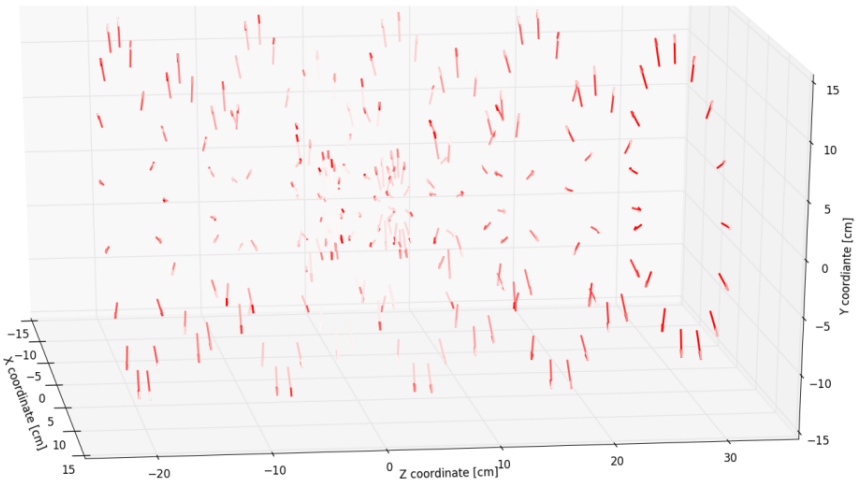

(a) Global coordinates.

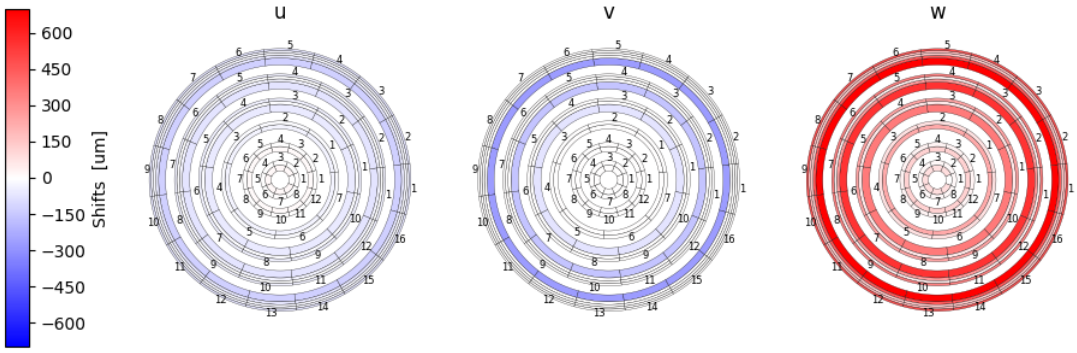

(b) Local coordinates.

Figure 6.9: Schematic description of the VXD bowing misalignment in the global coordinates system (a) and in the local coordinates system (b). The magnitude of the misalignment in the color bar is used for the analysis.

- **Twist:** $r\Delta\phi = c_{scale} \cdot z$.

  Sensors on one axial half of the detector rotate anti-clockwise on the transverse xy plane and move towards the negative z-direction (if they have negative x) and towards the positive z-direction (if they have positive x). Sensors belonging to the left half do the opposite (Figure 6.10. This mode affects mostly the local u coordinate.

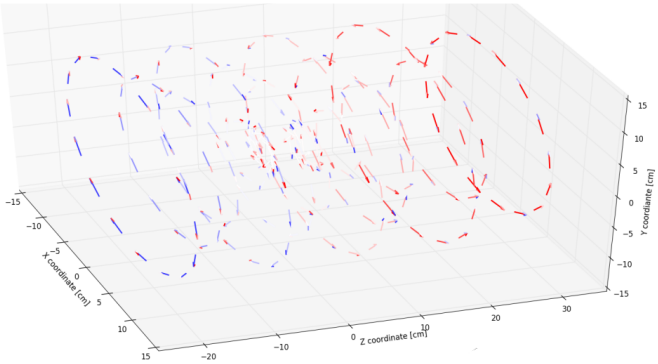

(a) Global coordinates.

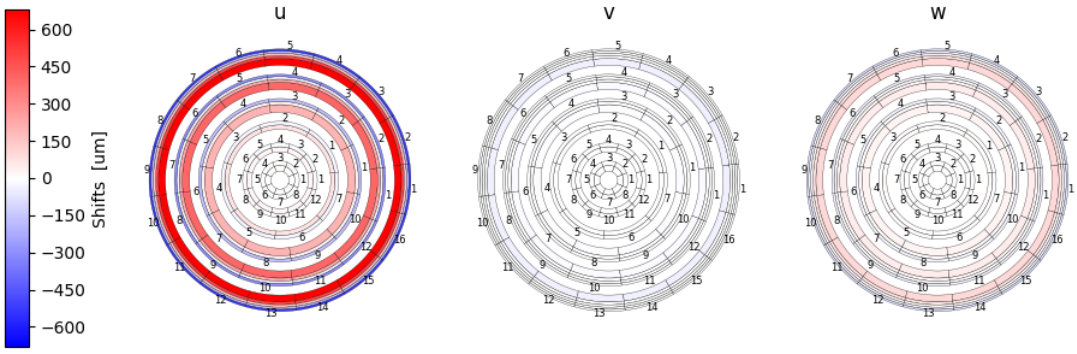

(b) Local coordinates.

Figure 6.10: Schematic description of the VXD twist misalignment in the global coordinates system (a) and in the local coordinates system (b). The magnitude of the misalignment in the color bar is used for the analysis.

- **Z-expansion (Figure 6.11):** $\Delta z = c_{scale} \cdot z$.

  Sensors on one axial half of the detector shift along the positive z-direction, while those on the other half along the negative z-direction. This mode affects mostly the local v coordinate.

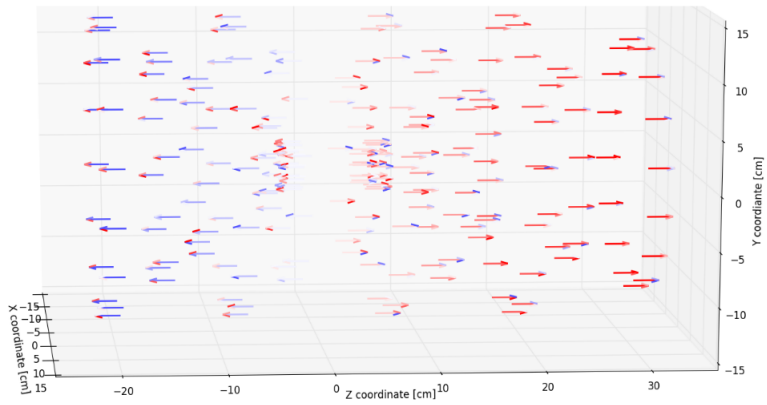

(a) Global coordinates.

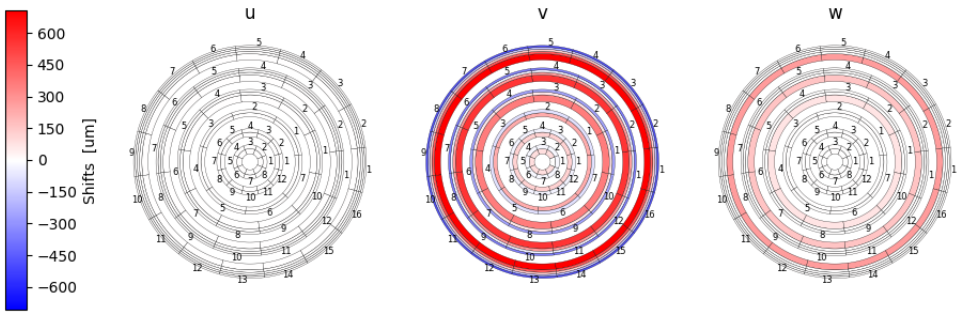

(b) Local coordinates.

Figure 6.11: Schematic description of the VXD z-expansion misalignment in the global coordinates system (a) and in the local coordinates system (b). The magnitude of the misalignment in the color bar is used for the analysis.

6.3 Weak mode detection

Figure 6.12 shows the distribution of the χ^2 probability for every fitted track in a sample of $e^+e^- \to \mu^+\mu^-$ events subject to all the possible weak modes individually. Here $\chi^2 = \chi^2(\vec{\tau}_j, \vec{a}) = \sum_i^{hits} z_{ij}^2(\vec{\tau}_j, \vec{a})$ and corresponds to the one provided by the reconstruction algorithm for a fitted j track.
I use log-scale on the y-axis because of the peak at probabilities close to zero associated to non-optimal fits, due to lack of additional constraints on the track model.
In the 0.0 to 0.2 probability range, distributions for the aligned configuration and for those resulting from z-expansion, curl and elliptical-expansion nearly overlap, showing little sensitivity of the standard procedure, as expected.
The tails of the χ^2 distributions show marginally higher probabilities for the aligned geometry, but still the observed small differences are likely to be diluted in the presence of background in realistic conditions. It seems challenging to distinguish between the various weak modes and then correct the sensors coordinates accordingly, using only Millepede II outputs.

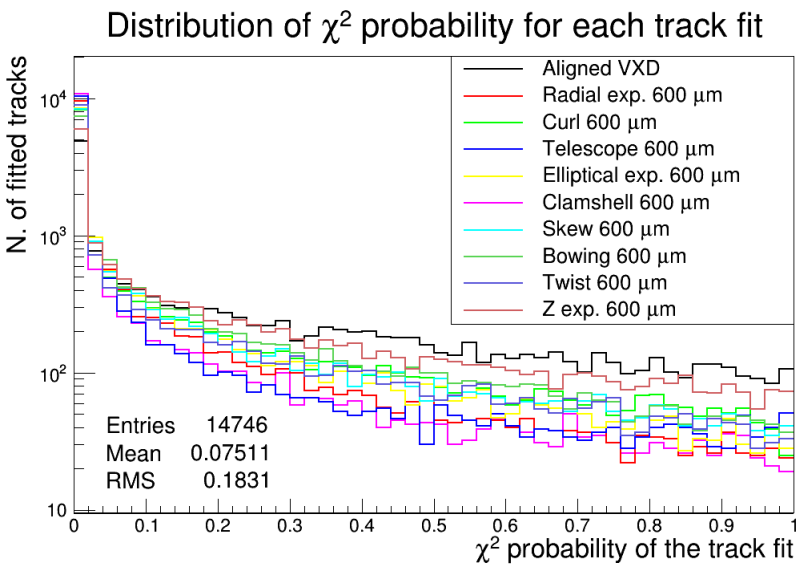

Figure 6.12: Distributions of the χ^2 probability for each fitted track in $e^+e^- \to \mu^+\mu^-$ events. Each color of the histograms corresponds to one of the weak modes listed in the legend.

To obviate to this limitation of the Millipede II approach, I search for distinctive patterns in the distributions of reconstructed track variables for each weak-mode configuration. The goal is to identify the presence of weak-mode misalignments and possibly to isolate a one-to-one correspondence between a specific misalignment mode of the vertex detector and a set of specific features observed in reconstructed quantities.

I use 5000 $e^+e^- \rightarrow \mu^+\mu^-$ signal-only events. Prior to reconstruction I produce a set of systematically misaligned configurations, based on a set of realistic input parameters for the deformations, using the code described in section 6.2.
After reconstruction, I select signal tracks according to the conditions described in section 5.3.
I test the effects of the VXD weak modes by looking at the normalized distributions of appropriately chosen tracking variables and comparing them with the distribution observed in the configuration of an aligned VXD. The variables I test are combinations of track parameters of the two muons and their values are those extrapolated from the track fit at the point of closest approach to the z-axis.
Finally, I study the robustness of my findings against the presence of backgrounds.

6.3.1 Signal-only data

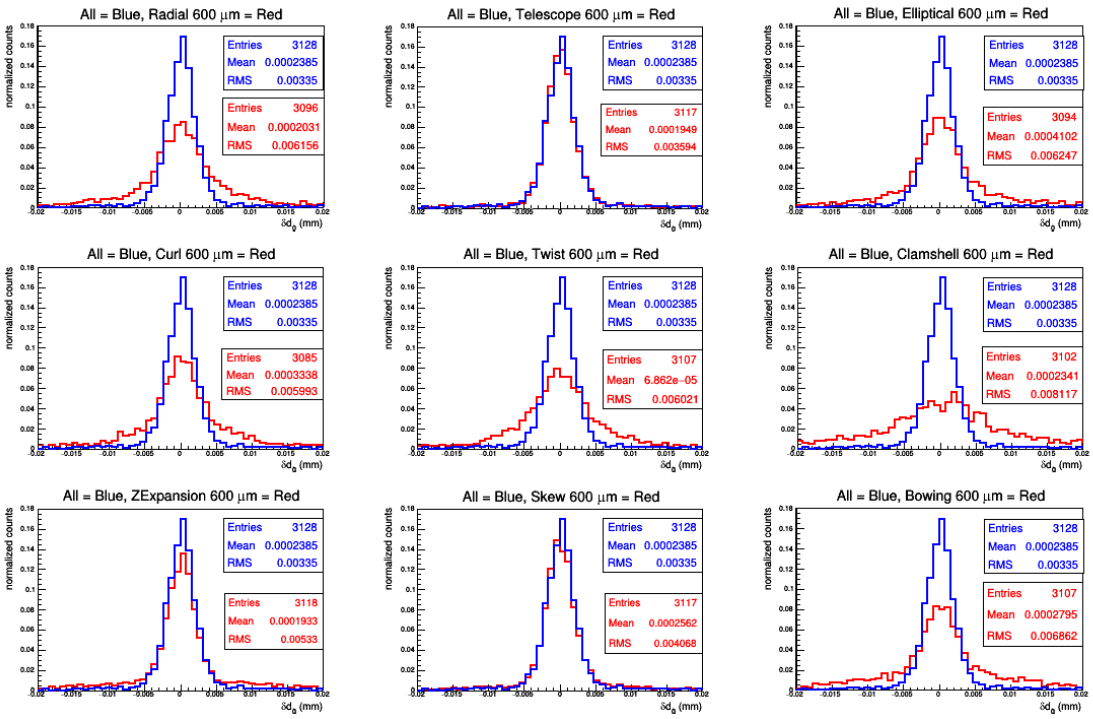

Figure 6.13: Distributions of δd_0 for VXD misaligned according to the main weak modes by an amount of maximum 600 μm. Every panel shows both the histogram corresponding to a configuration of alignment (blue) and the histogram originating from a weak mode (red). All the simulated weak modes produce shifts of the same magnitude (see plots).

I first test the effects of weak-mode misalignments of the vertex detector on recon-

structed $e^+e^- \to \mu^+\mu^-$ signal-only events. To search for misalignment patterns among the large number of possible combinations of track parameters, I first simulate large misalignments of up to 600 μm, which although possible, are quite unlikely. This stretched scenario aims at offering an immediate understanding of what variables are promising in providing distinctive signatures and what are insensitive. Once identified the subset of sensitive variables, I explore the effects of more realistically sized misalignments of 200 and 100 μm.

By examining the geometrical perturbations associated with each weak-mode I identified a restricted set of potentially useful variables that are combinations of reconstructed track parameters at POCA, and looked at their distributions. In particular, I compared the distribution originating from every weak mode with the one obtained for the aligned geometry.

The first tested variable is $\delta d_0 = d_0(\mu^+) - d_0(\mu^-)$, namely the difference of the reconstructed transverse impact parameters of the μ^+ and the μ^-. Figure 6.13 is referred to 600 μm misalignments and shows that modes producing a longitudinal deformation of the detector along the z-direction, like telescope, z-expansion and skew, leave the distribution of δd_0 unaffected. This is consistent with the fact that d_0 is a distance on the transverse xy plane. The main effect of the other modes is a widening of the distribution, that is strongest in the case of clamshell.

While I investigated systematically the effect of each weak mode on d_0 for more realistic misalignment sizes of 100 and 200 μm, as an example, I show in Figure 6.14 the effects of clamshell deformations only, since it is the mode that mostly affects d_0.

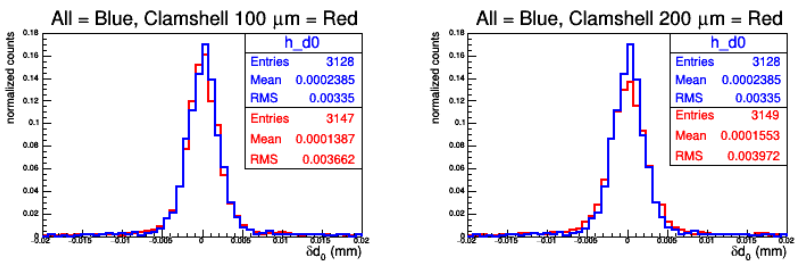

Figure 6.14: Distributions of δd_0 for aligned VXD (blue) and for a clamshell (red) of 100 μm (left panel) and 200 μm (right panel).

Figure 6.14 shows that δd_0 is nearly insensitive to a 100 μm clamshell and only poorly sensitive to a 200 μm clamshell. In both cases, we do not observe a significant widening of the δd_0 distribution.

A complementary variable that probes the longitudinal shifts on scalings is $\delta z_0 = z_0(\mu^+) - z_0(\mu^-)$, the difference between the reconstructed longitudinal impact parameters.

Figure 6.15 shows that the δz_0 distribution is invariant, with respect to the aligned ge-

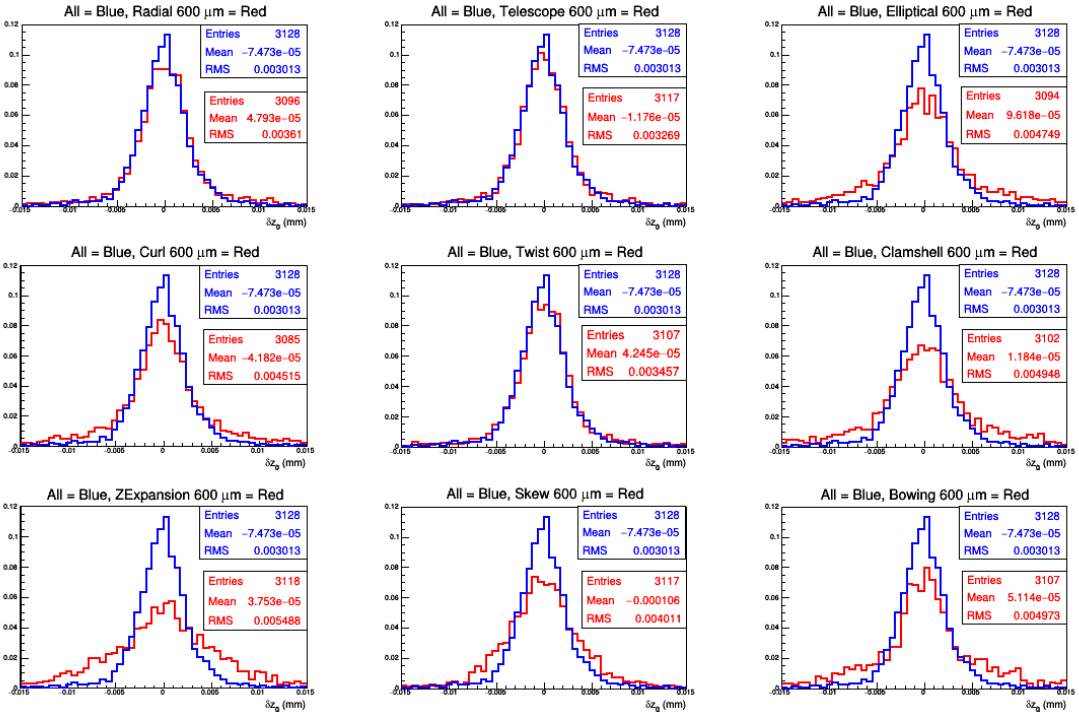

Figure 6.15: Distributions of δz_0 for VXD misaligned according to the main weak modes by an amount of maximum 600 μm. Every panel shows both the histogram corresponding to a configuration of alignment (blue) and the histogram originating from a weak mode (red). All the simulated weak modes produce shifts of the same magnitude (see plots).

ometry, for the radial-expansion, the telescope and the twist. The curl, that is a rotation of the sensors on the transverse plane, affects minimally the distribution. The remaining modes produce a more evident widening in the distribution of δz_0 and the most distinctive is the spread observed in the case of the z-expansion. This is expected, because we are producing a deformation along the direction where we measure the longitudinal impact parameter z_0.
While I investigated systematically the effect of each weak mode on δz_0 for more realistic misalignment sizes of 100 and 200 μm, as an example, I show in Figure 6.16 the effects of z-expansion only. For both deformations, the δz_0 distribution experiences a negligible widening and a small bias on its mean value.

Since the effects of the individual weak modes for realistically-sized misalignments are modest on the single tracking variables chosen so far, I test whether a better discrimination between aligned and misaligned detector setups can be obtained by studying the distance δ introduced in Chapter 5, which encapsulates coherently several small effects in a single variable.

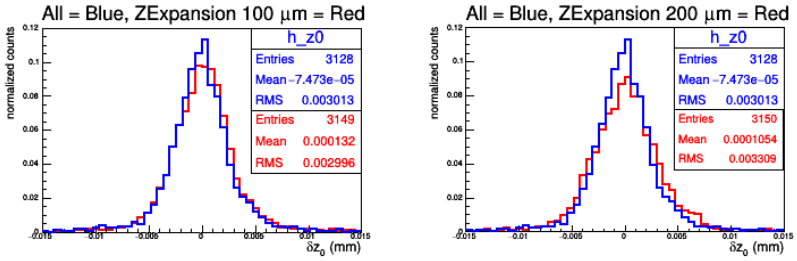

Figure 6.16: Distributions of δz_0 for aligned VXD (blue) and for a clamshell (red) of 100 μm (left panel) and 200 μm (right panel).

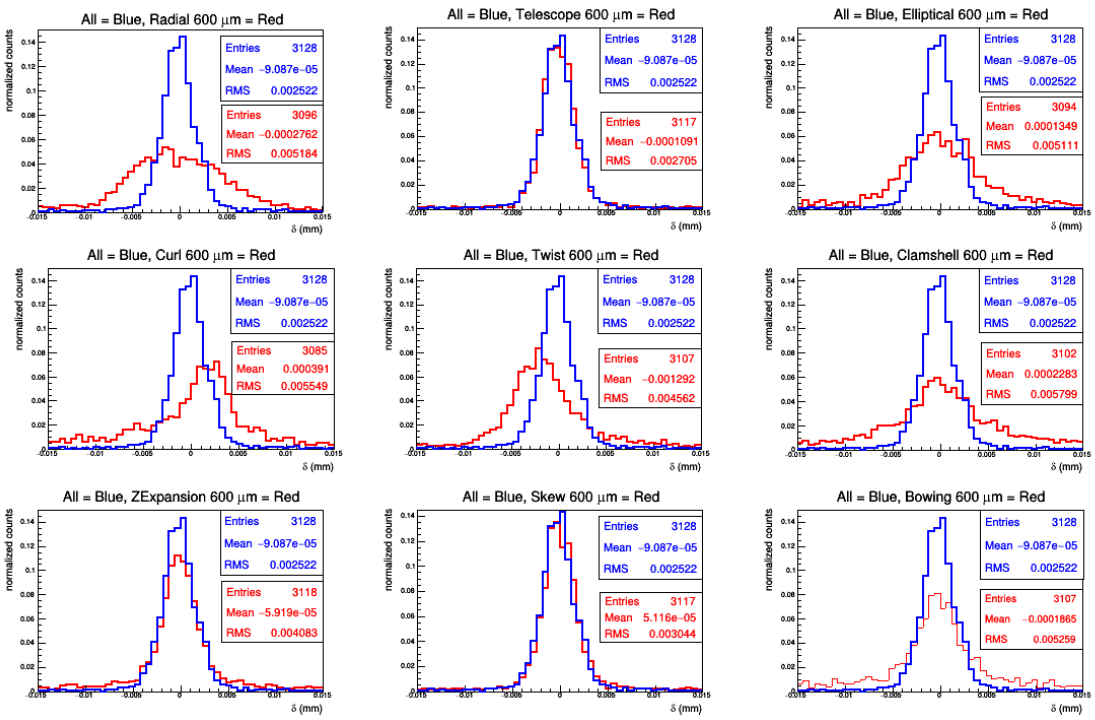

Figure 6.17: Distributions of δ for VXD misaligned according to the main weak modes by an amount of maximum 600 μm. Every panel shows both the histogram corresponding to a configuration of alignment (blue) and the histogram originating from a weak mode (red). All the simulated weak modes produce shifts of the same magnitude (see plots).

This variable is again quite informative as shown in Figure 6.17. The distribution of δ is invariant for the telescope and the skew and it highly sensitive to the radial-expansion and the clamshell. A striking effect on the distribution appears in the case of curl and twist, where the distributions shift, respectively, to the right and to the left of the one obtained in the case of an aligned vertex detector. These observed patterns seem promising toward

unambiguously identify the curl and the twist. All the remaining modes affect negligibly the distribution of the δ distance.
Similarly as in the previous cases, I investigated systematically the effect of each weak mode on δ for more realistic misalignment sizes of 100 and 200 μm, and, as an example, I show in Figure 6.18 the effects of clamshell deformation only.

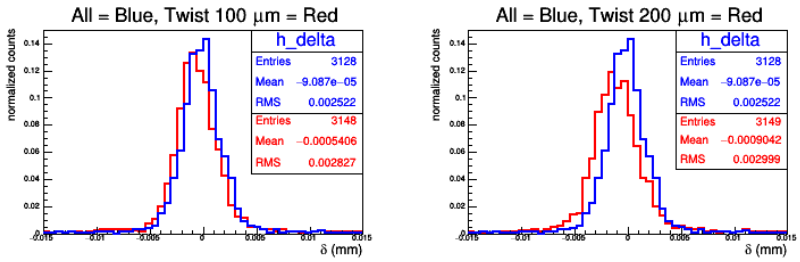

Figure 6.18: Distributions of δ for aligned VXD (blue) and for a clamshell (red) of 100 μm (left panel) and 200 μm (right panel).

Figure 6.18 shows that δ is only poorly shifted towards negative values for a 100 μm twist, while it experiences a more significant shift in the case of 200 μm twist. These results prove again the sensitivity of the δ distance, showing that it can be used to spot even some moderate misalignments.

Another variable sensitive to the weak modes is the distance between the POCAs of the two muons on the transverse plane

$$\Delta_{xy} = \sqrt{(x^{(+)}_{POCA} - x^{(-)}_{POCA})^2 + (y^{(+)}_{POCA} - y^{(-)}_{POCA})^2}. \tag{6.1}$$

Figure 6.19 shows the Δ_{xy} distributions obtained from the reconstructed coordinates, for every weak mode.

This variable is highly sensitive to the curl and the clamshell, both implying rotations of sensors on the transverse (xy) plane. Two modes, namely the telescope and the skew, leave the distribution invariant because they produce deformations on the z-axis. The variable Δ_{xy} is poorly sensitive to the remaining modes.
Given that curl is the mode that mostly changes the shape of the Δ_{xy} distribution, I look at the effects of 100 μm and 200 μm curl misalignments on Δ_{xy}.
Figure 6.20 shows that Δ_{xy} is not sensitive to smaller curl misalignments of 100 μm and 200 μm.

I tested many other variables and a summary of the results obtained for misalignments of 600 μm is listed in the table of Figure 6.21. Here, the elements of the first row are the weak modes and those of the first column the variables I tested. Green tick marks

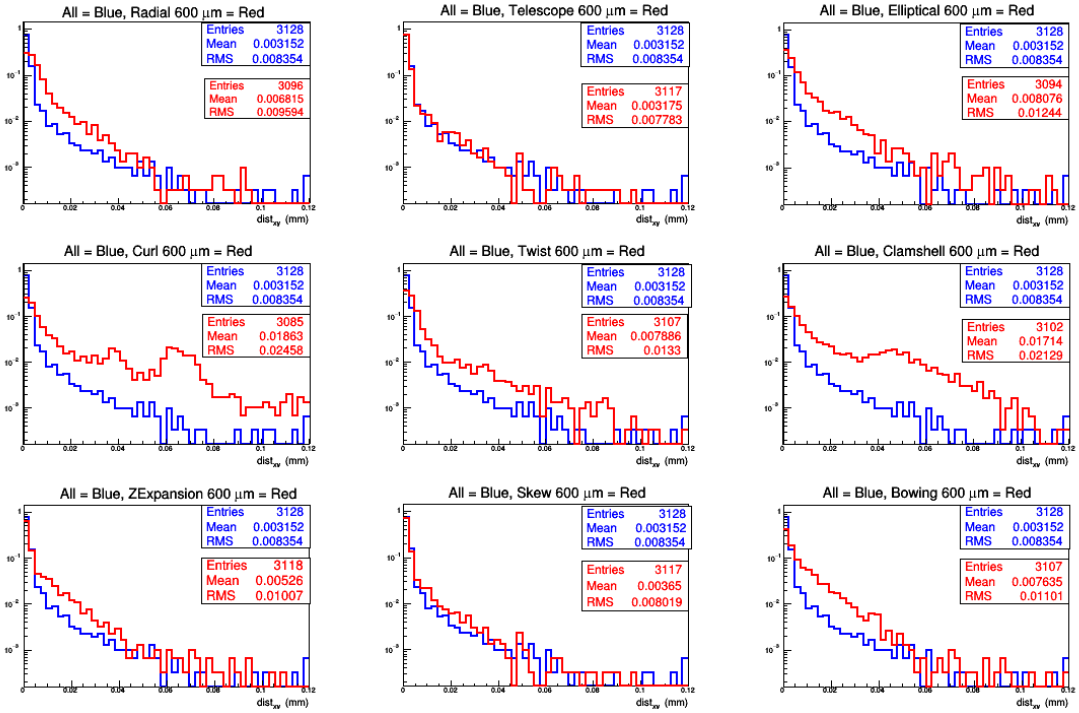

Figure 6.19: Distributions of Δ_{xy}. Every panel shows both the histogram corresponding to a configuration of alignment (blue) and the histogram originating from a weak mode (red). All the simulated weak modes produce shifts of the same magnitude.

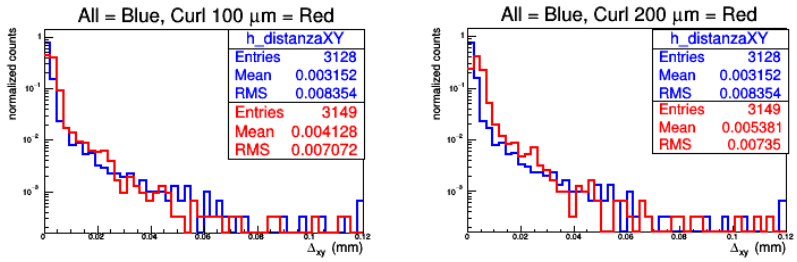

Figure 6.20: Distributions of Δ_{xy} for aligned VXD (blue) and for a clamshell (red) of 100 μm (left panel) and 200 μm (right panel).

indicate highly sensitive variables, yellow tick marks indicate poorly sensitive variables, and red cross marks indicate variables insensitive to the weak mode. Magenta circles are used for variables that seem promising to identify unambiguously a weak mode.
This table sums up the studies performed on the weak modes of the vertex detector and shows that the procedure I developed allows to identify rapidly and efficiently many weak modes, some of them even unambiguously, assuming that the size of the intervening ef-

fect is large. No powerful indicators of weak-mode misalignments of size inferior of 200 microns could be found.

Figure 6.21: Summary table of 600 μm weak modes tests. In the first row all the weak modes are listed and the first column shows all the tested variables.
Green tick marks are given to variables highly sensitive to the weak-mode, yellow tick marks to poorly sensitive variables and red crosses to variables which are invariant to the mode. Magenta circles are used when a variable allows to unambiguously identify a weak-mode.

6.3.2 Including background

Then I moved to study whether the previous findings remain valid in realistic conditions, i.e., when tracks reconstruction is performed on a sample including all the relevant processes occurring in a e^+e^- collision at the $\Upsilon(4S)$ center-of-mass energy.
The main processes resulting from an e^+e^- collision at the center-of-mass energy of $\sqrt{s} = 10.573$ GeV are those listed, together with their cross sections, in the Table 3.1. In particular, the cross section for the process $e^+e^- \to \mu^+\mu^-$ is 1.148 nb, corresponding approximately to the 0.6% of the total cross section.
Using the appropriate proportions between relative cross sections in the generators KKMC (for leptonic events), EvtGen (for hadronic events) and BabaYagaNLO (for Bhabha scatterings) I produced a generic sample of 5×10^4 events, with contributions from every process. Then I simulated the interactions of the generated particles with the Belle II detector in the Phase 3 geometry and eventually I performed track reconstruction for the whole sample.
Since I am interested in charged tracks coming from $e^+e^- \to \mu^+\mu^-$ events, I apply the requirements described in section 5.3 on the generic sample and restrict to only these events.
Inspection of the azimuthal differences and correlations for muon candidates (Figure 6.22), defined as opposite-sign high-momentum tracks with matching KLM hits shows results similar to those obtained in the signal-only sample, showing that our simple selection is sufficient to isolate a pure sample of opposite-charge muon pairs.

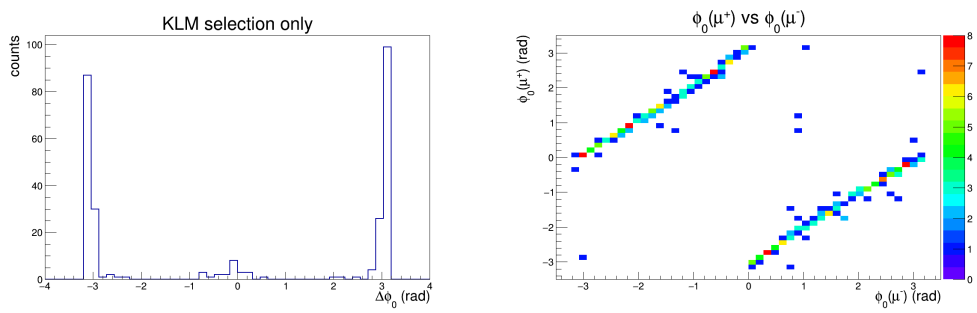

(a) $\Delta\phi_0$ distribution (b) $\phi_0(\mu^+)$ vs $\phi_0(\mu^-)$ scatter plot.

Figure 6.22: $\Delta\phi_0$ distribution (a) and scatter plot of the azimuthal angles at POCA (b) for two reconstructed tracks having opposite charge and hits in the KLM.

Given the complexity of the simulation procedure, the resulting samples contain a smaller number of signal events than those studied previously, but these are already sufficient to check our findings in realistic conditions.

While to investigate if patterns observed for a signal-only sample are still present in

realistic conditions I systematically studied all distributions, for the sake of illustration I report here only those more apt to illustrate the most striking effects, that is the distributions of δd_0, δz_0, δ, and Δ_{xy}.

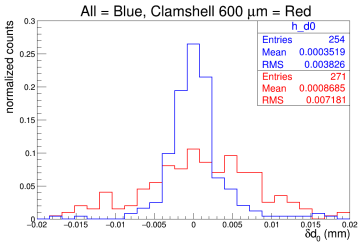

(a) δd_0 distributions: aligned VXD (blue) and 600 μm clamshell (red).

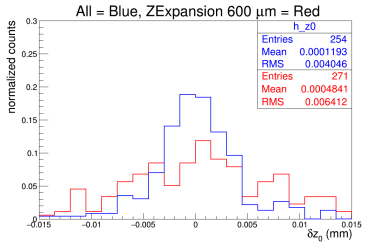

(b) δz_0 distributions: aligned VXD (blue) and 600 μm z-expansion (red).

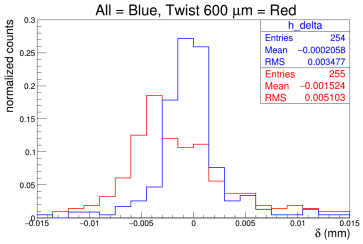

(c) δ distributions: aligned VXD (blue) and 600 μm twist (red).

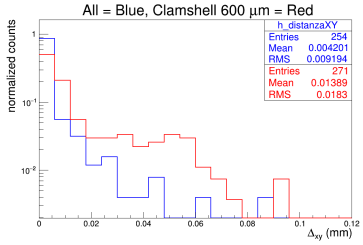

(d) Δ_{xy} distributions: aligned VXD (blue) and 600 μm clamshell (red).

Figure 6.23: Distributions of highly sensitive variables δd_0 (a), δz_0 (b), δ (c), Δ_{xy} (d) for an aligned configuration (blue) and a weak-mode misalignment (red).

These examples (see Figure 6.23), and the full set of plots not illustrated here, show that the main features associated with weak-modes misalignments remain visible and detectable in the realistic Belle II Phase 3 conditions.

Chapter 7

Detecting misalignments through overlapping sensors

This chapter discusses a novel, complementary approach I introduced in Belle II to study vertex-detector misalignments using hits in azimuthally overlapping sensors at same radii. This approach renders the misalignment search nearly independent of multiple scattering effects and probes powerful to supplement standard procedures.

7.1 Coordinate-residual differences

A further original method I developed to monitor and validate the effects of a VXD weak-mode on reconstruction, is to use the hits from tracks passing through regions where azimuthally adjacent modules overlap within a radial layer of the tracker. This method requires larger amounts of data, since only a small subset of tracks traverses VXD regions with overlapping layers, but offers a unique advantage since deviations for two consecutive hits produced by multiple scattering are small, given the little radial distance between overlapping sensors.
I select overlapping-region hits from 10^4 simulated $e^+e^- \to \mu^+\mu^-$ signal-only events. As a sensitive estimator of misalignment I define a difference of coordinate residuals for pairs of hits located in azimuthally overlapping, radially consecutive sensors (see Figure 7.1):

$$res = \Delta u_{\text{ext.}} - \Delta u_{\text{int.}}, \tag{7.1}$$

where

$$\Delta u = u^{\text{meas.}} - u^{\text{pred.}} \tag{7.2}$$

and u is the hit coordinate parallel to the short side of the sensor. The same variable can

be defined also for the local v coordinate that is the one parallel to the long side of the sensor.

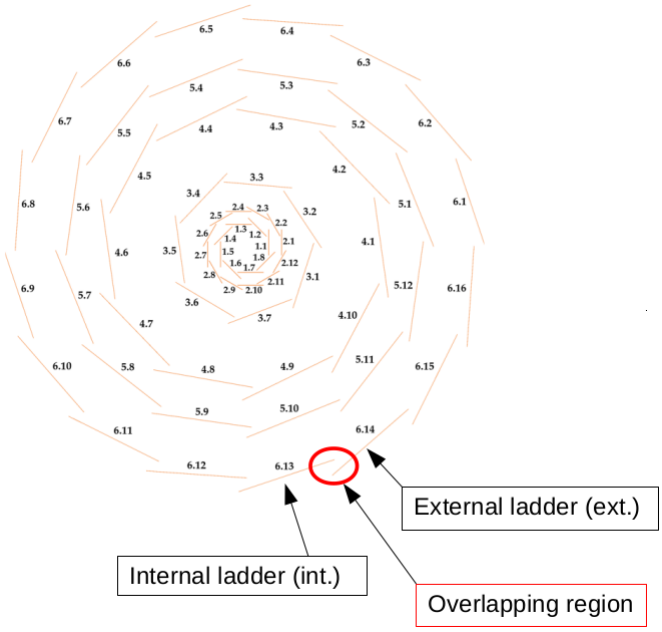

Figure 7.1: Schematic view on the transverse plane of the VXD. The red circle surrounds a region where two sensors of a same layer overlap.

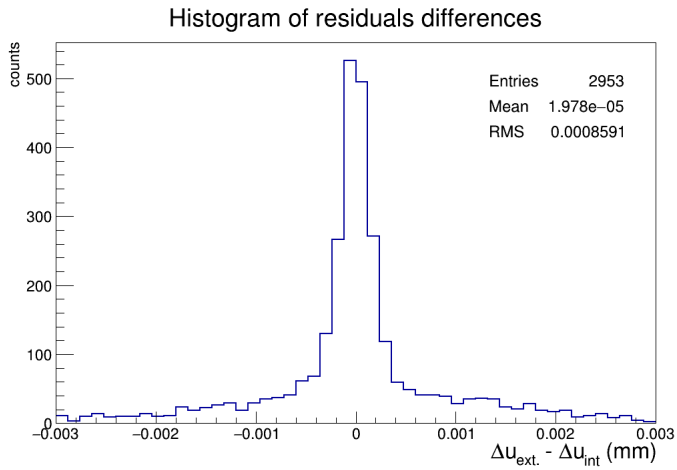

Figure 7.2: Distribution of $res = \Delta u_{ext.} - \Delta u_{int.}$ for aligned VXD.

When the VXD is aligned we observe the distribution in Figure 7.2 that is symmetric, unimodal, and mean-valued at zero.

The strategy is based again on comparing the distribution for the ideal alignment with those observed when I simulate a misalignment.

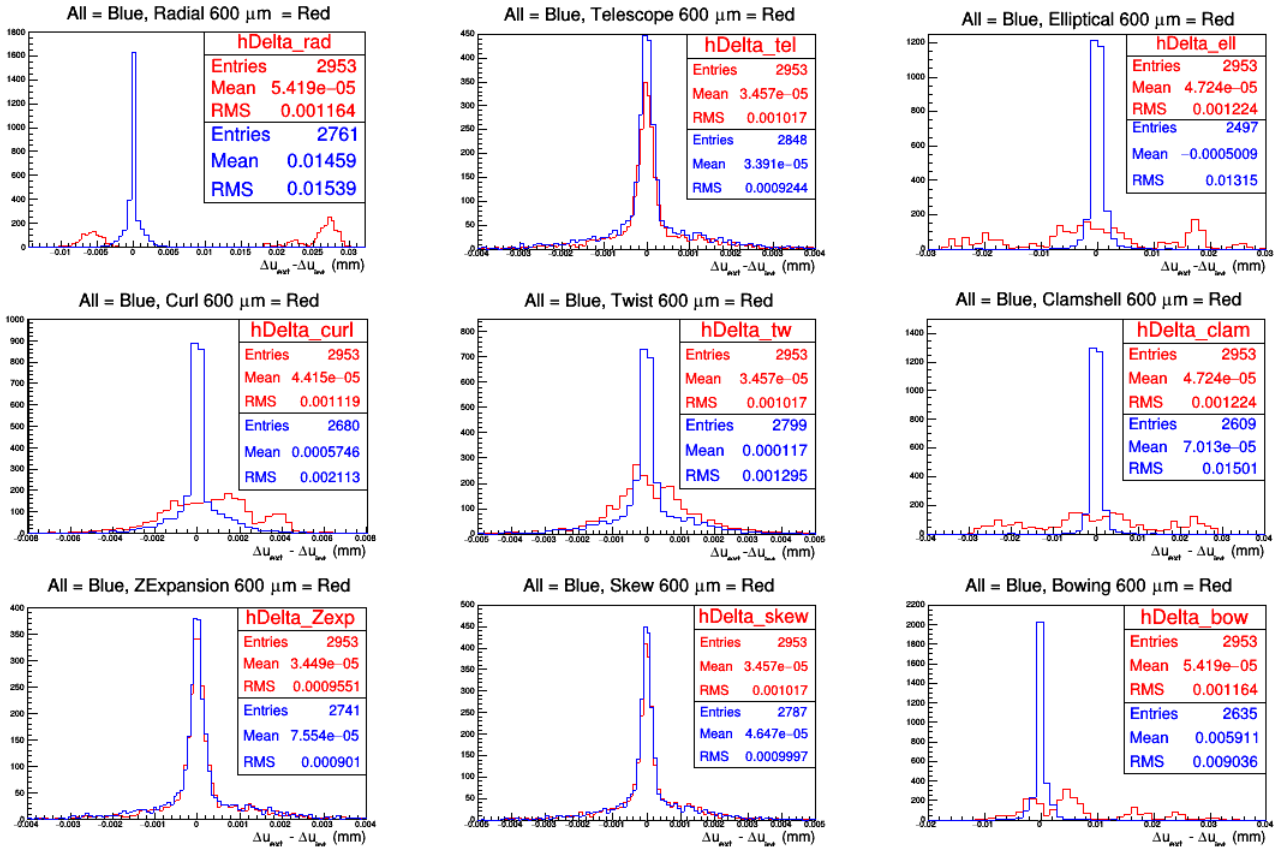

Figure 7.3: Distributions of $res = \Delta u_{ext.} - \Delta u_{int.}$ for VXD misaligned according to the main weak modes by an amount of 600 μm. Every panel shows both the histogram corresponding to a configuration of alignment (blue) and the histogram originating from a weak mode (red). All the simulated weak modes produce shifts of the same magnitude, as can be seen in the titles above the plots.

7.2 Results

In each panel of Figure 7.3 we compare the distribution of $\Delta u_{ext.} - \Delta u_{int.}$ obtained from an aligned VXD (blue) to that resulting from one of various misalignments (red) of 600 μm maximum.

It is reassuring to observe that the telescope, the z-expansion and the skew configurations leave the distribution of this variable invariant. This is expected, because those three

modes produce deformations along the z-direction, while u is a local coordinate defined on the transverse plane.
The most distinctive features of the residual differences are observed in the case of the radial-expansion, the elliptical-expansion, the clamshell and the bowing that lead to asymmetric and/or multi-modal distributions.

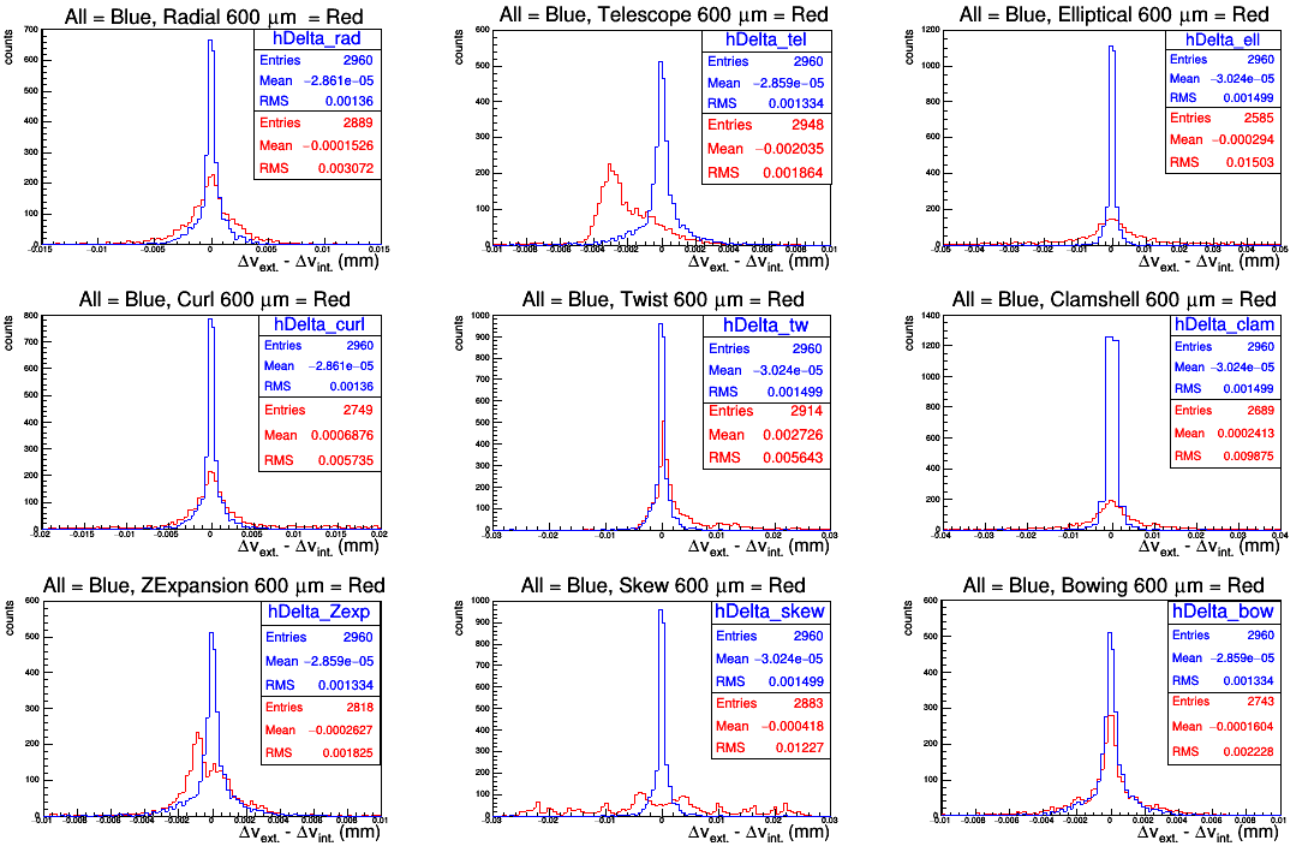

Figure 7.4: Distributions of $res = \Delta v_{ext.} - \Delta v_{int.}$ for VXD misaligned according to the main weak modes by an amount of 600 μm. Every panel shows both the histogram corresponding to a configuration of alignment (blue) and the histogram originating from a weak mode (red). All the simulated weak modes produce shifts of the same magnitude, as can be seen in the titles above the plots.

Results for v residuals are shown in Figure 7.4. In this case, $res = \Delta v_{ext.} - \Delta v_{int.}$ is sensitive to all the weak modes. Some of them broaden the distribution with respect to the configuration of alignment. This effect is more relevant in case of elliptical-expansion, radial-expansion and clamshell, while it is smaller for a bowing or a curl. The weak modes producing the most striking deviations, from the distribution obtained for an aligned VXD, are those that cause longitudinal displacements of the VXD sensors, thus affecting

mostly the local v coordinate of their positions. Figure 7.4 shows that telescope and z-expansion are responsible for a shift of the *res* distribution towards negative values; skew results in a large multi-modal distribution; twist creates a long tail over positive values. Then I performed the same studies in case of weak mode misalignments of 200 μm, which represents a more realistic magnitude. All the weak modes have been tested, but here in Figure 7.5 I show only those producing the most striking effects.

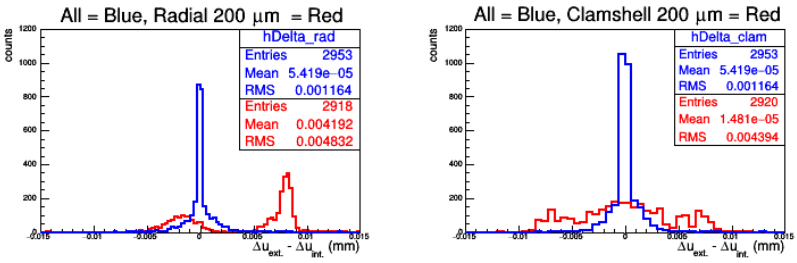

(a) $\Delta u_{ext.} - \Delta u_{int.}$ distributions: aligned VXD (blue), 200 μm radial-expansion (red, left panel) and clamshell (red, right panel).

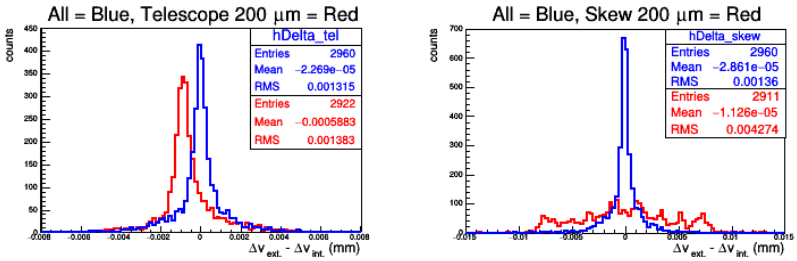

(b) $\Delta v_{ext.} - \Delta v_{int.}$ distributions: aligned VXD (blue), 200 μm telescope (red, left panel) and skew (red, right panel).

Figure 7.5: Distributions of $\Delta u_{ext.} - \Delta u_{int.}$ (upper panels) and $\Delta v_{ext.} - \Delta v_{int.}$ (lower panels) for aligned VXD (blue) and weak modes of 200 μm (red).

Figure 7.5 shows that $\Delta u_{ext.} - \Delta u_{int.}$ and $\Delta v_{ext.} - \Delta v_{int.}$ residuals for azimuthally overlapping sensors at adjacent radii allow for detecting weak-mode deformations of even modest entity, that would remain otherwise invisible to all track-based indicators. This is a remarkable result brought to Belle II by my innovative approach to the monitoring of VXD misalignments.

Given the relevance of these results for weak-mode detection, I proceeded to test the sensitivity of the overlapping-sensor approach by extending it to random misalignments of modest (50 μm) to large (200 μm) entity. Figure 7.6 shows the effects of these two random misalignments on u and v residual differences. The distributions corresponding to randomly misaligned cases show a 10× (50 μm) to 30× (200 μm) increase in width, offering a striking and powerful discriminator against the aligned cases even for small to

moderate misalignments as those expected in realistic condition.

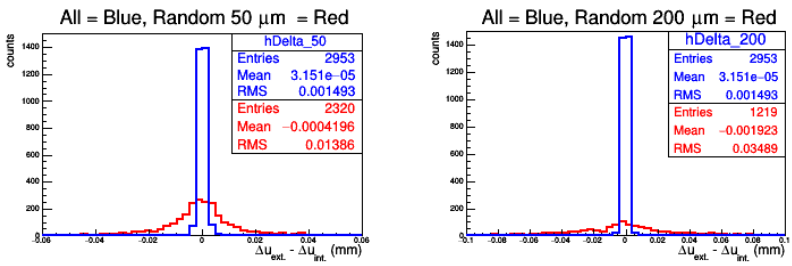

(a) $\Delta u_{ext.} - \Delta u_{int.}$ distributions: aligned VXD (blue), 50 μm random misalignment (red, left panel), 200 μm random misalignment (red, right panel).

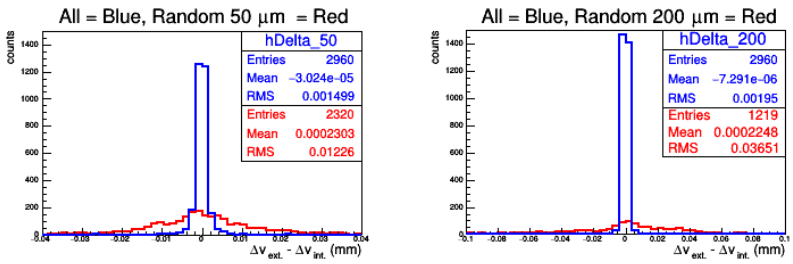

(b) $\Delta v_{ext.} - \Delta v_{int.}$ distributions: aligned VXD (blue), 50 μm random misalignment (red, left panel), 200 μm random misalignment (red, right panel).

Figure 7.6: Distributions of $\Delta u_{ext.} - \Delta u_{int.}$ (upper panels) and $\Delta v_{ext.} - \Delta v_{int.}$ (lower panels) for aligned VXD (blue) and random misalignments of 50 μm and 600 μm (red).

The table in Figure 7.7 gives an overview on the sensitivity of u and v residual differences to VXD misalignments.

Results of this section prove the major impact of looking at hits in azimuthally overlapping sensors at same radii. This method was not previously used by the Belle II tracking and alignment group and it has been applied for the first time in this thesis work. At the moment, given the results of other alignment studies performed at Belle II, this approach seems the most powerful and sensitive to identify moderate random and systematic misalignments of the vertex detector, and it may be considered a third key result of this work.

$res_{(u)} = \Delta u_{ext.} - \Delta u_{int.}$

$res_{(v)} = \Delta v_{ext.} - \Delta v_{int.}$

✓ : highly sensitive to the weak-mode.

✓ : poorly sensitive to the weak-mode.

✗ : invariant to the weak-mode.

	Random $50\mu m$	**Random** $200\mu m$	**Radial** $600\mu m$	**Curl** $600\mu m$	**Tel.** $600\mu m$	**Elliptical** $600\mu m$	**Clam.** $600\mu m$	**Skew** $600\mu m$	**Bow.** $600\mu m$	**Twist** $600\mu m$	**Z-exp.** $600\mu m$
$res_{(u)}$	✓	✓	✓	✓	✗	✓	✓	✗	✓	✓	✗
$res_{(v)}$	✓	✓	✓	✓	✓	✓	✓	✓	✓	✓	✓

Figure 7.7: Summary table for u, v residual differences. In the first row all the tested misalignments are listed and the first column shows the residual differences $res_{(u)}$ and $res_{(v)}$. Green tick marks are given to variables highly sensitive to the misalignment, yellow tick marks to poorly sensitive variables and red crosses to variables which are invariant to the misalignment.

Chapter 8

First look at data and summary

Since May 2018, the first samples of e^+e^- SuperKEKB collision data are available. As of today (July 10, 2018), more than 250 pb^{-1} of data have been collected. While the initial SuperKEKB and Belle II operating conditions have been too rapidly changing and uncertain to guarantee a quality of the data sufficient to pursue my studies effectively, I think it is still scientifically interesting to report here the first basic distributions of the quantities associated with my studies.

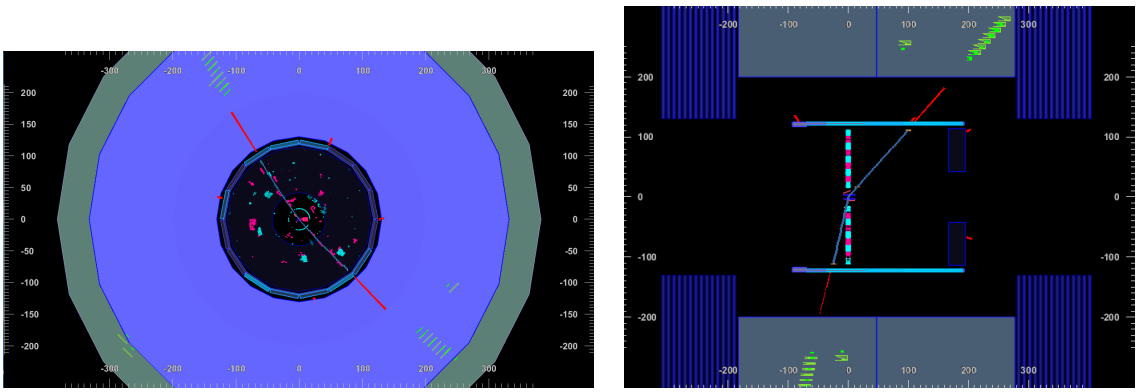

(a) Event display in the xy-plane. (b) Event display in the z-plane .

Figure 8.1: Dimuon event display in the xy-plane of the detector (a) and in the z-plane (b), recorded during a commissioning run in May 2018.

Figure 8.1 shows a dimuon event display recorded during one of the initial runs. Figure 8.2 shows distributions of reconstructed track parameters using raw data (blue) and after applying a preliminary set of selection requirements, cuts (red), recommended by the tracking and muon detector experts, which include fiducial requirements on impact parameters acceptance, track multiplicity, momenta, opening angle, and associated energy deposits in the calorimeter. Because only a narrow azimuthal sector of the vertex

detector was installed when these data were collected, it is unrealistic to use them just yet for precision studies as those discussed in this thesis. However, the availability of a first and growing sample of dimuons opens promising perspectives for extending our studies in data in early 2019, when the full vertex detector will be installed.

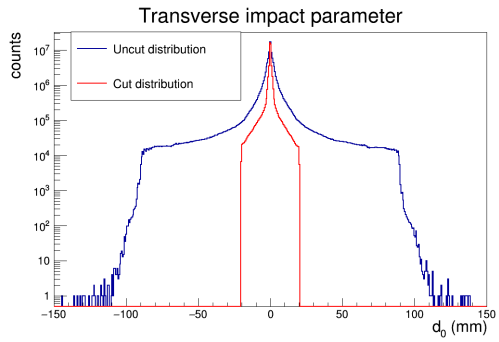

(a) Reconstructed transverse impact parameter.

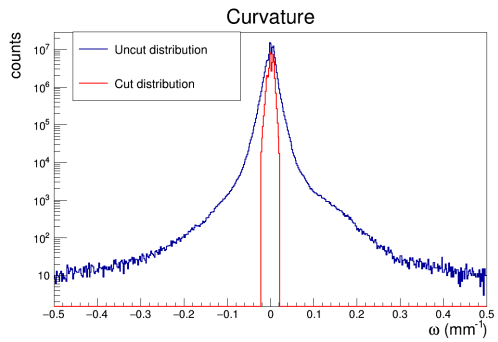

(b) Reconstructed curvature.

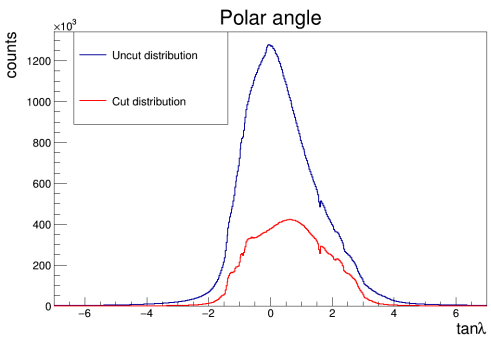

(c) Reconstructed tanλ.

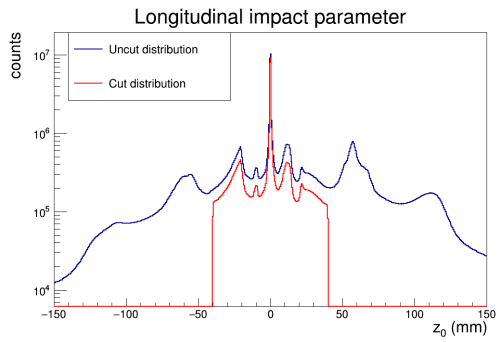

(d) Reconstructed longitudinal impact parameter.

Figure 8.2: Distributions of reconstructed track parameters from μ^+ and μ^- tracks from raw data (blue) and applying preliminary cuts (red).

Belle II is going to be at the forefront of indirect searches of non-SM physics at the intensity frontier. It will seek signatures of new dynamics by comparing precise measurements and SM predictions in processes sensitive to the contributions from virtual non-SM particles, by using billions of B, D and τ lepton decays. Precise charged-particle tracking with accurate momentum and impact parameter determination is essential for the Belle II success.

In this thesis I developed studies to monitor the performances of the inner Belle II tracker, focusing on the effects of possible misalignments of the vertex detector on the reconstructed quantities.
I used simulated $e^+e^- \to \mu^+\mu^-$ samples to develop fast and efficient procedures to identify misalignments in real time, thus supplementing the standard off-line alignment algorithm of Belle II.
The chief results of my work are the following:

- I invented a new variable, the distance between linearized tracks, which is able to consistently and coherently sum the informations from each track parameter in a simple higher-level scalar quantity that proves to be very sensitive and of immediate availability with few data;
- I identified a small set of variables that allow for a fast identification of a specific misalignment and may be unambiguously connected to certain weak modes;
- I introduced, first in Belle II, studies based on track hits in overlapping sensors that are extremely sensitive to a broad class of random and weak alignment configurations of even minor entity.

An internal note of my work is in progress and is currently reviewed by the Belle II tracking group which aims at integrating my findings in the standard procedure for track-quality monitoring.

Acknowledgements

Let me conclude by thanking my supervisor Diego Tonelli for his constant support and advice, Eugenio Paoloni and Giulia Casarosa from the University of Pisa for their invaluable help with technical matters, alongside with Jakub Kandra [52] and Tadeas Bilka [53], from the Belle II group at Charles University in Prague, who gave me the basics for alignment studies.

Bibliography

[1] Z. Dolezal, S. Uno et al. Belle II Technical Design Report. *KEK Report 2010-1, arXiv:1011.0352.*

[2] Ohnishi, Yukiyoshi. SuperKEKB collider. Recent progress. *Kasokuki; ISSN 1349-3833*, 2015.

[3] S. Weinberg. A Model of Leptons. *Physical Review Letters, vol. 19, Issue 21, pp. 1264-1266*, 1967.

[4] S. Glashow. The renormalizability of vector meson interactions. *Nucl. Phys. 10, 107*, 1959.

[5] A. Salam, J.C. Ward. Weak and electromagnetic interactions. *Il Nuovo Cimento, vol. 11, issue 4, pp. 568-577*, 1959.

[6] K. Abe, et. al, The Belle Collaboration. Observation of Large CP Violation in the Neutral B Meson System. *Phys.Rev.Lett.87:091802,2001.*

[7] B. Aubert, et. al, BABAR Collaboration. Observation of CP violation in the B^0 meson system. *Phys.Rev.Lett.87:091801,2001.*

[8] Nicola Cabibbo. Unitary Symmetry and Leptonic Decays. *Phys. Rev. Lett. 10, 531*, 1963.

[9] S. L. Glashow, J. Iliopoulos and L. Maiani. Weak Interactions with Lepton-Hadron Symmetry. *Phys. Rev. D 2, 1285.*

[10] S. L. Glashow, B.J.Bjorken. Elementary particles and SU(4). *Physics Letters*, 11, 1964.

[11] J. J. Aubert, U. Becker, P. J. Biggs, J. Burger, M. Chen, G. Everhart, P. Goldhagen, J. Leong, T. McCorriston, T. G. Rhoades, M. Rohde, Samuel C. C. Ting, Sau Lan Wu, and Y. Y. Lee. Experimental Observation of a Heavy Particle J. *Phys. Rev. Lett. 33, 1404*, 1974.

[12] J. E. Augustin et al. Discovery of a Narrow Resonance in e+e- Annihilation. *Phys. Rev. Lett. 33, 1406*, 1974.

[13] J. H. Christenson, J. W. Cronin, V. L. Fitch, and R. Turlay. Evidence for the 2π Decay of the K_2^0 Meson. *Rev. Lett. 13, 138*, 1964.

[14] Makoto Kobayashi, Toshihide Maskawa. CP-Violation in the Renormalizable Theory of Weak Interaction. *Progress of Theoretical Physics*, 49, 1973.

[15] CLEO Collaboration (M.S. Alam et al.). First measurement of the rate for the inclusive radiative penguin decay $b \to s\gamma$. *Phys.Rev.Lett. 74 (1995) 2885-2889.*

[16] ARGUS Collaboration (H. Albrecht et al. *Observation of B0-anti-B0 Mixing.*

[17] David P. Coupal. Review of Results from the Mark II Experiment at SLC. *SLAC-PUB-5240*, 1990.

[18] A. J. Bevan et al. The Physics of the B Factories. *Eur. Phys. J. C74 (2014) 3026.*

[19] Jonathan Lewis (Fermilab), Rick van Kooten (Indiana U.). Review of Physics Results from the Tevatron: Heavy Flavor Physics. *Int.J.Mod.Phys. A30 (2015) no.06, 1541003.*

[20] CMS Collaboration (S. Chatrchyan et al.). The CMS Experiment at the CERN LHC. *JINST 3 (2008) S08004.*

[21] ATLAS Collaboration (G. Aad et al.). The ATLAS Experiment at the CERN Large Hadron Collider. *JINST 3 (2008) S08003.*

[22] LHCb Collaboration (A.Augusto Alves, Jr. et al.). The LHCb Detector at the LHC . *JINST 3 (2008) S08005.*

[23] Peter W. Higgs. Broken Symmetries and the Masses of Gauge Bosons. *Phys. Rev. Lett. 13, 508*, 1964.

[24] F. Englert, R. Brout. Broken Symmetry and the Mass of Gauge Vector Mesons. *Phys. Rev. Lett. 13, 321*, 1964.

[25] Lincoln Wolfenstein. Parametrization of the Kobayashi-Maskawa Matrix. *Phys. Rev. Lett. 51, 1945*, 1983.

[26] The NA48 Collaboration: V. Fanti, et al. A new measurement of direct CP violation in two pion decays of the neutral kaon. *Phys.Lett.B465:335-348,1999.*

[27] A. Alavi-Harati et al. (KTeV Collaboration). Observation of Direct CP Violation in $K_{S,L} \to \pi\pi$ Decays. *Phys. Rev. Lett. 83, 22*, 1999.

[28] CKMfitter group (J. Charles et al.). Current status of the Standard Model CKM fit and constraints on $\Delta F = 2$ New Physics. *Phys. Rev. D 91, 073007 (2015).*

[29] The Belle II collaboration and B2TiP theory community. The Physics Prospects for Belle II. *BELLE2-REPORT (2016).*

[30] P. Raimondi. Status on SuperB Effort. *http://www.lnf.infn.it/conference/superb06/talks/raimondi1* 2006.

[31] C. Marinas. The Belle II pixel detector: High precision with low material. *Nuclear Instruments and Methods in Physics Research*, 731, 2013.

[32] J. Kemmer and G. Lutz. *Nucl. Instrum. Meth. Phys.Res. A 253, 356 (1987).*

[33] K. Adamczyk et al. Belle II silicon vertex detector. *Nuclear Instruments and Methods in Physics Research*, 831, 2016.

[34] Taniguchi, N. Central Drift Chamber for Belle-II. *Journal of Instrumentation, Volume 12, Issue 06, pp. C06014 (2017).*

[35] S. Iwata et al. Particle identification performance of the prototype Aerogel RICH counter for the Belle II experiment. *Prog. Theor. Exp. Phys. (2016) 033H01.*

[36] V. Aulchenko et al. Electromagnetic calorimeter for Belle II. *Journal of Physics: Conference Series*, 587.

[37] L. Piilonen et al. The upgraded KLM detector at Belle II. *APS April Meeting 2016, abstract id. R17.007.*

[38] Andreas Moll. The software framework of the Belle II experiment. *J.Phys.Conf.Ser. 331 (2011) 032024.*

[39] R. Brun et al. ROOT: An object oriented data analysis framework. *Nucl.Instrum.Meth. A389 (1997) 81-86.*

[40] GEANT4 Collaboration (S. Agostinelli et al.). GEANT4: A Simulation toolkit. *Nucl.Instrum.Meth. A506 (2003) 250-303.*

[41] Volker Blobel, Claus Kleinwort, Frank Meier. Fast alignment of a complex tracking detector using advanced track models. *arXiv:1103.3909.*

[42] Anders Ryd et al. EvtGen: A Monte Carlo Generator for B-Physics. *EVTGEN-V00-11-07.*

[43] Torbjorn Sjostrand et al. An Introduction to PYTHIA 8.2. *arXiv:1410.3012.*

[44] TS. Jadach, B. Ward, and Z. Was. The Precision Monte Carlo event generator KK for two fermion final states in e+e- collisions. *Comput.Phys.Commun. 130 (2000) 260–325, arXiv:hep-ph/9912214.*

[45] C. M. Carloni Calame, G. Montagna, O. Nicrosini, and F. Piccinini. The BABAYAGA event generator. *Nucl. Phys. Proc. Suppl. 131 (2004) 48–55, arXiv:hep-ph/0312014.*

[46] C. M. Carloni Calame, G. Montagna, O. Nicrosini, and F. Piccinini. Matching perturbative and parton shower corrections to Bhabha process at flavour factories. *Nucl.Phys. B758 (2006) 227–253, arXiv:hep-ph/0607181.*

[47] Guido Altarelli, G. Parisi. Asymptotic Freedom in Parton Language. *Nucl.Phys. B126 (1977) 298-318 (1977).*

[48] Johannes Rauch, Tobias Schlüter. GENFIT - a Generic Track-Fitting Toolkit. *Journal of Physics: Conference Series 608 (2015) 012042.*

[49] Kalman, Rudolph Emil. A New Approach to Linear Filtering and Prediction Problems. *Transactions of the ASME–Journal of Basic Engineering*, 82(Series D):35–45, 1960.

[50] R. Fruhwirth and A. Strandlie. Track Fitting with Ambiguities and Noise: A Study of Elastic Tracking and Nonlinear Filters. *Computer Physics Communications, 120(2-3):197–214, 1999.*

[51] C. Kleinwort. General Broken Lines as advanced track fitting method. *Nucl. Instrum. Meth. A673 (2012) 107–110.*

[52] J. Kandra. Simulation of Belle II physics events and performance tests of reconstruction software. *Charles University in Prague, 2016.*

[53] T. Bilka. Simulation and analysis of tests of Belle II vertex detector sensors. *Charles University in Prague, 2014.*